2011

Surface profile measurement techniques for large aperture optical thin film membrane structures

Kevin D. Spradley

SURFACE PROFILE MEASUREMENT TECHNIQUES FOR LARGE APERTURE OPTICAL THIN FILM MEMBRANE STRUCTURES

by

KEVIN D. SPRADLEY

A THESIS

Submitted in partial fulfillment of the requirements
for the degree of Master of Science
in
The Department of Physics
to
The School of Graduate Studies
of
The University of Alabama in Huntsville

HUNTSVILLE, ALABAMA
2011

In presenting this thesis in partial fulfillment of the requirements for a master's degree from The University of Alabama in Huntsville, I agree that the Library of this University shall make it freely available for inspection. I further agree that permission for extensive copying for scholarly purposes may be granted by my advisor or, in his/her absence, by the Chair of the Department or the Dean of the School of Graduate Studies. It is also understood that due recognition shall be given to me and to The University of Alabama in Huntsville in any scholarly use which may be made of any material in this thesis.

Kevin T. Moralley 10-11-11

(student signature) (date)

THESIS APPROVAL FORM

Submitted by Kevin D. Spradley in partial fulfillment of the requirements for the degree of Master of Science in Physics and accepted on behalf of the Faculty of the School of Graduate Studies by the thesis committee.

We, the undersigned members of the Graduate Faculty of The University of Alabama in Huntsville, certify that we have advised and/or supervised the candidate on the work described in this thesis. We further certify that we have reviewed the thesis manuscript and approve it in partial fulfillment of the requirements for the degree of Master of Science in Physics.

Don A Gregory 10/14/11 Committee Chair
Dr. Don Gregory (Date)

A M. Dem 10/14/2011
Dr. Abdalla Elsamadicy

Joseph Geary 10/14/11
Dr. Joseph Geary

G. P. Zank Department Chair
Dr. Gary Zank

10/17/11 College Dean
Dr. John Fix

Rhonda Kay Gaede 11/29/11 Graduate Dean
Dr. Rhonda Gaede

ABSTRACT

The School of Graduate Studies
The University of Alabama in Huntsville

Degree Master of Science College/Dept. Science/Physics

Name of Candidate Kevin D. Spradley

Title Surface Profile Measurement Techniques for Large Aperture Optical Thin Film Membrane Structures

Large aperture thin film optics typically have substantial shape errors which are difficult to quantify with conventional measurement methods, such as interferometry. The interferograms are normally too complex and contain too much information to discern relevant shape information pertinent to (for example) solar energy collection. This led to the development of an application oriented, less expensive and less complex measurement procedure based on well-defined geometric relationships. Classical aberration coefficients are derived from this information and, using commercially available optical modeling software, a recognized method for analyzing the performance of the optic can be employed.

Abstract Approval:

Committee Chair — Dr. Don Gregory

Department Chair — Dr. Gary Zank

Graduate Dean — Dr. Rhonda Gaede

ACKNOWLEDGMENTS

I would like to extend my sincerest thanks and gratitude to the members of my committee who provided extremely helpful advice and guidance. This would not have been possible without the aid and watchful eye of my advisor, Prof. Don Gregory. My other committee members, Dr. Abdalla Elsamadicy and Dr. Joe Geary, provided valuable insight into the experimentation and testing areas of this thesis research. These three advisors were also integral to this research by providing me with the steps and teaching I needed to improve the overall quality of the research.

Another very important person who deserves a big thank you is Dr. John Outerbridge who provided experimental assistance during this research. I would also like to thank United Applied Technologies for supplying the test articles. Without their optics, this research would not have been possible.

Last, but certainly not least, I need to express how much my family supported and urged me to continue. My parents, Harold and Joan Spradley, have played such a large role in this research over the years that it cannot be captured on paper. So to them, I can only say thank you for everything from the bottom of my heart and I love you. Without question, my wife Dreama Spradley, was the rock during this process and provided the encouragement to finish. I am at a loss for words how to express what she has meant to this thesis, so again I can only say, I love you. Finally, to my son Russell who gave me the drive to finish, I love you more than life itself and hope one day you read this as you are preparing your thesis or dissertation.

TABLE OF CONTENTS

LIST OF FIGURES

LIST OF TABLES

CHAPTER 1

INTRODUCTION TO THIN FILM SOLAR COLLECTORS

This thesis will present a new method for quantifying the shape of large diameter thin-membrane optical elements which typically have substantial shape error making them difficult to test using conventional techniques such as interferometry. This new method is less expensive and less complex than traditional methods and makes use of geometric relationships that are easy to quantify. The experimental technique evolved as data was gathered for several large thin membrane mirrors, and the latest version of the technique, presented here, has proven to be very useful in the laboratory.

1.1 Thin Film Membrane Applications

Thin film membranes are perfect for large area space-based optical applications due to their ability to be stored in a small volume and then expanded once in orbit. The major materials being used for large area thin films are polyimide polymers and mylar. Future spacecraft missions will be heavily aided by the use of large area, ultra-lightweight systems. These thin film membranes can be used in many different ways; such as energy concentrators, solar baffles, and solar sails.[i] One of the more common material classes in use today is polyimide polymer, specifically Kapton manufactured by Dupont and some polyimide films made by manufacturers such as Nexolve and K-Tech. The uses of Kapton include solar collectors, wire insulation, aircraft insulation, and flexible circuits. [ii]

Other formulations of polyimides can be used similarly as solar shields, sails, collectors, insulation, and circuit boards. Mylar based applications typically include inflatable installations, such as membrane mirrors and solar sails, just like the polyimides. Thin film membrane optics used as reflectors are not limited to the usual light spectrum; flexible radar antennas incorporate polyimide films as well.

1.2 Solar Collection

Solar collectors, or concentrators, are and will continue to be instrumental in harvesting the natural energy of the sun for two main categories of use, heat generation and energy generation. Typically heat generating systems are non-concentrating collectors and energy generators are concentrating collectors. The non-concentrating type of system consists of flat plate and evacuated tube collectors for such application as space heating and heating water. The flat plate collectors are just large area dark absorbers which then transfer the heat through some fluid to an absorber for later use. The evacuated system uses individual glass tubes which absorb the light and transfer the heat into a fluid contained within each tube. This is then moved to the absorber for later use.[iii] For energy generation, concentrating collectors are used and the shape of the concentrator is critical to providing the amount of energy needed to produce a useful output.

Since ancient China, concentrating solar power has been used in accomplishing a variety of everyday tasks. One "example" of an early use of concentrated solar energy comes by the way of Archimedes where he used solar power as a defense system. The

legend dictates that he concentrated solar power to focus the light on the invading Roman ships causing to them to ignite.[iv]

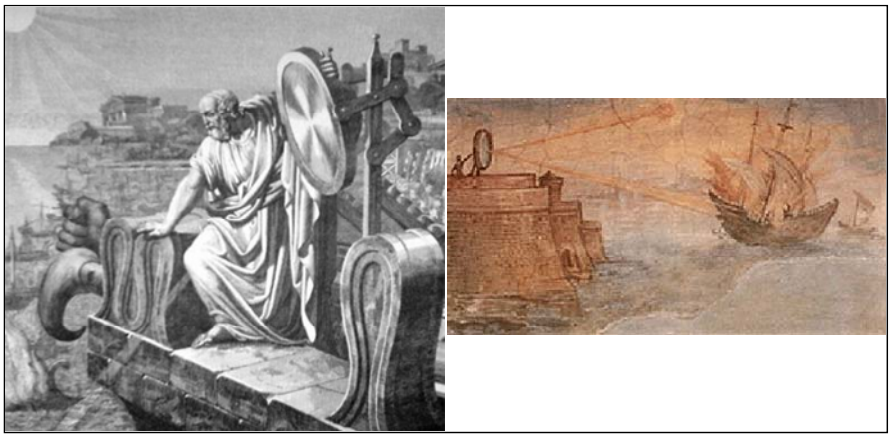

Figure 1.1 Archimedes and the "death ray" burning mirror used in 212 BC against the Romans.[v]

A Greek scientist in the 1970s attempted to recreate the Archimedes "burning glass" idea. He used a plywood cutout to simulate a Roman ship and an array of people holding mirrors and after a few minutes, the ship ignited.[vi] There are no reports of him running down the streets naked screaming "eureka, eureka," as Archimedes was said to have done after discovering the principle of buoyancy.

The energy generating systems typically use a parabolic shaped collector, either a dish or trough depending on the system. The trough approach generates a line focus which is incident on a heat pipe to absorb the energy. The dish approach is fairly self-explanatory; all the energy is focused onto a single point with some finite size. This is highly useful in solar thermal propulsion, solar pumped lasers, and solar collection heliostat fields used to drive a power generating station as seen in Figure 1.2.[vi]

Figure 1.2 Aerial and side view PS10 parabolic heliostat field located near Seville, Spain focusing the energy onto a power tower.[vii]

The first molten salt power generator station, named Archimede, integrated with a combined-cycle power plant has opened this year in Italy by the energy company Enel. While there are other molten salt stations around the world, this is the first that can still provide electricity at night or in overcast conditions.[viii]

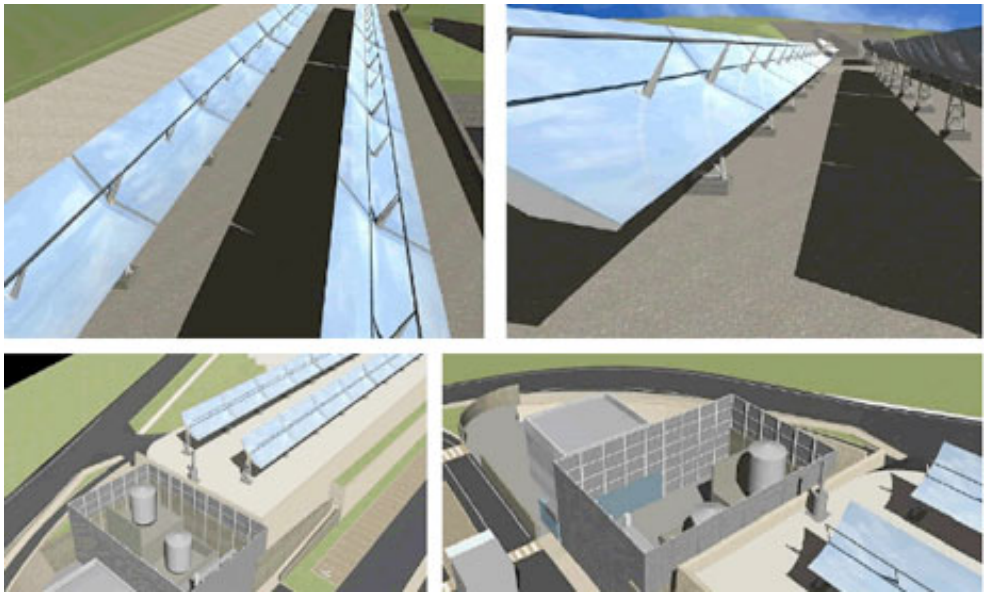

Figure 1.3 Computer generated rendering of Archimede integrated molten salt/combined cycle energy plant in Italy. Opening announced in July 2010.[ix]

1.3 Solar Radiometry

How much power can a solar collector collect if a solar collector could collect power? A fairly straightforward radiometric analysis of the sun and the collection optics used for this thesis is detailed below. The diagram below in Figure 1.4 illustrates the radiometry and defines the relevant terms. The following calculations are based on average solar numbers accepted by the solar radiation community. The irradiance of the sun at the edge of the atmosphere has been measured to be $E_{Sun} = 1366 \frac{W}{m^2}$ at the edge of the atmosphere, and contains all wavelengths not just the visible spectrum.[x,xi] This value can calculated for the wavelength range of interest by using spectral solar irradiance tables like the ASTM G173-03 Reference Spectra.[xii]

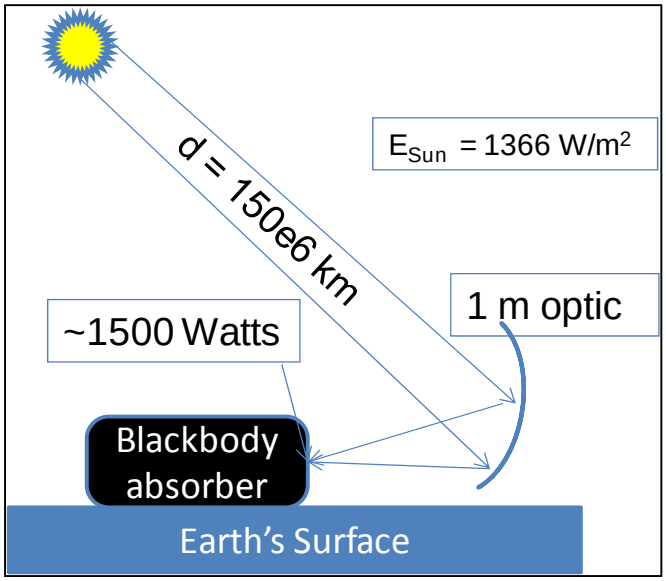

Figure 1.4 Simple radiometry setup for solar collection calculations for the optics tested.

This value reduces to $E_{Surface} \cong 1000 \frac{W}{m^2}$ at the Earth's surface on a plane normal to the Sun on a clear day. The actual value of the solar irradiance is affected by a variety of factors and should be calculated for the particular location of the collector. The altitude, latitude, longitude, time of day, cloud cover, and time of year are some factors used in determining exact solar irradiance.[x] How much solar radiation can a 1.0 m diameter collector collect? The equation for power through an aperture is

$$\boldsymbol{P = r * E_{Surface} * A_{Collector} = r * E_{Surface} * \pi * \left(\frac{D_{Collector}}{2}\right)^2}, \qquad \textbf{(1.1)}$$

where P is the power collected, r is the reflectivity of the collector, $A_{Collector}$ is the area of the collector, and $D_{Collector}$ is the diameter of the collector. Assuming a reflectivity of 1 and using a 1 m diameter optic, the total power collected is

$$\boldsymbol{P = 1 * 1000 \frac{W}{m^2} * \left(\frac{1m}{2}\right)^2 \cong 1500\, W.} \qquad \textbf{(1.2)}$$

The 0.5 m optic will capture 375 W of power since the area is reduced by a factor of 4 and therefore the power is also reduced by a factor of 4. Knowing the amount of power collected, the irradiance of the focus spot can be calculated to determine if the requirements dictated by the absorber material and application are met. There are two terms typically used for describing the effectiveness of a solar collector, the collection efficiency and the concentration ratio. The collection efficiency, CE, is the diameter of the collection optic divided by the diameter of the focused spot and the concentration ratio, CR, is the diameter of the optic divided by the diffraction limited spot size. Their respective expressions are shown below:

$$\boldsymbol{CE = \frac{D_{Collector}}{d_{spot}}} \quad \textbf{(1.3)}$$

$$\boldsymbol{CR = \frac{D_{Collector}}{d_{Airy}}}, \quad \textbf{(1.4)}$$

where $d_{Airy} = 2.44 * \lambda * \frac{f}{D_{Collector}}$ and λ is the wavelength of interest, f is the focal length of the optic, and $D_{Collector}$ is the diameter of the collecting optic.

1.4 Solar Thermal Propulsion

Solar thermal propulsion (STP) as an alternative to conventional propulsion methods can provide transportation for orbital and interplanetary missions. Since the 1970's, solar thermal propulsion has been considered an efficient means of orbital transfer from low Earth orbit (LEO) to geostationary Earth orbit (GEO).[xiii] Solar thermal propulsion generates higher specific impulse (800 to 1150 seconds) compared to chemical propulsion which is promising for performing orbital transfers starting from low earth orbit (LEO).[xiv] Solar thermal propulsion is an excellent choice because it requires only one propellant gas and combines moderate thrust with moderate propellant efficiency. For more distant travel such as interplanetary missions, a solar thermal engine using this propulsion would act like a simple, efficient tugboat in space.[xv]

In STP, the sun's energy is focused onto an absorber, which then radiates the energy into a cryogenic propellant during a thrust phase. The sun's energy could be transferred directly to the propellant for use during interplanetary missions needing continuous thrust, a difficult and arduous task. The underlying principle of solar thermal

propulsion is fairly straightforward: focus the sun's energy in order to heat a propellant and then force the hot expanded gas through a rocket nozzle to provide the thrust. An illustrative example of a solar thermal propulsion system is shown below in Figure 1.5.[xiv]

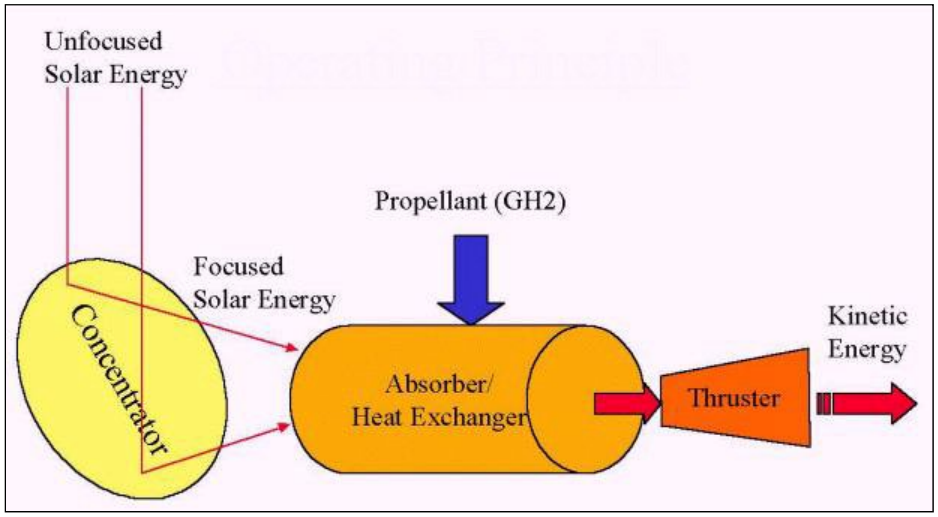

Figure 1.5 Illustrative example of a solar thermal propulsion system.[xiv]

In general, most solar collectors are parabolic in nature, allowing for a more concentrated spot compared to a spherical reflector, thus concentrating the same amount of energy into a smaller volume. The energy is directed into a black-body cavity which radiates the high temperature to the propellant flowing around the cavity where it is then expanded and forced through the nozzle.[xiv] For practical use in space, these parabolic mirrors need to be large-scale, lightweight inflatable optics in order to focus the proper amount of energy onto the absorber. The design configuration shown below in Figure 1.6 is from a 1979 Air Force sponsored program where the concentrator/thruster, located at focus were optically coupled to the concentrator. The concentrator in this particular design is an off-axis inflated parabolic reflector.[xiii]

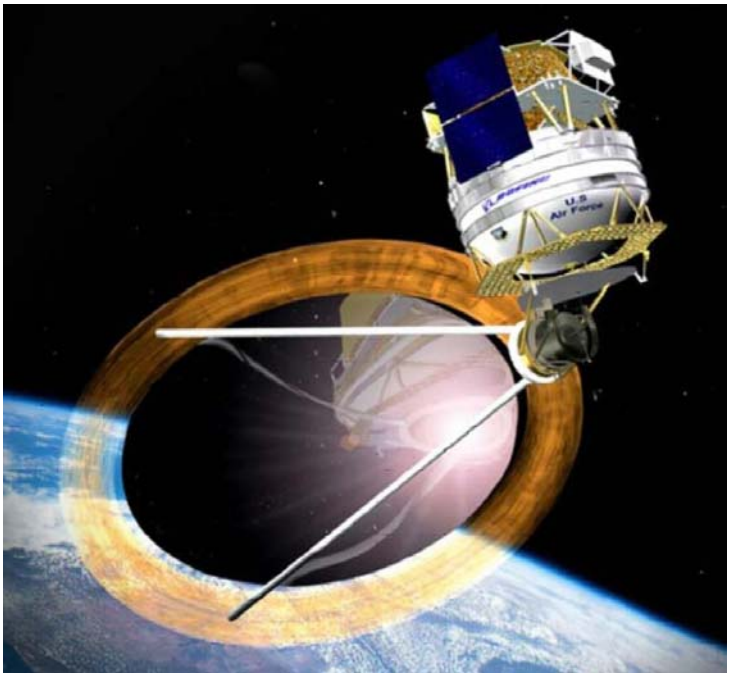

Figure 1.6 Rendering of inflatable off-axis parabolic concentrator coupled with the absorber/thruster located at the focus of the concentrator.[xiii]

The optically coupled absorber/thruster is sensitive to structural deformations in the concentrator due to the large scale and the non-rigid support structure. This can create misalignment and defocus at the absorber. An alternative method is to decouple the absorber/thruster from the concentrator and place at a location that will maximize thrust efficiency, and transmit the high energy solar power through flexible optical waveguides to the location of the absorber/thruster.[xiii] The system shown below in Figure 1.7 is a system designed and proposed in 2005 by Physical Sciences Inc (PSI), Rocketdyne, and Boeing in which the absorber/thruster are optimally located away from the focus of the concentrators. Using low-loss optical fibers as the waveguides, the high energy solar power is propagated to the absorber/thruster.

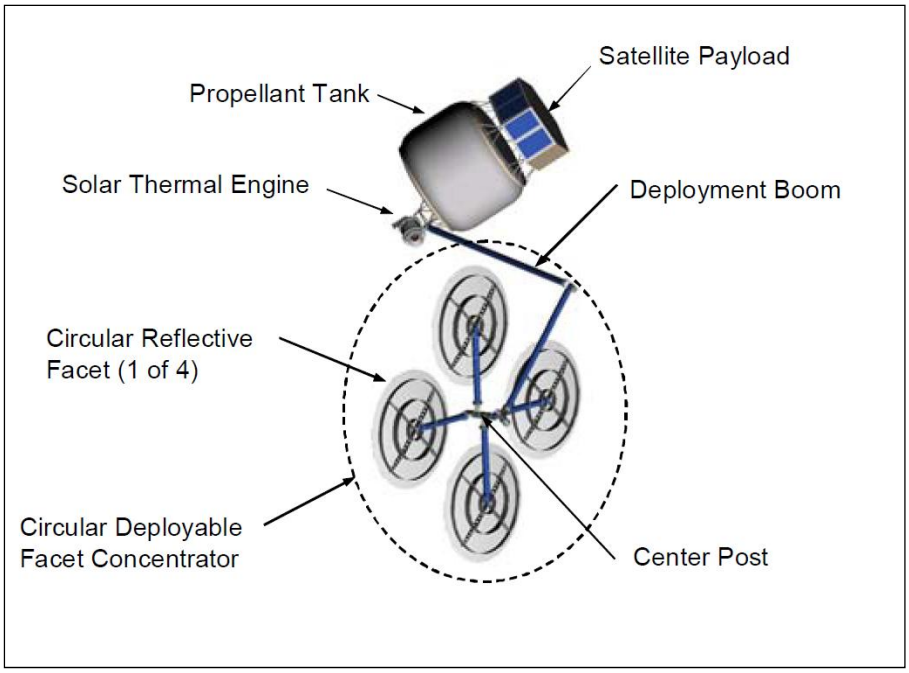

Figure 1.7 Deployed configuration of proposed system by PSI, Rocketdyne, and Boeing. Notice the location of the solar thermal engine (absorber/thruster) being located away from the focus of the concentrators.[xiii]

NASA and others believe that STP is an effective way of boosting payloads from LEO to GEO. It is feasible to consider trip times of 30 days for LEO-GEO transfer using this technology.[xiv,xv] Test units built at the Marshall Space Flight Center (MSFC) were to use hydrogen as the propellant and produce 2.5 N of thrust. The ground test absorber temperature within the cavity reaches 2450° C, with hydrogen being the working fluid which can reach an internal gas pressure of 170 kPa. The Solar Thermal Facility (STF) at the MSFC has built a solar thermal propulsion test system including a 20 ft x 24 ft heliostat mirror to follow the sun and direct the energy onto the 18 ft concentrator.[xv]

One of the key components of these solar thermal propulsion systems is the parabolic concentrator, and one of the key questions is how to launch a large mirror into space. Current and previous designs have used inflatable optics to create these parabolic

concentrators after the spacecraft is in orbit, but this type of optic is fairly susceptible to space debris and gas leaks, which would require a more sustainable gas supply, thus increasing payload mass. A different approach is to use a semi-rigid aluminized polymer, such as a common polyimide like Kapton, and heat form the material to the desired nominal shape through the use of material stress relaxation. The photo shown below in Figure 1.8 shows an aluminized concentrator that was built by Hironori Sahara and others as part of an end-of-lifetime de-orbit system.[xvi]

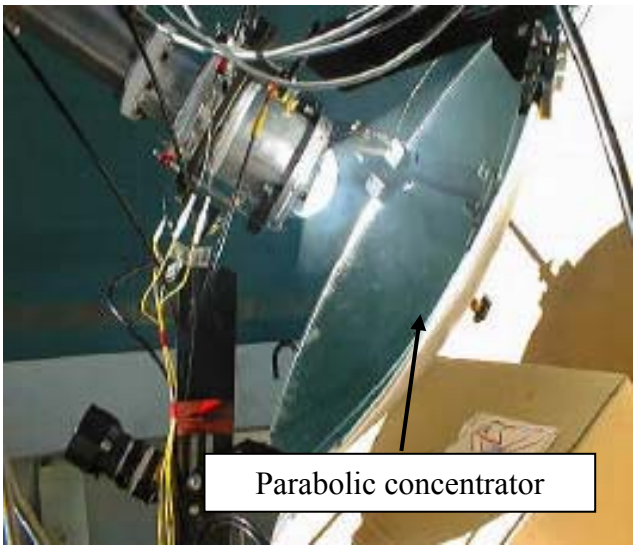

Figure 1.8 Test chamber and 640 mm parabolic solar concentrator built by Sahara for Japanese 50 kg Micro-Lab-Sat end-of-life de-orbit system.[xvi]

The parabolic shape accuracy is critical to focusing enough of the solar energy into a small enough spot to meet the collection efficiency requirements regardless of the deployment mechanism. The ideal solar image diameter is about 2.5 mm and a solar concentration ratio of 5000 will be needed to produce system with enough impulse to achieve the desired missions of orbital transfer, de-orbit end of life maneuvers, and

interplanetary travel.[xvi] The Japanese micro-sat system with a 640 mm diameter collector and spot diameters of 5 and 11 mm for two of their different mirrors, the efficiencies are 128 and 58 respectively. The mirror that produces the 11 mm spot has a solar concentration ratio of 3000, substantially below the 5000 needed.

1.5 Solar Pumped Lasers

As the name implies, solar pumped lasers operate like conventional lasers by emitting coherent radiation, but the difference lies in the fact that the lasing medium is not pumped by an artificial energy source; rather it is indeed pumped by solar radiation. Typically, solar pumped lasers are not used in regions where the cost of electricity is low enough to allow for more efficient electrically powered lasers.[xvii] Solar pumped lasers would be useful in areas without sufficient electrical supply, especially in space where inefficient solar panels cannot produce enough power to drive other more conventional lasers. A couple of space applications for solar powered lasers include beam-powered propulsion, space based solar power, and as a ballistic missile defense tool. Currently, the largest solar pumped laser is housed in the mountains outside of Tashkent, Uzbekistan. The 1 megawatt NdYag laser is being pumped by solar energy collected by a 40 m collector, shown in Figure 1.9 consisting of 62 individual mirrors which follow the sun's path.[xviii,xix]

Figure 1.9 Solar concentrator located in Uzbekistan. 40 m tall concentrator pumping a NdYag laser producing 1 MW of power.[xviii]

Another area of solar pumped laser application is in communication. Large amounts of information can be transmitted at greater distances due to the higher power of the emitted laser energy which will be more effective than cable lines and microwaves. This also bodes well for space based laser communication.[xix]

One of the key parameters in using solar pumped lasers effectively is shared with solar thermal propulsion: the collection efficiency of the concentrator. The parabolic shape needs to be well defined and correctly manufactured in order to produce spot sizes small enough to generate high efficiencies without forcing the concentrator diameter to grow to an unfeasible size. Quantifying the actual shape of the concentrator is instrumental in determining the collection efficiency and ultimately the system performance. These collectors will continue to grow in size, so the measurement systems must either scale with the collector size or measure localized regions of the collector.

1.6 Previous Shape Measurement Approach

One approach developed at UAH is the Ronchi test using interferometric analysis software to extract the shape of the optic from the aberrations found in the return image. A Ronchi test is a variation of the scanning knife edge test except that a Ronchi ruling is a collection of many knife edges eliminating the need for scanning across the aperture. As the wavefront propagates through the Ronchi grating, portions of the aperture are obscured creating a fringe pattern. This method is expensive and requires a sophisticated setup, with the need of sophisticated software for analysis. Ken Pitalo at the Space Optics Manufacturing Technology Center (SOMTC) at the MSFC developed the setup for this approach and Dr. Phil Stahl developed the THIN software. The complex setup involves an interferometer and associated optics, specialized software for decoding the aberrated fringe pattern, a CCD, and other specialized equipment. A diagram depicting the setup and the membrane under test is shown below in Figure 1.10.

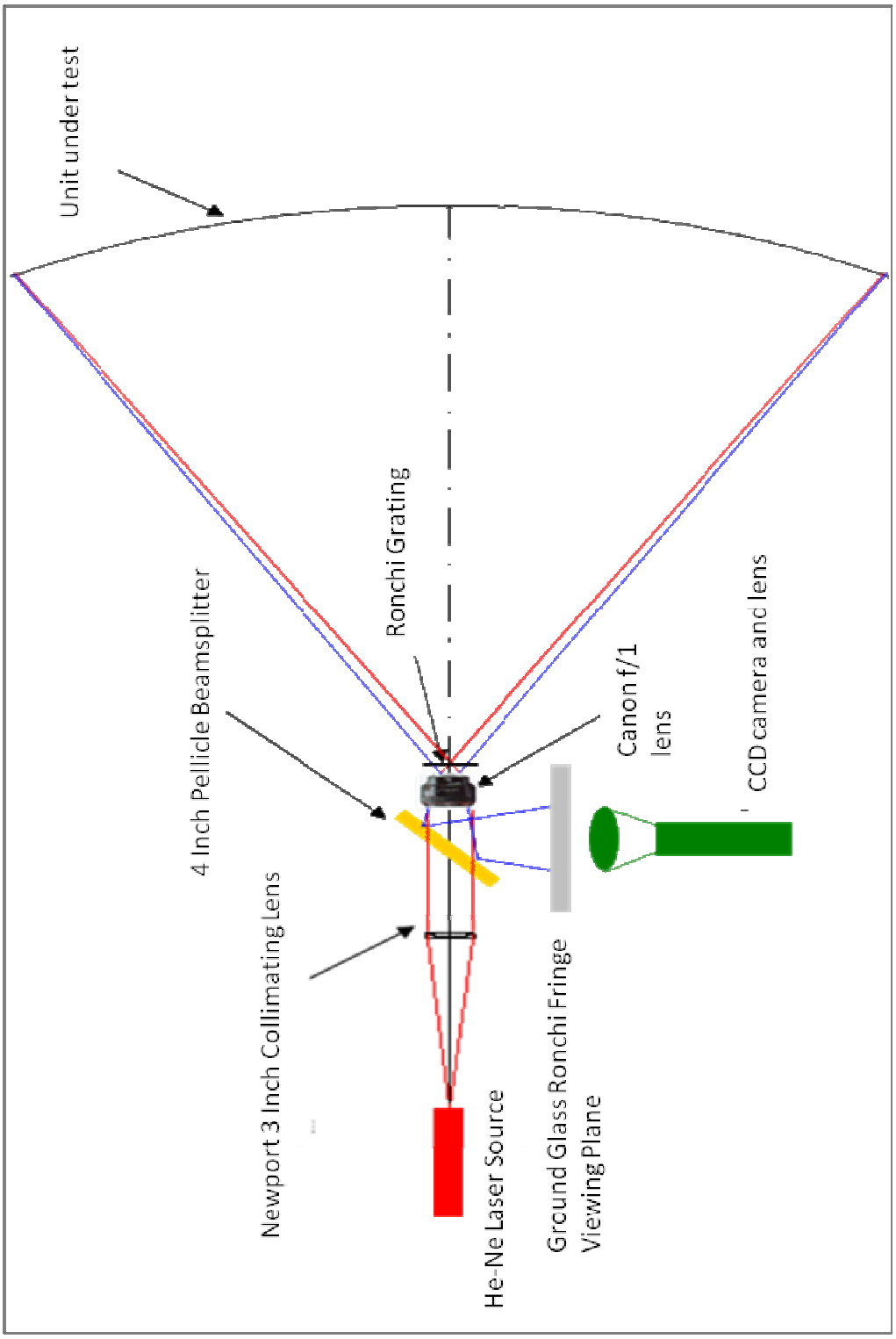

Figure 1.1 Large diameter mirror test setup at UAH using rochi ruling and fringe analysis.

Theoretically, this method shows some promise for providing shape information for large diameter optics. The Ronchi ruling test has already been tried on membranes (made from thin flexible material) of a smaller diameter (approximately 21 inches) in the optical testing lab at the University of Alabama-Huntsville (UAH). The resulting fringe pattern had too many aberrations present to extract the shape data. Figure 1.11 is a picture of the return image obtained in that Ronchi test performed at UAH. Note that the fringe pattern has been obscured to the point that no useful information can be extracted (some semblance of vertical bars should be evident in order to extract any reliable data).

Figure 1.11 Ronchigram produced by the Ronchi analysis test described above.

The above results provided the motivation to develop another method for shape measurement of large diameter thin film optics. This thesis will briefly describe some uses of solar concentrators and ultimately demonstrate a measurement method employed to test different diameter solar concentrators.

[i] Johnston, John. "Analysis and Test Technology for Thin-Film Membrane Structures." Analysis and Test Technology For Thin-Film Membrane Structures. http://femci.gsfc.nasa.gov/workshop/2001/posters/johnston/Johnston_Membrane.pdf (accessed September 15, 2010).

[ii] "DuPont™ Kapton® : Uses & Applications: Aerospace." DuPont. The Miracles of Science. http://www2.dupont.com/Kapton/en_US/uses_apps/aero/index.html (accessed August 20, 2010).

[iii] "Types of Solar Collectors, Solar Basics." Solar Water Heater, Solar Hot Water, Solar Hot Water Heater, Solar Heating, Solar Collector by Apricus. http://www.apricus.com/html/solar_typesofsolar.htm (accessed August 20, 2010).

[iv] "Science: Archimedes' Weapon." *Time*, November 26, 1973. http://www.time.com/time/magazine/article/0,9171,908175,00.html (accessed August 20, 2010).

[v] "Burning Mirrors." www.cs.drexel.edu. http://www.cs.drexel.edu/~crorres/Archimedes/Mirrors/Tzetzes.html (accessed September 1, 2010).

[vi] "Concentrated Solar Power." *Solar Thermal Magazine*, October 2004. http://www.solarthermalmagazine.com/learn-more/concentrated-solar-power-csp/ (accessed September 2, 2010).

[vii] "SolarPACES Home Page." SolarPACES. http://www.solarpaces.org/Tasks/Task1/ps10.htm (accessed September 2, 2010).

[viii] "Press Releases - Enel.com." Home - Enel.com. http://www.enel.com/en-GB/media/press_releases/release.aspx?iddoc=1634858 (accessed September 2, 2010).

[ix] Ombello, Carlo. "The World's First Molten Salt Concentrating Solar Power Plant | Environment | guardian.co.uk." Latest news, comment and reviews from the Guardian | guardian.co.uk. http://www.guardian.co.uk/environment/2010/jul/22/first-molten-salt-solar-power (accessed February 14, 2011).

[x] "Solar Insolation." Solar Water Heater, Solar Hot Water, Solar Hot Water Heater, Solar Heating, Solar Collector by Apricus. http://www.apricus.com/html/solar_collector_insolation.htm (accessed February 15, 2011).

[xi] "Current Projects." Current Projects. http://www.acrim.com/ (accessed April 4, 2011).

[xii] "Solar Spectral Irradiance: ASTM G-173." Renewable Resource Data Center (RReDC) Home Page. http://rredc.nrel.gov/solar/spectra/am1.5/ASTMG173/ASTMG173.html (accessed March 3, 2011).

[xiii] Nakamura, Takashi, Robert Krech, James McClanahan, James Shoji, Russell Partch, and Skylar Quinn. "Solar Thermal Propulsion for Small Spacecraft - Engineering System Development and Evaluation." sr-1228.pdf. www.psicorp.com/pdf/library/sr-1228.pdf (accessed October 2, 2010).

[xiv] "SART-Systemanalyse Raumtransport - Solar thermal propulsion." DLR Portal - Lampoldshausen. http://www.la.dlr.de/ra/sart/projects/sto/sto.php.en (accessed October 3, 2010).

[xv] Smith, Brett. "NASA Marshall Space Flight Center - Huntsville, AL: Solar Thermal Propulsion." Best Manufacturing Practices: Your Source for Best Practices and Innovative Technologies. http://www.bmpcoe.org/bestpractices/internal/nasam/nasam_32.html (accessed February 14, 2011).

[xvi] Sahara, Hironori, Morio Shimizu, Keitaro Osi, Kai Watanabe, and Yoshihiro Nakamura. "Solar Thermal Propulsion for Microsatellites End-of-life De-orbiting." 0085-0303iepc-full.pdf. sgc.engin.umich.edu/erps/IEPC_2003/proceedings/0085-0303iepc-full.pdf (accessed September 20, 2010).

[xvii] Hitz, Breck. "Can Lasers Help Decrease Our Dependence on Fossil Fuels? (Photonics Spectra | Sep 2007 | Tech News)." Photonics.com: Optics, Lasers, Imaging & Fiber Information Resource. http://www.photonics.com/Article.aspx?AID=30649 (accessed September 14, 2010).

[xviii] "Physics-sun solar laser oozes millions of watts." Solar Feeds News Network. http://solarfeeds.com/index.php?option=com_content&view=article&id=2820:physics-sun-solar-laser-oozes-millions-of-watts&catid=76:ecofriend&Itemid=112 (accessed September 13, 2010).

[xix] Yakhyaev, Anvar. "Uzbek Scientists Created a Powerful Solar Laser." *Uzbekistan Today* (Tashkent), November 16, 2007. http://www.ut.uz/eng/today/uzbek_scientists_created_a_powerful_solar_laser.mgr (accessed September 13, 2010).

CHAPTER 2

ABERRANT BEHAVIOR

2.1 Imperfect Imaging

Basic imaging principles dictate that for a perfect imaging system, all ray paths have the same optical path length from the object plane to the image plane.[i] In this ideal system, the image of a true point source through an optical system with circular apertures will result in an intensity or irradiance distribution proportional to the square of a Bessel function of the first kind, more commonly known as the Airy pattern as seen in Figure 2.1.[ii] The central region is referred to as the Airy disc and its diameter is given by the expression $d=2.44*\lambda*f/\#$, where λ is the wavelength of the light and f/# is the f-number of the system and defined as the focal length divided by the entrance pupil diameter of the lens.[i]

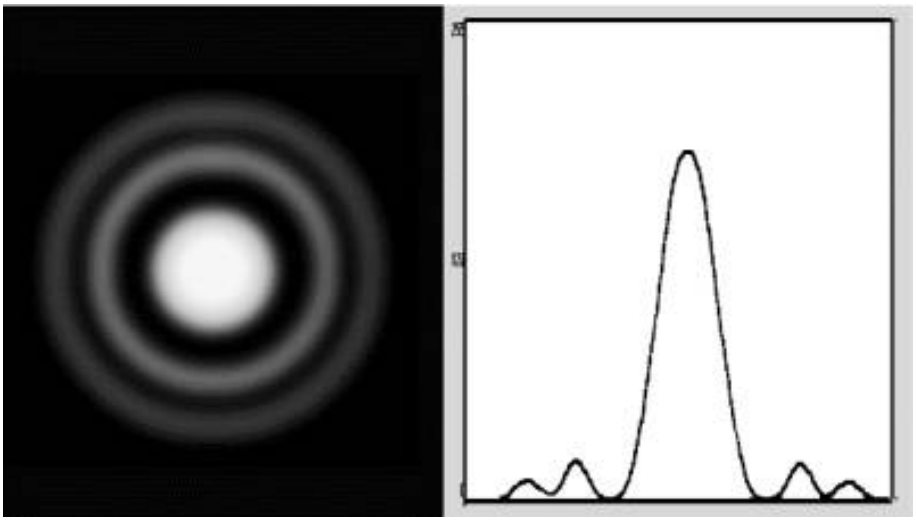

Figure 2.1 Contour and cross-section of Airy profile.[iii]

After passing through the optical system, the once spherical wavefront (SWF) is modified due to imperfect shapes, gradient indices of refraction, and other real world factors. This produces a non-ideal wavefront in the exit pupil, thus producing aberrated images. The amount of deviation of this new wavefront relative to a reference spherical wavefront is referred to as the optical path difference (OPD). The OPD is positive if the aberrated wavefront leads the ideal wavefront as shown in Figure 2.2.[ii]

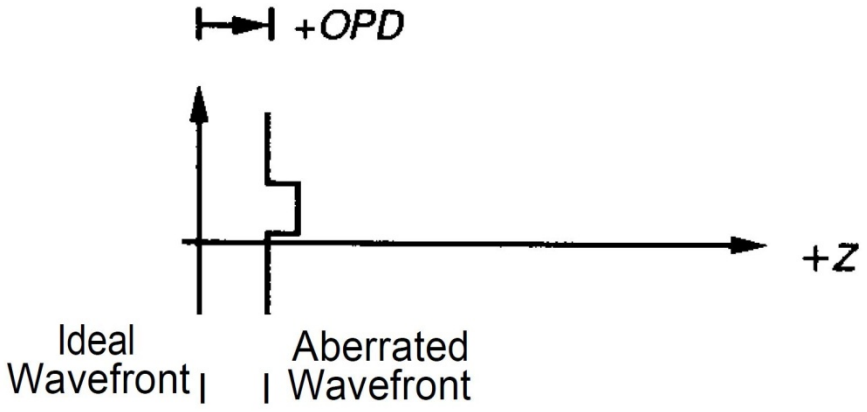

Figure 2.2 Illustration depicting definition of OPD, the difference between the aberrated wavefront and an ideal wavefront.[ii]

These deviations, or aberrations, can be measured at the exit pupil using the non-ideal, or aberrated, wavefront (AWF) or at the image plane using measurements taken on the image. The measurements taken at the image plane use exact ray tracing to find where a particular ray will cross the optical axis and intercept the Gaussian, or paraxial, image plane. This Gaussian image plane is located at the center of the reference sphere centered on the exit pupil; therefore perfect rays will all intersect at the Gaussian image plane. However, rays from the aberrated wavefront will cross the optical axis at various points, as shown in Figure 2.3 and will intercept the Gaussian image plane at different distances from the optical axis.[iv]

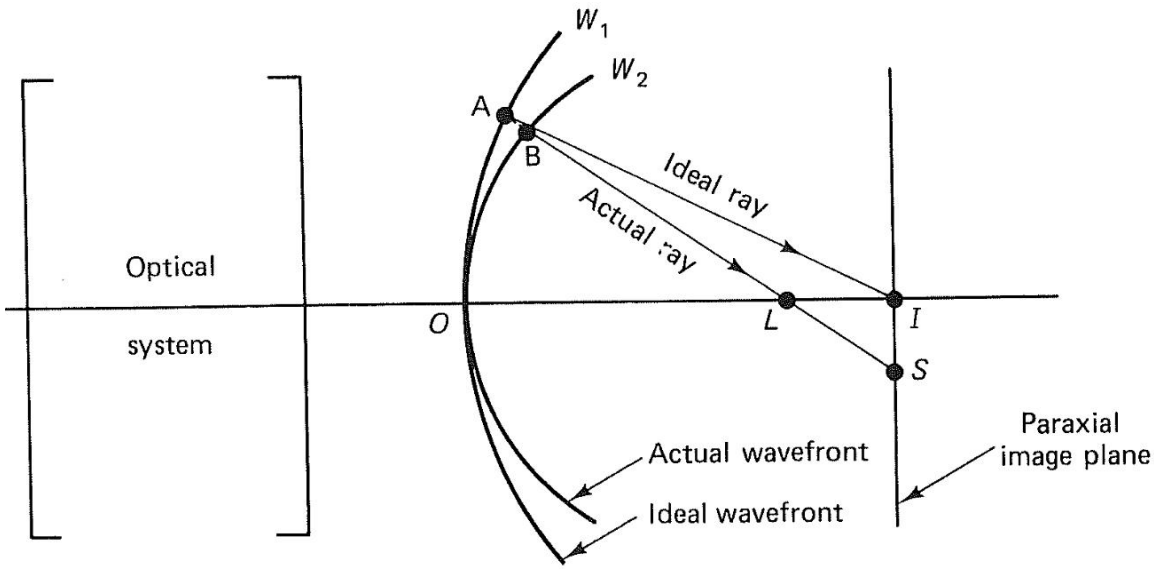

Figure 2.3 Basic pictorial showing the location of optic axis crossing and paraxial plane intercept for aberrated wavefront rays.[vii]

There are two basic polynomial representations describing wavefront aberrations in the exit pupil: Seidel and Zernike. The ray aberrations used by optical designers in imaging systems paved the way for the emergence of the Seidel polynomial expression

and the Zernike representation is typically used by optical testers.[i] The wavefront aberrations at the exit pupil will be chosen for further discussion primarily due to the fact that wavefront aberration is a more fundamental concept than the ray aberration approach and does not depend on whether the conjugates are finite or at infinity.[v] The amount of OPD measured between the AWF and a SWF is the total systen aberration, W, represented in the following Seidel equation:[i]

$$\mathbf{W} = \sum_{\mathbf{ijk}} \mathbf{W_{ijk}} * \bar{\mathbf{H}}^{\mathbf{i}} * \boldsymbol{\rho}^{\mathbf{j}} * \mathbf{cos}^{\mathbf{k}}(\boldsymbol{\varphi}), \qquad \textbf{(2.1)}$$

where H is the normalized field coordinate, ρ is the normalized pupil coordinate, and φ the angle from the horizontal where the ray intersects the exit pupil. Knowing *W, H,* ρ and φ, the amount each individual aberration contributes to the overall can be calculated. The W_{ijk} term in the expression is a coefficient representing a particular aberration and typically has units of length to retain dimensionality.[i] The mathematical treatment that will follow uses the convention of positive angles being measured clockwise from the y-axis as seen in most optical testing and geometrical optics books, such as *Optical Testing* by J. Geary and *Introduction to Optics* by F. Pedrotti and L. Pedrotti. This is illustrated in Figure 2.4.

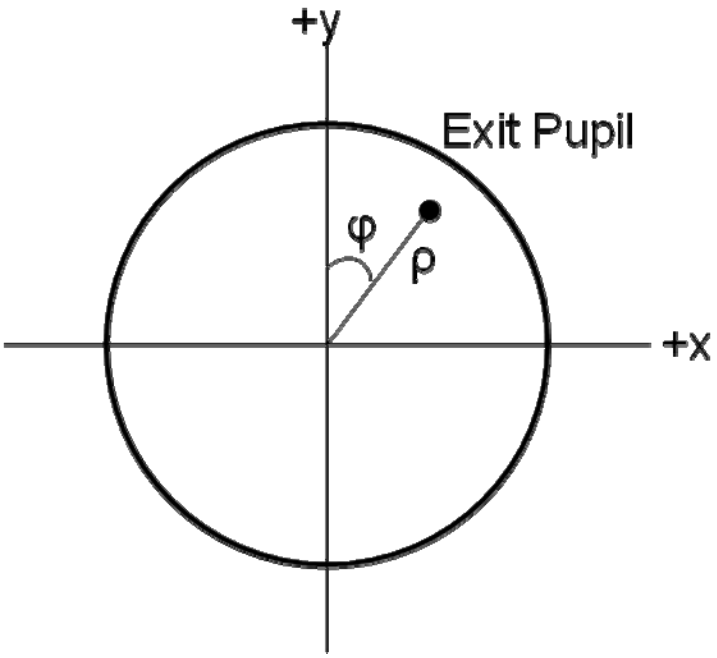

Figure 2.4 Mathematical convention for Seidel aberrations.

These departures from ideal, or Gaussian, conditions, fall into two main categories of aberrations: chromatic aberrations and monochromatic aberrations. All subsequent discussions throughout this thesis will involve monochromatic aberrations since the optics under analysis are reflective in nature and have no significant dependence on the wavelength of visible light.[vi] These monochromatic aberrations are related to the first eight terms of the Seidel expansion in which the first three represent piston (W_{200}), tilt (W_{111}), and defocus (W_{020}). Piston and tilt are not true aberrations because they do not affect the shape of the wavefront; therefore defocus is truly the only first-order aberration. The next five terms of the above expansion where $i + j = 4$ are known as the Seidel, or third-order, aberrations. These terms are named spherical aberration (W_{040}), coma (W_{131}), astigmatism (W_{222}), field curvature (W_{220}), and distortion (W_{311}). The first three affect the shape of the point spread function (PSF), or Airy pattern, which in turn

blurs the image and the other two affect the position of the PSF.[i] Using the above information, it is possible to quantify the wavefront of a large diameter thin-film optic and subsequently calculate the Seidel aberrations for image quality prediction.

2.2 W020 – Defocus

The term defocus is also referred to as longitudinal focus shift with a dependence on the square of the normalized pupil radius, ρ. Mathematically this indicates that the reference sphere and aberrated sphere are identical except in radius of curvature as can be seen in the equation

$$\Delta \mathbf{W} = \mathbf{W_{020}} * \boldsymbol{\rho}^{\mathbf{2}}. \qquad \textbf{(2.2)}$$

To correct for this aberration, the radius of the reference sphere can be changed, which means selecting a different Gaussian focal plane location. Since there is no true wavefront deformity, some researchers do not refer to defocus as an aberration but it is convenient to treat it as such since it interacts with other aberrations such as spherical aberration and astigmatism.[v] Figure 2.3 above is actually depicting defocus. In Figure 2.5, the 3-dimensional wavefront map and a 2-dimensinal contour map are shown for defocus.

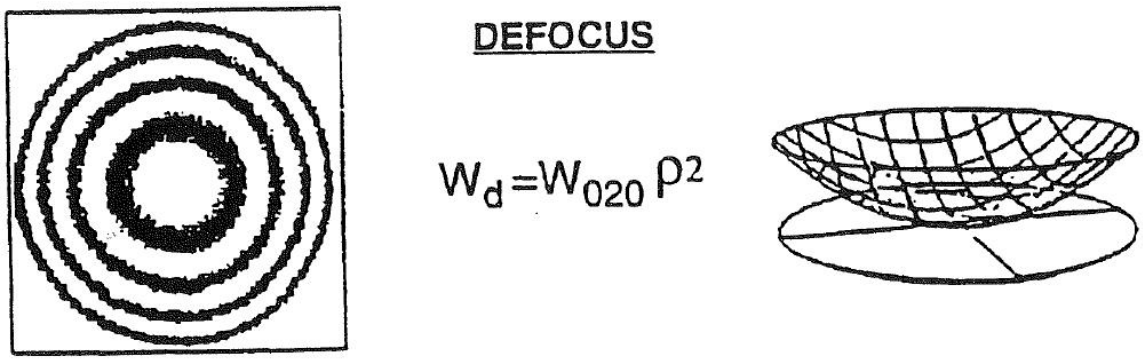

Figure 2.5 3-d wavefront and 2-d contour map of defocus.[i]

The quadratic dependence on the pupil position is visualized in the 3D representation of the wavefront on the right. This illustrates a wavefront with defocus present and its relation to the reference sphere. The contour plot on the left of the figure shows a 2D representation of the wavefront with each contour line representing a one wave of defocus.

2.3 W_{040} – Spherical Aberration

Sir Isaac Newton provided a description of spherical aberration in *Opticks* which states:

> if [rays] flow from a lucid Point, so very remote from the Lens, that before their Incidence they may be accounted parallel, the Focus of the most refrangible Rays shall be nearer to the Lens than the Focus of the least refrangible, by about the 27^{th} or 28^{th} Part of their whole distance from it. And the Diameter of the Circle in the middle Space between those two Foci…is about the 55^{th} part of the Diameter of the Aperture of the Glass. So that 'tis a wonder, that Telescopes represent Objects so distinctly as they do. [Newton *Opticks*]

To rephrase: the marginal rays, or rays near the edge of the pupil will be refracted more, thus focusing before the paraxial rays. This is illustrated in Figure 2.6.

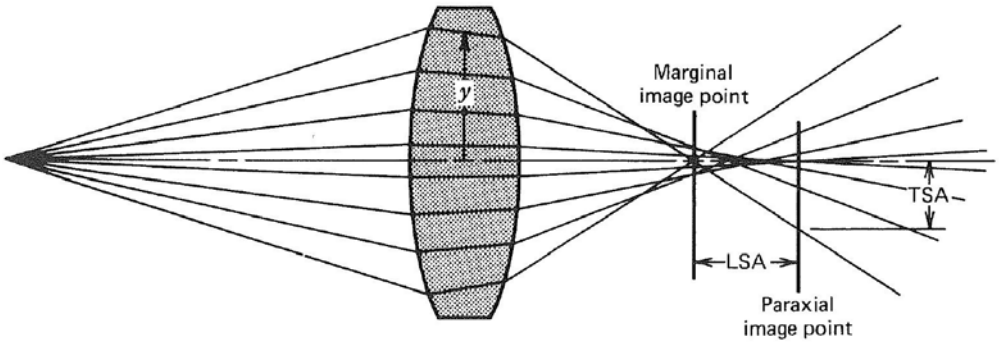

Figure 2.6 Graphical ray depiction of spherical aberration. [iv]

This particular component of spherical aberration is commonly referred to as longitudinal spherical aberration (LSA) and is the distance from the paraxial focus to the marginal ray focus. When the marginal ray focus is located in front of the paraxial focus, the LSA is said to be positive which is typical for a standard converging positive lens. Whereas with a negative lens the marginal ray focus is after the paraxial focus producing a negative LSA. [vi] There exists a point on the paraxial image plane where the marginal ray intercepts. The distance from this point to the optical axis is denoted as transverse spherical aberration (TSA). At some intermediate point along the optic axis between the

marginal ray focus and the paraxial ray focus; there exists a point of "best" focus which is called the *circle of least confusion* or *minimum blur* depicted in Figure 2.7.[vii] This is the point where the diameter of the ray bundle is the smallest thus producing the least amount of blur in the image.

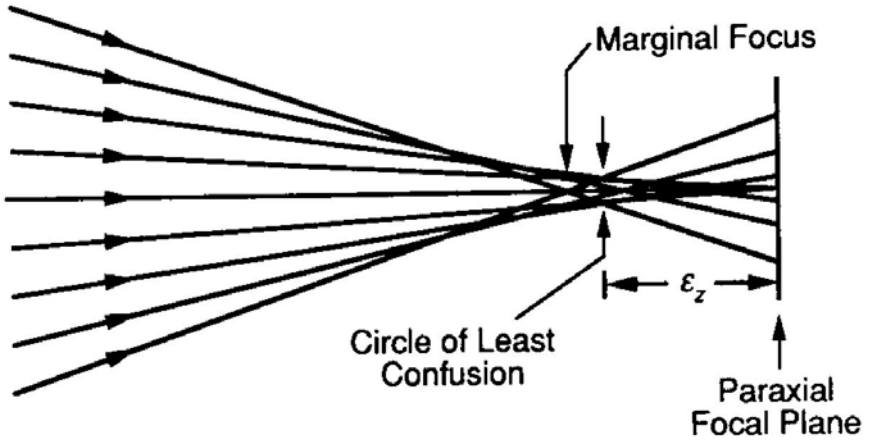

Figure 2.7 Illustration from Wyant and Creath showing the location of the circle of least confusion and its relation to the paraxial focal plane.[ii]

Like defocus, spherical aberration is dependent only on the pupil position (as can be seen in the Seidel expression for spherical aberration below), but instead of the square relationship, spherical aberration varies as the pupil position to the fourth power.

$$\Delta W = W_{040} * \rho^4. \quad (2.3)$$

This equation describes the effect spherical aberration has on the wavefront, or conversely, if the wavefront is known, the amount of spherical aberration created by the deformed wavefront. By knowing the wavefront error, the spherical aberration coefficient can be calculated from the above expression. A representation of a wavefront that creates spherical aberration is shown in Figure 2.8.

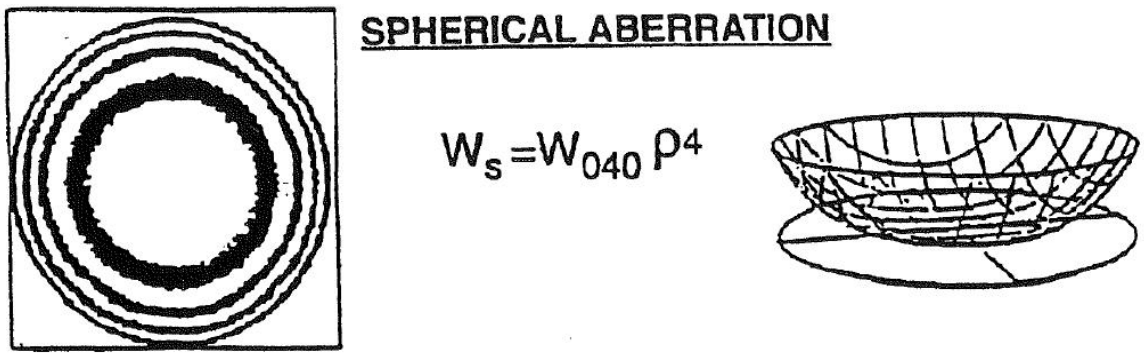

Figure 2.8 Spherical aberration plots showing a 3-dimensional wavefront and the corresponding 2-dimensional contour plot.[i]

The quartic dependence on the pupil position is visualized in the 3D representation of the wavefront on the right. This illustrates a wavefront with spherical aberration present and its relation to the reference sphere. The contour plot on the left of the figure shows a 2D representation of the wavefront with each contour line representing a one wave of spherical aberration. Spherical aberration, the first primary aberration, is typically the largest contributor to the overall deformed wavefront and optical designers tend to correct for spherical aberration before any other aberrations since the magnitude of the spherical aberration is sometimes great enough to mask the effects of the other primary aberrations. This aberration is a major concern for solar collectors due to the loss of collection efficiency if the absorber is placed in the wrong location. This is the primary reason most, if not all, solar collectors are parabolic in shape to eliminate spherical aberration.

2.4 W_{131} – Coma

The next primary aberration that pertains to this research is comatic aberration, commonly referred to as coma. Coma is one of the field dependent image degrading aberrations with its effect worsening as the object is displaced farther from the optic axis.

Coma exists because the off-axis portions of the lens have different effective focal lengths which will cause the off-axis rays to focus at a different intercept point in the paraxial image plane, assuming there is no spherical aberration present.[vi] For the remainder of this brief discussion of coma, the assumption will be that there is no spherical aberration present. This effect of coma is shown geometrically in Figure 2.9.

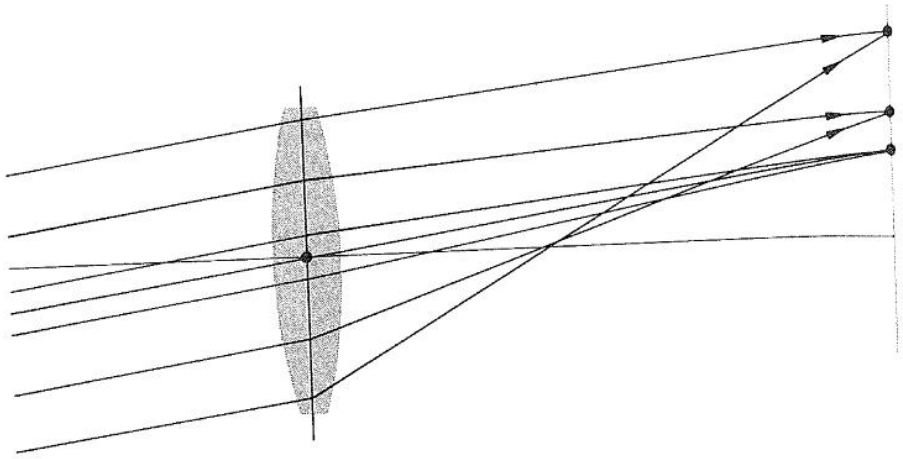

Figure 2.9 2-dimensional ray trace illustrating the effect of coma on the ray intersections.[vi]

The diagram above shows an exaggerated two-dimensional representation of the effect of coma on the ray bundle. Examining this aberration around the lens (three-dimensionally) each set of ray bundles will form a ring at the paraxial image plane. The term *comatic circle* was penned by H. Dennis Taylor to describe this ring as viewed at the image plane which is illustrated graphically in Figure 2.10.[vi]

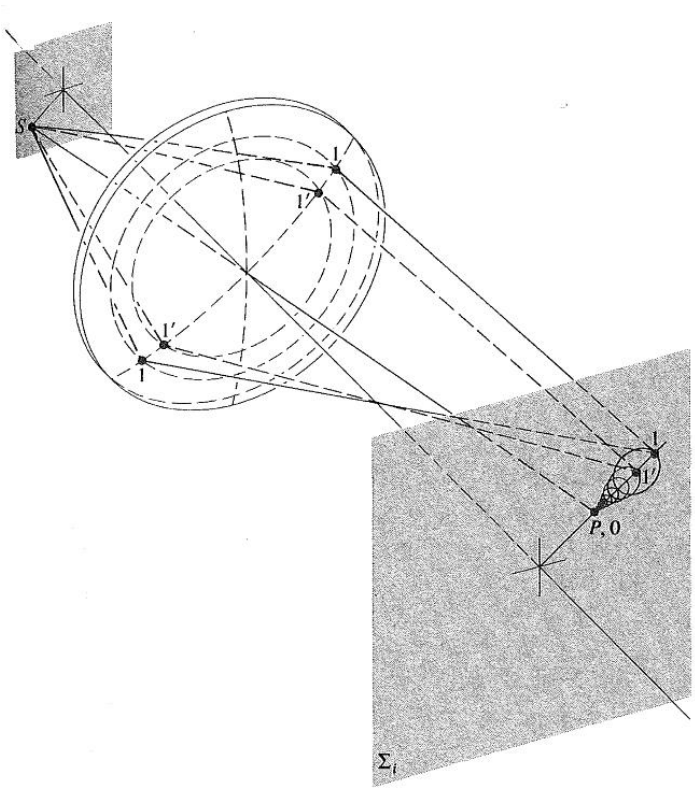

Figure 2.10 3-dimensional representation of coma showing the creation of the comatic circle.[vi]

Coma is generally considered to be the worst of all the aberrations since it presents itself in an asymmetric configuration as evident in the coma flare.[vi] The coma term in the Seidel expansion is

$$\Delta \mathbf{W} = \mathbf{W_{131}} * \bar{\mathbf{H}} * \boldsymbol{\rho}^{\mathbf{3}} * \mathbf{cos}(\boldsymbol{\varphi}), \qquad \textbf{(2.4)}$$

where H is the normalized field position, ρ is the normalized pupil radius, and φ is the angle from the +y axis in the pupil plane. Compared to spherical aberration, there are more individual contributors to the overall comatic effect even though dependence on pupil radius has been decreased; The field dependence is clearly evident. Geometrically speaking, the amount of coma cannot be decreased by shifting the focal plane, as in

spherical aberration and defocus, but rather a wavefront tilt is required to produce a clearer image spot. This is apparent when viewing a wavefront consisting of coma as given in Figure 2.11.

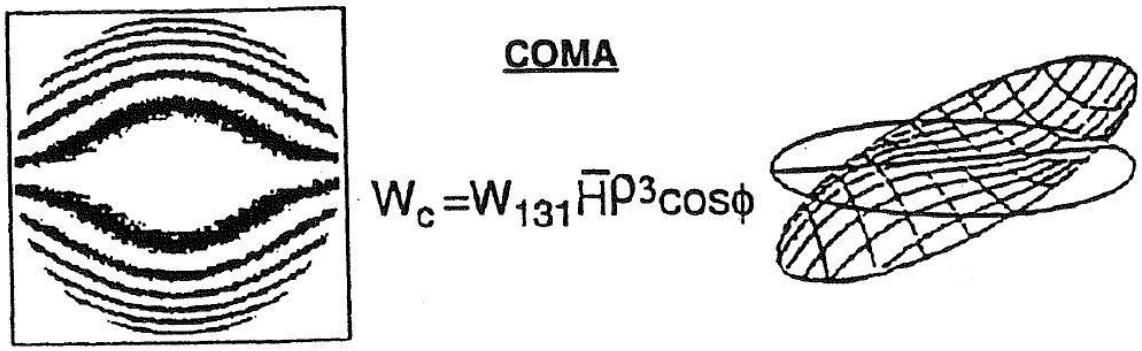

Figure 2.11 Wavefront map showing tilted nature of coma and the corresponding 2-d contour plot.[i]

The cubic dependence on the pupil position is visualized in the 3D representation of the wavefront on the right. This illustrates a wavefront with pure coma present and its relation to the reference sphere. The contour plot on the left of the figure shows a 2D representation of the wavefront with each contour line representing a one wave of coma.

The focused spot diameter is the primary parameter solar collector designers want to minimize, thereby maximizing the collection efficiency. The odd shape that is traditionally generated by coma would increase the overall diameter of the spot which would decrease the collection efficiency. However, since these optics are designed for collecting solar energy, most systems have tracking hardware in place to follow the path of the sun, keeping the field angles fairly small thus minimizing the field dependent nature of coma.

2.5 W_{222} – Astigmatism

The next field dependent aberration of interest is astigmatism, which is simply explained as: a ray fan contained within a plane will come to focus at a different position along the optic axis than a ray fan from another plane. Typically, this aberration is divided into tangential and sagittal components, with the tangential ray fan being contained within a plane that is tangent to the optic axis and the sagittal ray fan being contained within a plane that is orthogonal to the tangential, or meridional, plane. As a result of the different focus locations for the orthogonal set of ray fans, two line foci at right angles to each other are formed. In most cases, the sagittal focus will occur after the tangential but before the paraxial focus as illustrated below in Figure 2.12.[iv]

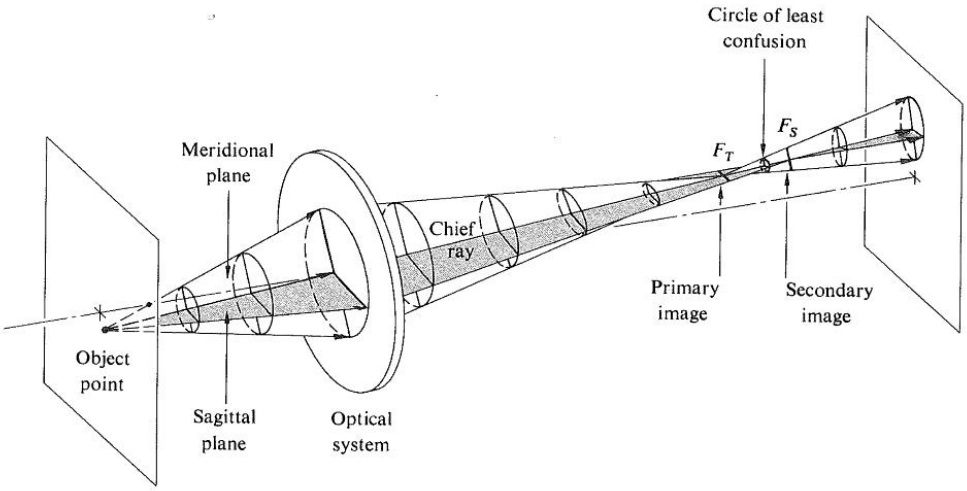

Figure 2.12. Graphical illustration of astigmatism and the circle of least confusion.[vi]

Between the horizontal line and the vertical line, a central circular region is formed between the two and this region is termed the *circle of least confusion*.[iv] This is considered to be the best compromise focal plane for minimum image blur just as it was

for spherical aberration. For axial objects, and in the absence of spherical aberration, the ray configurations for both planes are identical and so are as the focal lengths, thus forcing all the rays to a single focus.[vi] As the object moves off-axis and the angle becomes more oblique, one set of ray fans will be tilted more thus creating a shorter focal length than the orthogonal ray fan set. This focal length difference, or astigmatic difference, increases quite rapidly as the object moves further off-axis.[vi] This dependence is shown in the Seidel expression for astigmatism which is

$$\Delta \mathbf{W} = \mathbf{W_{222}} * \bar{\mathbf{H}}^{\mathbf{2}} * \boldsymbol{\rho}^{\mathbf{2}} * \mathbf{cos}(\boldsymbol{\varphi}), \qquad \textbf{(2.5)}$$

where the field dependence is now squared, the radial position in the pupil has a decreased dependence, and the angular coordinate dependence is increased to quadratic compared to coma's linear dependence. As the object moves more off-axis, the circle of least confusion increases in diameter thus causing the image quality to suffer. The image will lose detail around the edge of the circle as it increases in diameter.[vi] Figure 2.13 gives a graphical wavefront representation of astigmatism.

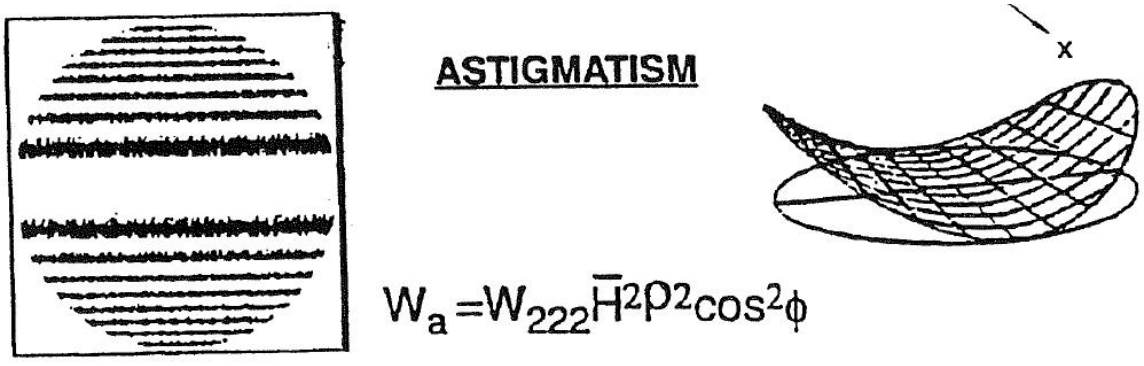

Figure 2.13 Wavefront representation of astigmatism. Notice the asymmetric curvature.[i]

The quadratic dependence on the pupil position is visualized in the 3D representation of the wavefront on the right. This illustrates a wavefront with pure astigmatism present and its relation to the reference sphere. The contour plot on the left of the figure shows a 2D representation of the wavefront with each contour line representing a one wave of astigmatism.

The effect of coma, the other field dependent aberration, and astigmatism on solar collectors employing a sun tracking system, should be minimal. With continuous tracking, the sun will remain approximately on axis, keeping the *circle of least confusion* to a minimum diameter. One idea to keep in mind is the relationship between astigmatism and the fourth primary aberration, known as field curvature.

2.6 W_{220} - Field Curvature

Astigmatism and field curvature are closely related and typically their wavefront aberration terms are combined into a single expression. Both aberrations are field and aperture dependent, however as astigmatism is reduced, the tangential and sagittal focal planes are made to coincide, a curved focal surface is formed. This curved focal surface is termed field curvature. Field curvature can be nullified or reduced by the addition of a field flattener just before the image plane.[vii] A field flattener is an optical element which is designed to shift the local focus to the paraxial image plane. This is usually accomplished by varying the thickness as a function of height. Field curvature is not applicable to solar collectors due to the on-axis nature and the ability to shift the focal plane to the point of producing the smallest spot diameter, keeping collection efficiency at a maximum.

2.7 W_{311} - Distortion

The fifth and final primary aberration is distortion, and it is defined by a change in magnification as the object moves off-axis.[vii] The image is still well focused but appears to be misshapen. There are two main types of distortion, one for an increase in magnification with radial distance, and one for a decrease in magnification with radial distance. These two distortions are named pincushion and barrel, respectively.[vi] Since distortion does not affect quality, just location of images, it is of little concern for solar collectors.

---

[i] Geary, Joseph M.. *Introduction to optical testing*. Bellingham, Wash., USA: SPIE Optical Engineering Press, 1993.

[ii] Wyant, James, and Katherine Kreath. "Aberrations and Optical Testing." www.optics.arizona.edu. www.optics.arizona.edu/jcwyant/optics513/ChapterNotes/Chapter03/BasicAberrationsandOpticalTesting.pdf (accessed September 2, 2010).

[iii] Liverpool John Moores University. "Astrophysics Research Institute." Astrophysics Research Institute. www.astro.ljmu.ac.uk/courses/phys134/pic/scope/airydisk.jpg (accessed April 15, 2011).

[iv] O'Shea, Donald C. *Elements of modern optical design*. New York: Wiley, 1985.

[v] Mouroulis, Pantazis, and John Macdonald. *Geometrical optics and optical design*. New York: Oxford University Press, 1997.

[vi] Hecht, Eugene, and Alfred Zajac. *Optics / Eugene Hecht; with contributions by Alfred Zajac*. 2nd ed. Reading, Mass.: Addision-Wesley, 1987.

[vii] Pedrotti, Frank L., and Leno S. Pedrotti. *Introduction to Optics*. Englewood Cliffs, N.J.: Prentice-Hall, 1987.

CHAPTER 3

METHODOLOGY

3.1 Measurement Technique

Several applications of solar collectors have been discussed in previous chapters, but all of them are characterized by the amount of energy collected and the profile of the focused spot, or rather focus volume for some applications. The shape and surface figure of the collector is a major contributor to malformed or aberrated spots and focus volumes. The interferometric method briefly presented earlier is a valid testing method for determining the surface profile of optics; however, with large thin-film collectors, the magnitude of the aberrations typically overwhelms the ability to discern any shape information from the interferogram.

The measurement method developed in the present research utilizes simple geometric relationships to ultimately determine the local tilt of the optic at a particular location. Based on the local tilts, a surface map can then be generated. This method relies on a source laser and observations of the reflected beam from the optic. Alignment of the laser to the center of the lens was crucial to the reliability of the data. This was achieved by using an additional optical rail fixed and oriented perpendicular to the rail

used for translation of the mounted laser. The laser was mounted such that the front and rear alignments could be manipulated independent of each other, which allowed for a more accurate and stable alignment scheme. An adjustable iris was then placed on the perpendicular rail with the iris stopped down to the minimum diameter. The laser was turned on and aligned such that the beam was incident on the center of the iris. The laser was considered to be aligned, forming an optical axis, when the beam location on the iris remained constant as the iris was translated from one end of the rail to the other. Once an optical axis was achieved, the laser was then aligned to the center of the optic by translating it in the x and y directions until the return beam was reflected back into the aperture of the laser. The laser was then translated across the surface of the lens in 1cm increments with the center of each return beam marked on the observation wall. For each data point collected, the shape of the optic was determined using simple geometric relations derived using Figure 3.1.

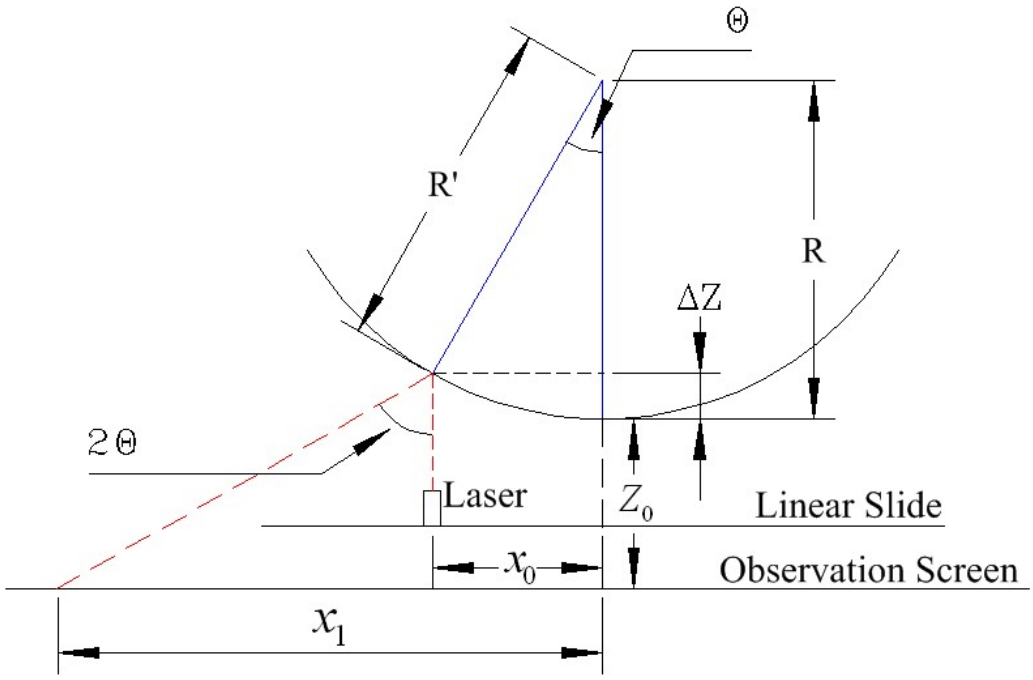

Figure 3.1 Geometrical relationships used to detemine the shape of the optic.

The optics tested were heat formed thin membranes with a thickness of 75 μm. This very flexible membrane was supplied by the manufacturer already mounted to a wooden ring. Mounting holes were drilled into this wooden structure to allow mounting to a rotation mount. The rotation mount was a large bearing approximately 17" in diameter. The ring/optic combination was mounted to the inner ring of the bearing and the outer ring was fixed to two optical posts. This setup allowed the optic and inner ring to rotate, thus providing a simple way to completely scan the optic.

3.2 Instrumentation

The accuracy of the measurement method depends on the instrumentation used as part of the measurement setup. Two optical rails were used for accurately positioning the

laser for measurement of $x_0$and the mirror method added a rotation stage for accurately measuring the value of θ. As the measurement system is scaled up for larger optics and automated, finer resolution measuring equipment can be employed.

Equipment used:

- Oriel optical rail with 1 mm vernier scale and teeth for use of fine position carriage
- Oriel carriage for laser diode with fine position knob
- Melles Griot 635 nm laser diode
- Melles Griot laser diode mount housing
- CVI rotation mount for the analysis mirror with arcminute vernier

3.3 Experimental Method #1 (0.5 m optic)

The first experimental method consisted of measuring the location of a reflected laser beam to ultimately determine to the shape through the geometrical relationships illustrated in Figure 3.1. The reflected beam location, on a wall parallel to the scanning direction, was measured relative to the zero location of the on-axis reflection from the center of the optic. The ring of the optic was marked with 5 degree increments around the circumference to be used as a guide for rotating the optic known amounts between scan intervals. The optical rail used to translate the mounted laser was positioned perpendicular to the orientation of the optic so that the laser could scan the front convex surface. Using optical mounts and optical rails fixed to an optical table helped insure precise alignment and the optical table was positioned parallel to the wall used for observation. A picture of the mounted optic, alignment laser, and optical rails is shown below in Figure 3.2.

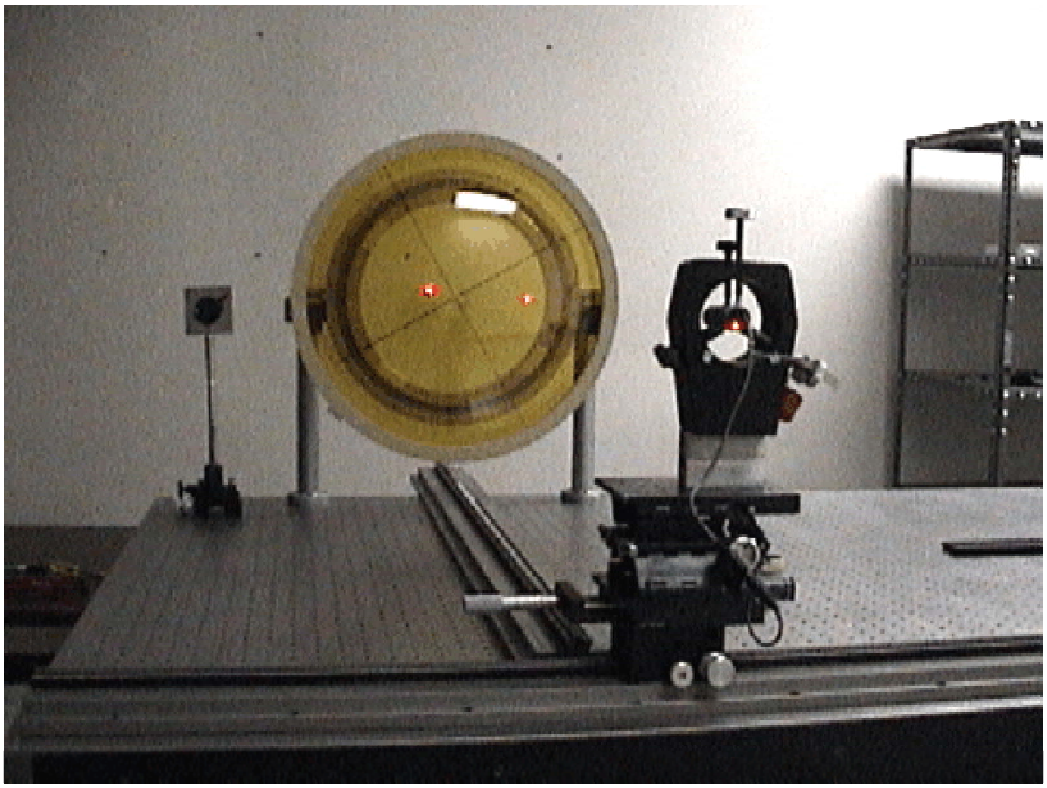

Figure 3.2. Method #1 experimental setup. View is from the observation screen. The optic shown is approximately 50 cm in diameter.

3.3.1 Experimental Method #1 Data Reduction Equations

The following equations are based on Figure 3.1. These equations are only valid for reduction method #1 which requires the solutions to a transcendental equation to determine θ at each scan point. Once θ is known, the radius of curvature and ultimately the local tilt for each scan point can be calculated. The surface shape can then be constructed from the local tilts. The measured values, from Figure 3.1, are as follows: x_0 represents the radial scan location, x_1 is the reflected beam location (RBL), and Z_0 is the distance from the vertex of the optic to the observation screen. The other values are calculated parameters with R being the nominal radius of curvature, R' is the local radius

of curvature for a particular radial scan point, ΔZ is the sag of the surface, and θ is the angle from the optic axis to the scan point. The ultimate goal was to calculate ΔZ, effectively creating a surface map. Using the measured values, an expression for 2θ can be written as

$$\tan 2\theta = \frac{x_1 - x_0}{Z_0 + \Delta Z}, \tag{3.1}$$

where ΔZ is the only unknown on the right hand side of the equation. This quantity is the distance from the vertex of the optic to the inspection point along an axis parallel to the primary optical axis. From Figure 3.1, the relevant data reduction equations are

$$\tan \theta = \frac{x_0}{R - \Delta Z}, \tag{3.2}$$

$$\Delta Z = R - \frac{x_0}{\tan \theta}, \text{ and} \tag{3.3}$$

$$R' = \frac{x_0}{\sin \theta}. \tag{3.4}$$

In order to determine R, several assumptions were made which proved to be valid when compared to a later calculation of R. These assumptions were choosing $x_0 = 0.5\ cm$ and assuming . Later data will validate the $\Delta Z = 0$ assumption by showing the $\Delta Z's$ calculated at these scan points near the vertex are approximately 0.05% of the total sag. The nominal radius of curvature was calculated by using equation (3.2) and equation (3.4) and averaging all the $R's$ for each rotation of the optic. Substituting equation (3.3) into equation (3.1), the resulting transcendental equation is

$$\tan 2\theta = \frac{x_1 - x_0}{Z_0 + \left[R - \frac{x_0}{\tan \theta}\right]}. \tag{3.5}$$

Using MATLAB, an algorithm was developed to find the zeroes of the above function, which in this case correspond to θ for each scan point. This algorithm required an initial guess for the value of θ and would iterate until a solution was reached. After exploring various trigonometric identities to solve this equation and substituting in for $tan\,(2\theta)$, the following quadratic expression was obtained

$$\boldsymbol{\theta = \tan^{-1}\left(\frac{-(Z_0 + R) \pm \sqrt{Z_0 + R + x_1^2 - x_0^2}}{x_1 - x_0}\right).} \qquad \textbf{(3.6)}$$

This equation aided in verifying the results of the MATLAB algorithm to find the solution to the transcendental equation. However, a measurement technique presented later in this thesis will show how a direct measurement of θ was possible. For small angles (or scan points near the vertex), $R' \approx R$. Once θ is determined, it is trivial to calculate $R', \Delta Z$, and ultimately the local tilt for a particular scan point. Using equation (3.4) to determine the local radius for each point and equation (3.3), the sag, ΔZ, can be calculated.

The outcome of the data reduction identified numerous potential sources of error and as a result, a plan was developed to eliminate some of them. The first error source was the lack of an absolute zero reference. Even though the laser (source laser) was centered on the optic, the absolute zero point on the observation screen was not known, and it could only be approximated. A reference laser was then introduced into the system. This laser was placed on the rail perpendicular to the scan direction pointing

toward the observation screen after the source laser was centered on the optic and an optic axis determined. The source laser was then removed and the reference laser produced a spot on the observation screen that defined the absolute reference point. This eliminated one source of error. The other main source of error was measurement accuracy of the reflected beam location which led to the development of measurement method #2.

3.4 Experimental Method #2 (0.5 m optic)

The measurement error concern led to the development of a new measurement architecture which eliminated the observation screen. This new method introduced a flat mirror into the system to produce a direct measurement of the local radius of curvature of the optic at a particular scan location. This mirror was rotated until the return beam spot was coincident with the reflected beam spot from the optic. If the measurement mirror is normal to the initial reflected beam, the beam reflecting from the measurement mirror travels back to the optic and continues to the aperture of the source laser. This direct measurement of the reflected beam angle is simply related to the local tilt of the optic at a particular scan location. The previous method required θ to be calculated from several measurements with each contributing to the overall error in θ. The only error source in the direct measurement of θ was the measurement accuracy of the rotation stage. Figure 3.3 illustrates this direct measurement and the corresponding geometrical relationships.

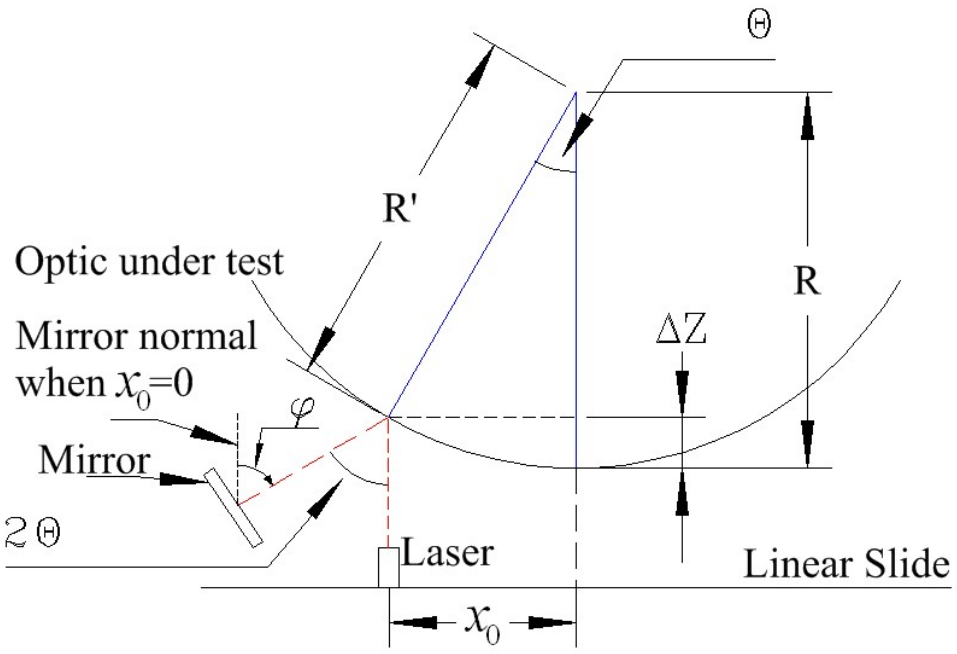

Figure 3.3. Experimental Method #2 geometrical relationships.

3.4.1 Method #2 Data Reduction Equations

This method uses equations (3.3) and (3.4) which are only valid for reduction method #2. This greatly reduced data collection time and improved accuracy. Once θ is known, the radius of curvature and local tilt for each scan point can be calculated. The surface shape can then be constructed from the local tilts. In Figure 3.3, the measured values are as follows: x_0 represents the scan location and φ, the amount the mirror is rotated from horizontal to retro-reflect the beam back onto the optic. Based on the law of reflection and the fact that the surface normal at that point is collinear with the radius at that point, $\varphi = 2\theta$. Since θ has been directly measured, there is no need for any additional calculations other than solving for R' and ΔZ, both of which can be found using equations (3.4) and (3.3), respectively.

3.5 Experimental Method #3 (1.0 m optic)

The method used for a large 1.0 m diameter optic was very similar to method #2 (mirror method) except the complete setup was rotated 90 degrees so that gravity would not cause the optic to sag. This involved suspending the optic and mounting the laser and measurement mirror underneath. This being a new procedure brought about another set of problems which had to be addressed. The spatial stability of the optic was one of the problems along with leveling the optic. To help solve the stability of the optic, different suspension techniques were examined. Figure 3.4 shows the 1.0 m optic suspended from the ceiling in a floating configuration. This proved to be unstable so another method was developed. A support structure was built from aluminum square tubing and the rotary optic mount was attached to this rack. This structure, shown in Figure 3.5, provided a very stable mounting configuration for the large optic.

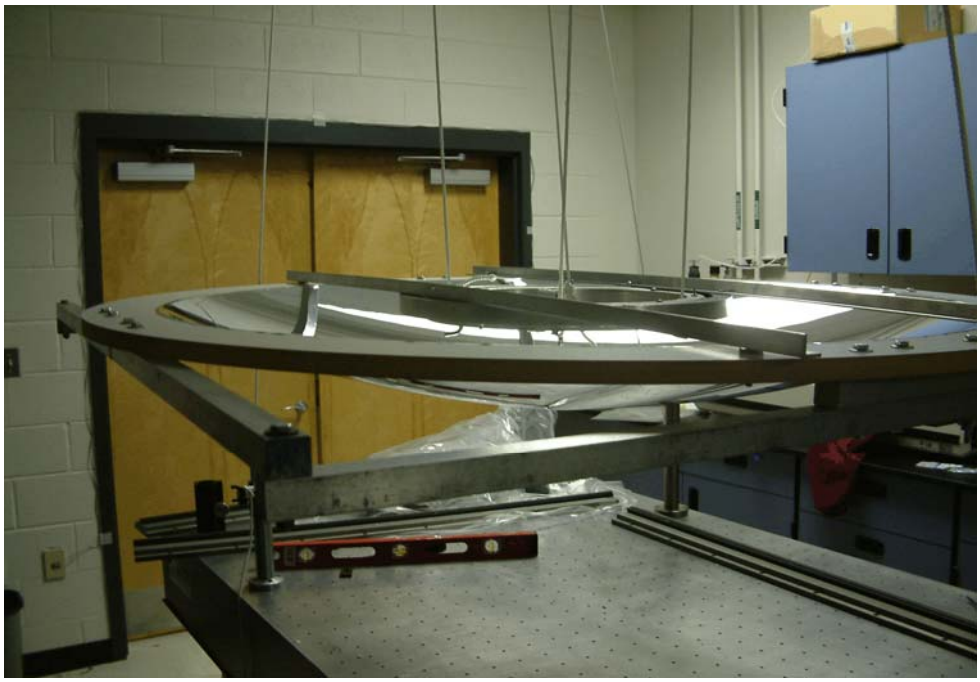

Figure 3.4 Suspension method #1 for the 1.0 m optic.

Figure 3.5 Suspension method #2 for the 1.0 m optic.

3.6 Data Collection

The initial method of collecting data included measuring the displacement of an incident parallel laser beam on an observation screen. This required an enormous amount of space because the reflected beam required a significant propagation distance. A new method was developed using a secondary mirror and it proved to be substantially better. This flat mirror was rotated until its reflected beam was coincident with the initial beam. This guaranteed the mirror to be normal to the reflected beam at that scan location. For all of the test pieces, the laser was aligned to the center of the optic and then translated in the x direction in 1.0 cm increments. The measurement mirror was then rotated to retro-reflect the beam back onto the optic and subsequently back to the laser aperture. This angle of rotation was then recorded. This constituted a single measurement. This

process was repeated until a complete scan along that profile of the optic was complete. The optic was then rotated about the optic axis 20 degrees and rescanned. Once all scans were made, the data was processed by the data reduction algorithm in Matlab. The results of the Matlab script were exported into Excel for creation of the plots seen later in this thesis.

CHAPTER 4

SURFACE MEASUREMENT RESULTS

4.1 Data, Data, and More Data

Representative raw data tables, surface profiles (ΔZ), and the departure from sphere (DFS) for each profile of each optic are presented in this section. Data was collected and processed for three 0.5 m optics and a single 1.0 m diameter optic. The results below show that all three optics fit a spherical profile very well. The departure from sphere is measured in units of centimeters. The scales of each of the curves should be particularly noticed since a departure from spherical of 0.5 cm would be considered excessive for normal optical elements, but is actually quite good for large aperture thin membrane optics. The best shape is obtained near the center of the optic and the largest deviation is observed near the support ring. This is perfectly acceptable since in most applications only the center portion of the optic is of interest. It is of particular interest to observe that the deviation from spherical is less for the large 1.0 m optic than for the 0.5 m optic. This has significant importance in planning the scaling of thin membrane mirrors to even larger diameters.

4.2 Optic #1 (0.5 m) Results

The data below represents one set of raw data obtained for optic #1, one of the 0.5 m diameter membranes. The raw data shows x_0 (scan location) and x_1 (reflected beam location) values measured for each scan profile. The following pages will list the raw data and provide two plots of reduced data. Each row in the table represents the scan location and the columns represent the reflected beam location for various rotations of the tested optic. The two plots that follow the table illustrate the surface profile (ΔZ) and the departure from sphere (DFS) for optic #1. The deviation seen at 16 cm for the 60 degree case is caused by the mounting structure. A small wrinkle in the optic at 60 degrees caused the reflected beam to deviate more than normal. The anomaly is more evident in the departure from sphere plot due to the scale difference.

Table 4.1 Raw Data from Optic #1 (0.5 m diameter)

x_0 (cm)	x_1 (cm)									
	0°	20°	40°	60°	80°	100°	120°	140°	160°	180°
-22	322.85	325.89	327.76	324.38	326.01	337.80	337.46	328.30	323.28	322.71
-21	290.25	292.69	294.41	291.58	293.01	301.60	300.31	297.58	289.36	292.99
-20	263.20	264.19	266.46	264.48	267.11	271.15	271.11	266.64	259.51	264.06
-19	239.55	241.14	242.08	240.43	241.21	245.40	245.51	240.23	245.90	237.65
-18	219.50	219.47	221.33	219.58	220.11	223.30	222.56	222.37	222.21	223.51
-17	199.45	200.52	201.93	200.63	200.36	203.30	202.66	204.79	199.27	201.75
-16	182.15	183.02	184.83	183.06	183.41	185.05	184.81	186.19	179.40	184.12
-15	166.55	166.82	167.63	167.16	167.46	168.45	167.71	165.53	163.50	165.13
-14	151.35	152.07	152.53	152.31	152.21	153.55	153.16	149.49	153.50	154.34
-13	137.55	138.52	139.23	139.01	139.16	139.70	138.46	136.89	140.57	138.82
-12	125.10	125.37	126.48	126.16	126.26	126.32	125.76	127.62	127.19	123.97
-11	113.20	113.75	114.33	113.46	113.46	113.97	113.16	112.45	115.79	114.00
-10	102.35	102.05	102.78	101.86	102.11	102.27	101.56	104.47	101.41	103.30
-9	90.48	90.50	91.53	91.01	90.46	90.87	90.11	90.71	91.60	91.31
-8	79.88	79.70	80.68	80.36	79.46	79.50	78.81	81.60	81.04	81.29
-7	69.18	69.55	69.78	69.51	69.46	68.50	68.06	69.69	68.48	68.90
-6	58.58	59.55	59.48	58.86	59.11	58.95	57.31	59.79	59.16	58.45
-5	48.83	48.95	49.18	48.71	48.16	48.30	47.71	49.71	49.12	48.99
-4	38.63	38.65	39.38	39.26	39.26	38.45	38.01	38.62	39.06	38.47
-3	28.53	28.90	29.53	29.46	29.26	29.00	28.01	29.83	28.67	28.79
-2	19.03	18.95	19.88	19.73	19.46	19.05	18.36	19.63	18.93	19.38
-1.5	14.39	14.15	14.88	14.88	14.46	14.40	13.61	14.71	13.97	14.50
-0.5	4.83	4.70	4.88	4.83	4.68	4.95	4.98	4.96	4.68	4.68
0	0.00	0.00	0.00	0.00	0.00	0.00	0.00	0.00	0.00	0.00
0.5	4.85	4.75	4.90	4.80	4.65	4.90	4.95	4.93	4.79	4.54
1	9.43	9.30	9.48	9.53	9.48	9.65	9.76	9.53	9.45	9.42
2	19.03	18.85	18.63	19.15	19.13	18.65	18.06	18.63	18.76	18.93
3	28.20	28.30	28.28	28.17	28.93	29.05	28.06	28.72	28.22	28.36
4	38.25	38.30	37.88	38.12	38.68	39.05	38.24	38.27	38.76	38.76
5	47.95	47.80	47.43	48.12	47.98	48.40	47.89	47.00	47.80	47.09
6	57.80	57.80	57.83	58.22	58.98	59.00	58.49	57.48	57.05	57.97
7	67.60	68.18	68.38	68.34	69.68	69.20	69.21	67.16	69.42	67.39
8	78.80	78.68	79.28	79.34	80.23	80.10	79.46	79.46	80.03	77.74
9	89.55	89.33	90.03	90.24	90.63	91.85	90.11	91.57	87.83	90.60
10	101.20	101.03	101.43	101.84	101.98	101.95	100.71	100.68	101.94	101.84
11	112.65	112.63	113.23	113.09	114.08	115.05	112.56	111.56	112.67	114.68
12	125.10	125.03	125.43	126.09	127.08	128.25	125.36	126.61	124.71	123.74
13	137.45	137.38	137.88	138.99	139.12	140.85	137.66	140.10	136.28	137.11
14	151.80	151.53	151.78	152.84	153.42	154.11	152.28	152.66	152.17	149.27
15	166.40	166.58	166.78	168.64	168.32	167.66	166.08	169.78	165.86	168.63
16	182.30	182.73	183.18	168.64	183.87	183.66	181.68	181.85	183.11	180.01
17	200.95	203.53	203.53	189.64	203.72	204.66	202.18	202.70	200.85	203.92
18	222.35	223.13	222.78	210.04	225.22	225.16	220.68	226.44	226.76	223.50
19	245.25	245.03	246.68	233.54	246.22	247.36	242.58	243.59	241.37	246.94
20	270.75	271.38	271.48	257.69	272.82	270.16	265.78	274.35	269.70	269.40
21	301.90	300.78	302.17	287.39	301.82	298.06	292.58	306.95	303.79	306.82
22	332.35	335.08	334.07	320.94	333.01	329.01	322.63	336.45	341.17	338.29

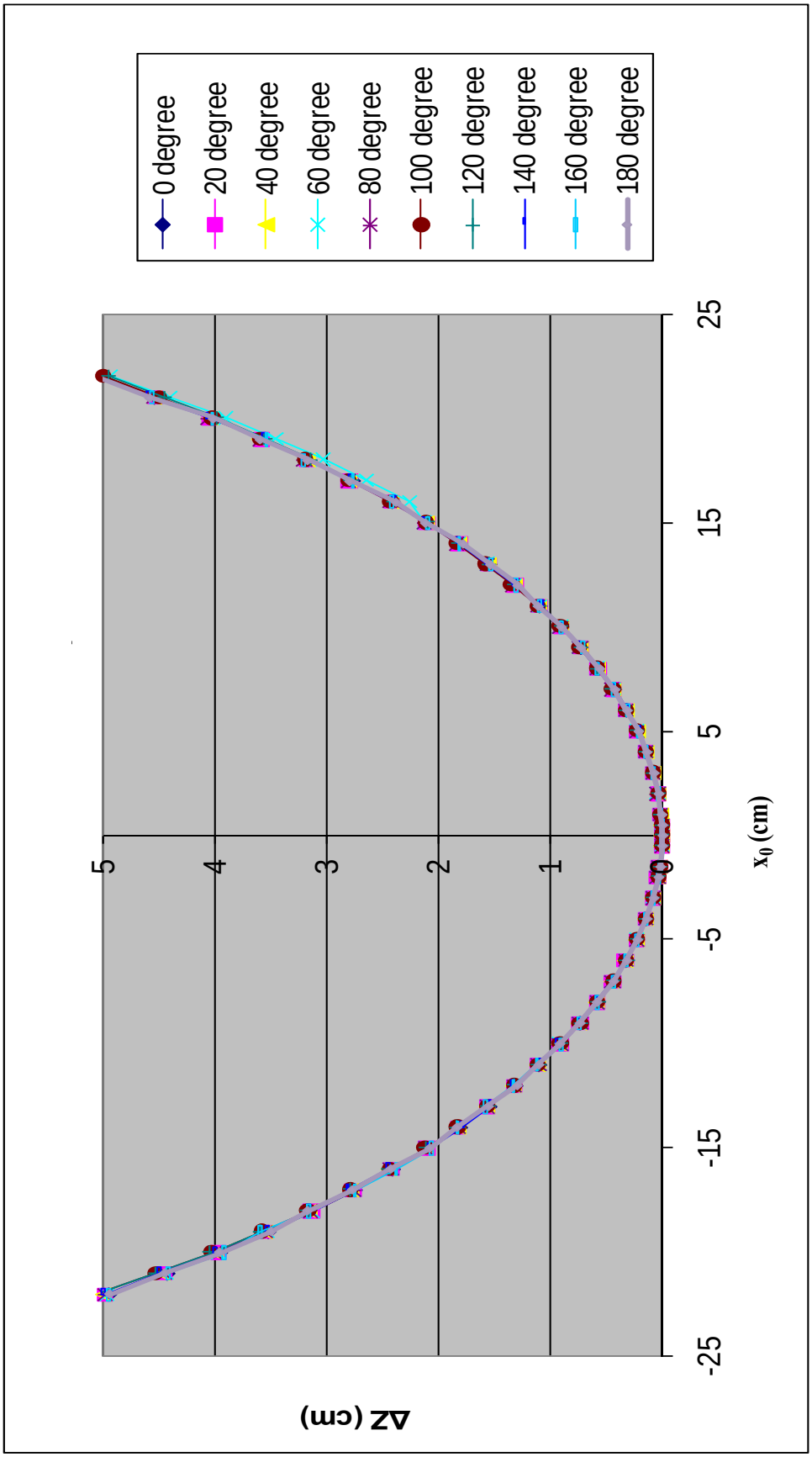

Figure 4.1 Optic #1 Surface Profile,
Notice the small deviation on the 60 degree scan.

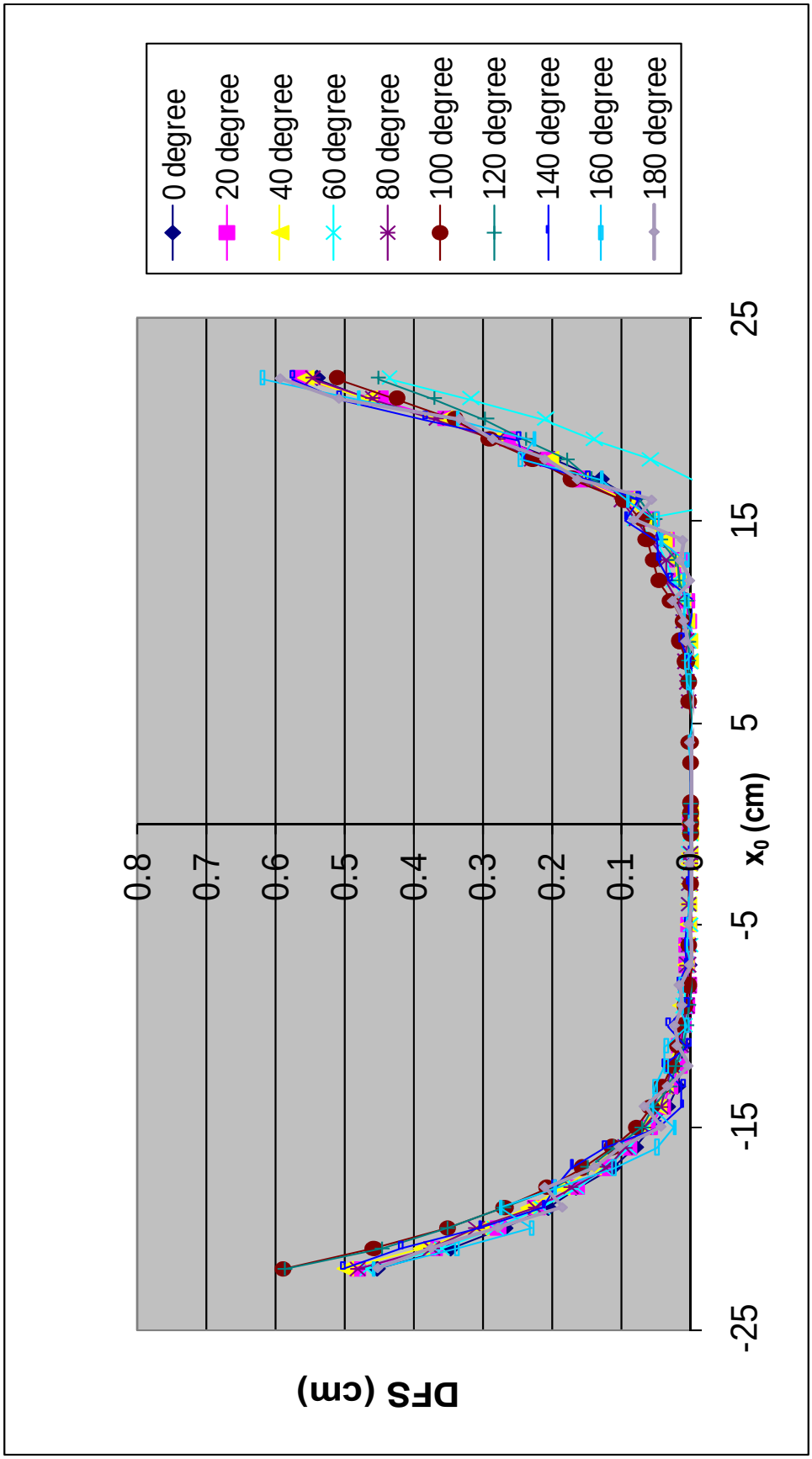

Figure 4.2 Optic #1 (0.5 m diameter) Departure From Sphere.

4.3 Optic #2 (0.5 m) Results

The data below represents one set of raw data obtained for optic #2, one of the 0.5 m diameter membranes. The raw data shows x_0 (scan location) and x_1 (reflected beam location) values measured for each scan profile. The following pages will list the raw data and provide two plots of reduced data. Each row in the table represents the scan location and the columns represent the reflected beam location for various rotations of the tested optic. The two plots that follow the table illustrate the surface profile (ΔZ) and the departure from sphere (DFS) for optic #2. There is no irregular deviation in this data as seen with the first optic; this is evident from the surface profile figure where each curve is nearly identical. The departure from sphere plot has more separation between each curve but the scale is significantly smaller thus magnifying small differences.

Table 4.2. Raw Data for Optic #2 (0.5 m diameter)

x_0 (cm)	x_1 (cm)									
	0°	20°	40°	60°	80°	100°	120°	140°	160°	180°
-21	334.90	351.70	350.68	364.04	366.60	354.70	361.41	352.95	353.63	334.08
-20	300.95	315.45	313.40	323.42	327.05	315.80	325.66	316.83	314.32	296.21
-19	271.95	284.15	281.20	289.57	292.45	283.65	290.73	276.04	288.12	271.19
-18	246.30	256.61	252.60	259.72	262.85	255.75	261.18	255.68	256.03	243.45
-17	223.30	232.27	227.76	233.94	237.05	230.55	236.19	226.71	232.19	223.13
-16	202.70	211.27	206.46	211.59	213.65	208.80	211.61	210.15	211.93	200.51
-15	184.40	192.47	186.90	191.67	193.27	189.30	193.26	183.49	191.24	184.22
-14	167.10	175.07	169.19	173.30	174.27	171.60	171.29	171.85	172.33	165.17
-13	151.85	158.55	152.79	156.45	156.97	154.15	155.10	154.54	161.63	151.33
-12	136.70	143.15	137.83	140.75	141.27	138.25	139.85	140.06	141.23	134.40
-11	123.25	129.02	122.98	126.10	126.13	124.20	125.40	121.06	127.11	122.13
-10	109.50	115.37	109.45	112.25	112.77	110.20	112.30	108.11	113.10	108.26
-9	97.95	102.47	96.70	98.95	99.75	97.05	99.17	96.61	103.32	97.80
-8	86.10	90.52	84.45	86.65	86.70	85.75	85.80	83.61	89.31	85.09
-7	73.95	78.99	72.65	74.80	74.67	74.10	73.38	73.48	78.14	73.75
-6	63.15	67.59	61.55	63.40	62.93	62.65	62.53	62.39	66.98	62.55
-5	52.25	57.02	50.82	52.00	51.63	51.90	50.77	50.01	57.06	51.69
-4	41.80	46.17	39.62	41.00	41.28	41.00	40.46	39.37	45.44	41.38
-3	31.80	35.79	29.37	30.80	30.58	30.20	30.07	29.01	36.09	31.33
-2	21.20	25.75	19.47	20.75	20.08	20.10	19.74	19.82	25.81	20.92
-1	10.70	10.25	9.05	10.38	10.04	9.95	9.90	9.00	10.41	10.56
0	0.00	0.00	0.00	0.00	0.00	0.00	0.00	0.00	0.00	0.00
1	9.95	10.20	11.20	10.10	10.20	10.70	10.07	11.13	10.29	9.84
2	20.10	25.42	21.30	20.12	20.70	21.20	20.66	20.94	25.92	19.99
3	30.20	35.34	31.67	30.74	31.20	31.80	31.08	31.74	35.53	29.72
4	41.00	45.59	42.22	40.99	41.30	41.80	40.97	42.18	46.13	40.45
5	51.90	56.29	53.02	51.69	51.75	52.25	50.92	53.54	57.12	51.69
6	62.65	68.04	63.97	62.57	62.61	63.15	61.47	63.73	69.39	61.40
7	74.10	79.04	74.82	73.17	73.46	73.95	72.11	74.56	78.03	73.15
8	85.75	90.63	85.97	84.92	84.02	86.10	82.71	87.66	90.61	84.96
9	97.05	101.63	97.07	96.22	94.87	97.95	94.54	97.46	100.67	96.05
10	110.20	113.73	109.52	108.12	107.13	109.50	105.23	110.09	114.24	109.93
11	124.20	127.36	122.12	120.42	119.80	123.25	118.57	122.35	126.67	122.30
12	138.25	141.11	136.42	133.62	133.65	136.70	133.46	137.21	142.26	137.39
13	154.15	155.41	150.72	147.62	148.15	151.85	145.25	148.67	154.08	153.44
14	171.60	173.23	167.32	164.22	164.10	167.10	162.82	168.58	171.81	170.35
15	189.30	190.58	185.13	180.62	180.20	184.40	178.60	184.95	190.12	187.63
16	208.80	209.43	204.81	198.97	197.93	202.70	197.37	206.43	213.24	205.51
17	230.55	230.75	225.40	218.27	216.55	223.30	213.28	227.21	231.48	229.15
18	255.75	254.15	248.00	239.40	238.65	246.30	234.66	245.65	254.01	252.24
19	283.65	282.05	274.66	263.40	262.48	271.95	262.19	276.35	286.85	278.50
20	315.80	313.95	305.42	291.10	289.88	300.95	288.91	301.42	315.86	312.41
21	354.70	350.60	342.80	322.85	321.48	334.90	315.79	337.98	353.91	350.81
20	270.75	271.38	271.48	257.69	272.82	270.16	269.06	271.16	266.50	268.49
21	301.90	300.78	302.17	287.39	301.82	298.06	299.21	296.67	306.39	298.61

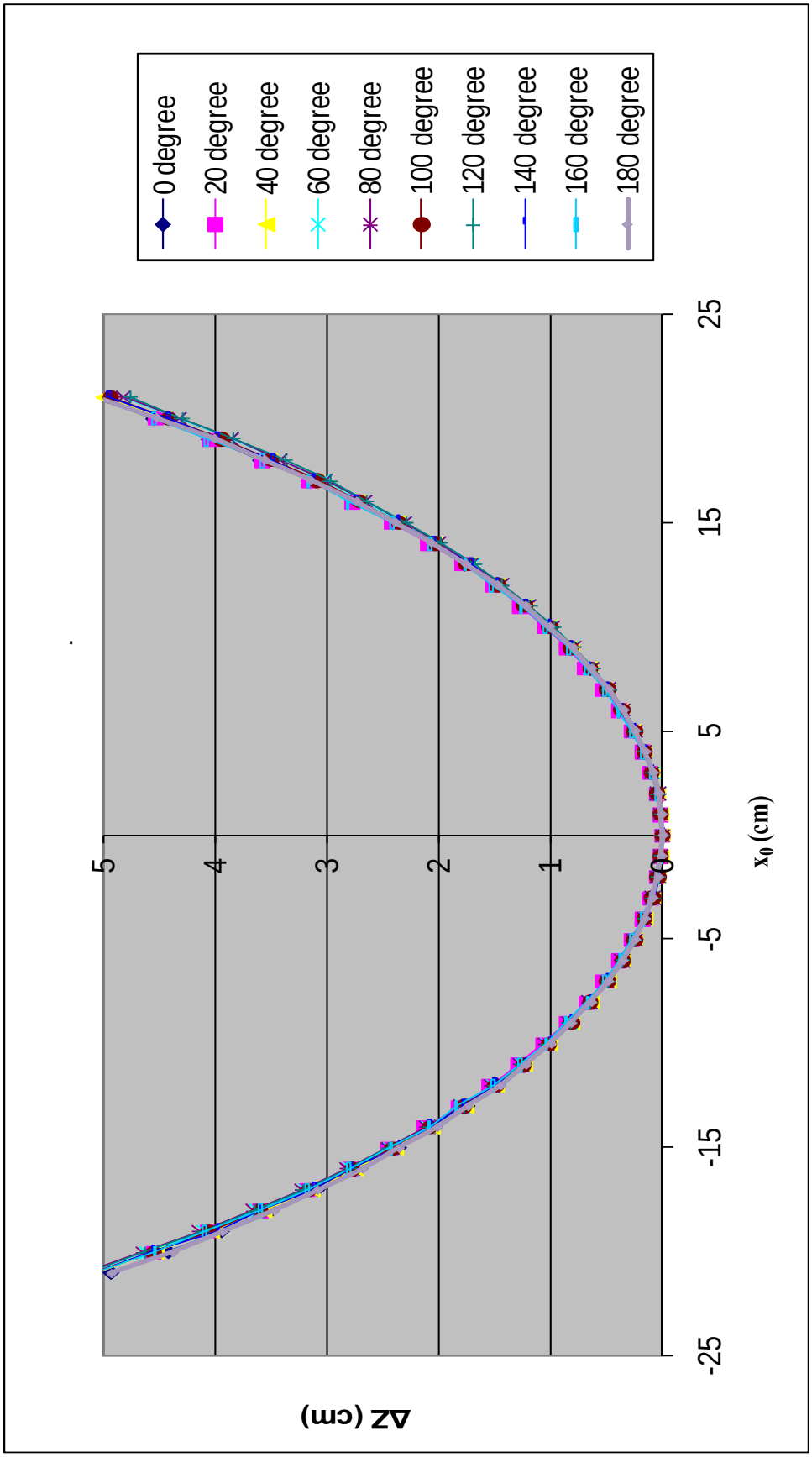

Figure 4.3 Optic #2 Surface Profile.

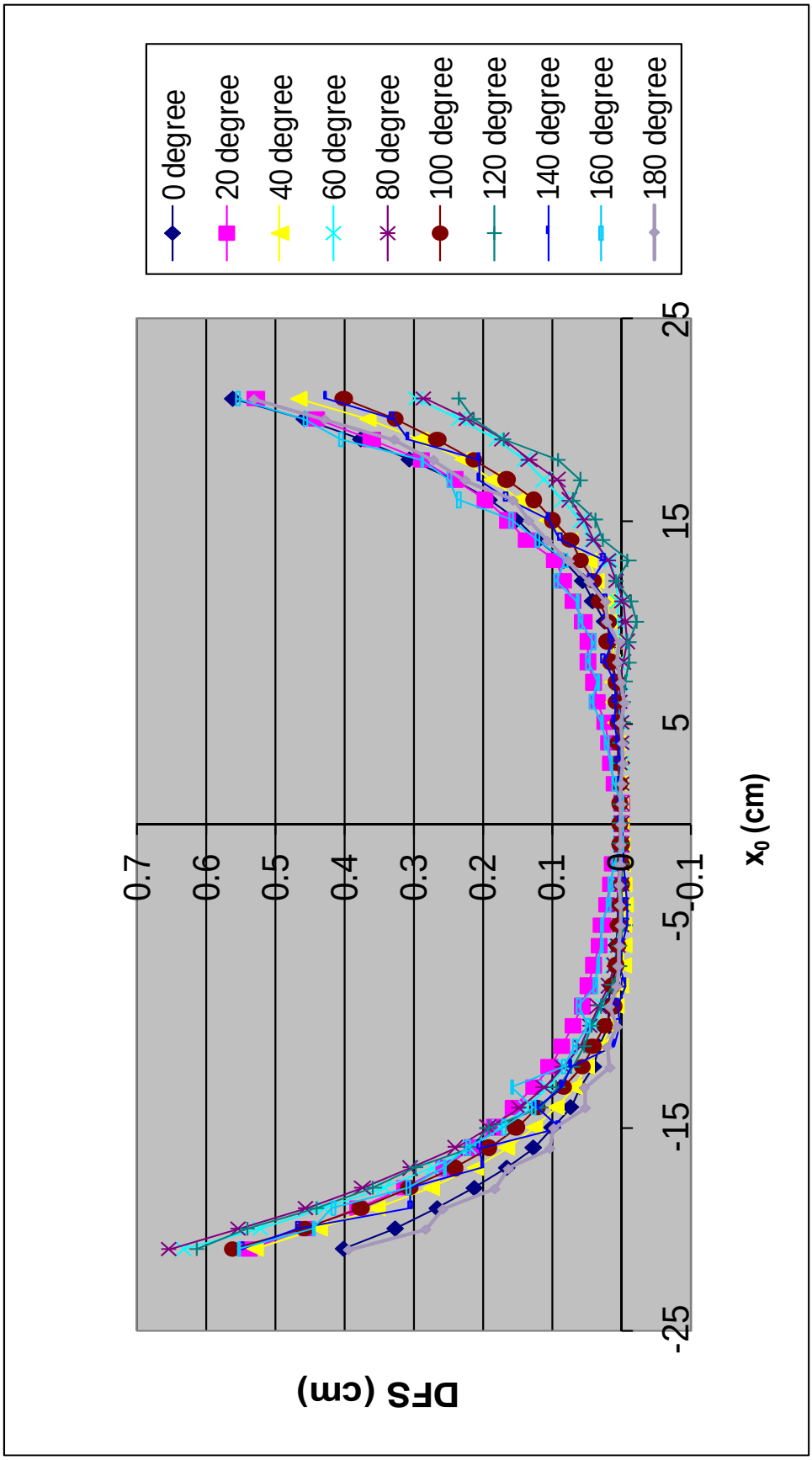

Figure 4.4 Optic #2 Departure From Sphere.

4.4 Optic #3 (0.5 m) Results

The data below represents one set of raw data obtained for optic #3, the final sample of 0.5 m diameter membranes. The raw data shows x_0 (scan location) and x_1 (reflected beam location) values measured for each scan profile. The following pages will list the raw data and provide two plots of reduced data. Each row in the table represents the scan location and the columns represent the reflected beam location for various rotations of the tested optic. The two plots that follow the table illustrate the surface profile (ΔZ) and the departure from sphere (DFS) for optic #3. There is no irregular deviation in this data as seen with the first optic. The surface profile plot for optic #3 resembles the surface profile for optic #2 with each curve agreeing very well. However, the departure from sphere produced an odd shaped DFS profile and each curve has this same profile. The calculation for DFS was examined but nothing was found to produce this profile.

Table 4.3 Raw Data for Optic #3.

x_0 (cm)	x_1 (cm)									
	0°	20°	40°	60°	80°	100°	120°	140°	160°	180°
-22	331.07	331.77	324.98	316.69	318.63	317.50	314.28	318.81	330.22	329.80
-21	298.42	297.72	291.58	283.53	286.53	285.45	284.13	291.26	297.64	297.00
-20	269.32	268.52	263.83	255.97	259.73	259.17	256.63	263.58	266.96	268.68
-19	242.92	242.64	238.73	232.57	235.18	235.63	234.10	235.67	242.32	240.02
-18	220.97	222.01	217.13	210.82	214.38	213.53	213.70	216.00	221.03	219.76
-17	202.02	202.16	197.25	192.82	195.83	195.01	195.62	196.86	200.33	199.27
-16	183.62	184.44	180.00	176.02	177.88	178.33	178.87	177.41	182.50	183.56
-15	167.52	167.74	164.46	160.67	161.83	163.03	163.22	161.93	166.44	166.56
-14	152.40	152.14	149.38	146.22	147.23	147.93	148.72	147.17	149.74	152.35
-13	138.30	138.28	136.38	133.07	134.21	134.13	133.85	135.77	136.34	136.72
-12	125.70	126.18	124.00	120.55	121.66	121.73	121.31	123.63	124.63	124.23
-11	113.06	112.80	111.28	108.90	109.96	109.88	109.46	110.57	112.12	111.12
-10	101.46	101.16	98.83	97.10	98.16	97.93	97.96	98.12	100.10	101.16
-9	90.86	89.76	88.03	86.20	86.86	87.03	87.43	86.61	89.67	89.72
-8	79.83	78.56	77.83	75.85	76.21	76.38	77.13	76.90	77.56	78.68
-7	68.43	68.81	67.38	65.77	66.46	66.18	67.27	67.07	67.73	68.11
-6	58.88	59.11	57.10	55.55	56.41	56.08	57.27	55.97	58.84	57.97
-5	48.53	48.36	47.38	46.10	46.26	46.03	47.15	46.71	48.14	47.68
-4	38.58	38.63	36.88	36.62	36.46	36.43	37.85	36.80	38.19	38.11
-3	29.48	29.03	27.98	26.62	27.32	27.25	29.48	27.83	28.83	29.17
-2	19.48	19.58	18.88	17.40	17.80	17.90	19.48	18.59	19.41	19.45
-0.5	4.75	5.05	4.48	8.20	9.10	8.90	4.75	4.44	5.05	4.74
0	0.00	0.00	0.00	0.00	0.00	0.00	0.00	0.00	0.00	0.00
1	9.85	9.20	9.40	10.25	10.00	10.25	9.85	9.30	9.12	9.70
2.5	23.35	22.68	22.85	19.30	19.48	19.70	23.35	22.55	22.62	22.88
3	27.95	27.28	27.55	28.45	28.58	29.22	27.95	27.36	26.91	27.89
4	37.85	36.72	37.15	38.00	37.90	38.52	38.58	36.98	36.52	37.80
5	47.15	47.04	46.40	48.35	47.50	48.12	48.53	46.30	46.25	46.34
6	57.27	56.59	57.05	58.85	57.50	58.07	58.88	57.04	55.98	56.59
7	67.27	66.59	66.30	67.90	67.80	68.22	68.43	65.82	66.27	66.70
8	77.13	76.84	76.60	78.42	77.47	79.37	79.83	76.46	76.83	76.19
9	87.43	86.84	87.20	88.32	87.87	88.99	90.86	87.01	86.68	87.21
10	97.96	97.82	98.25	99.47	99.37	100.49	101.46	98.13	97.63	96.63
11	109.46	109.87	109.60	110.42	110.22	112.09	113.06	108.51	109.56	107.99
12	121.31	121.57	122.80	122.67	122.47	123.89	125.70	121.57	120.85	120.70
13	133.85	133.97	136.00	136.37	137.97	137.14	138.30	135.56	132.25	132.20
14	148.72	149.07	150.00	151.00	152.17	153.44	152.40	148.02	148.82	147.53
15	163.22	163.74	164.97	166.62	167.12	168.74	167.52	164.60	163.14	161.52
16	178.87	178.59	181.52	183.14	183.37	184.24	183.62	179.63	175.37	177.01
17	195.62	196.68	200.97	201.84	201.30	201.69	202.02	200.86	193.58	191.71
18	213.70	215.18	222.75	222.24	221.80	221.54	220.97	221.38	212.90	209.50
19	234.10	236.58	246.05	245.29	244.90	244.10	242.92	241.93	236.46	233.64
20	256.63	260.71	270.65	271.04	271.50	270.68	269.32	267.67	258.89	252.16
21	284.13	289.21	300.50	301.14	301.62	301.53	298.42	296.03	284.46	278.48
22	314.28	321.71	339.25	333.84	336.59	337.88	331.07	334.88	317.48	308.85

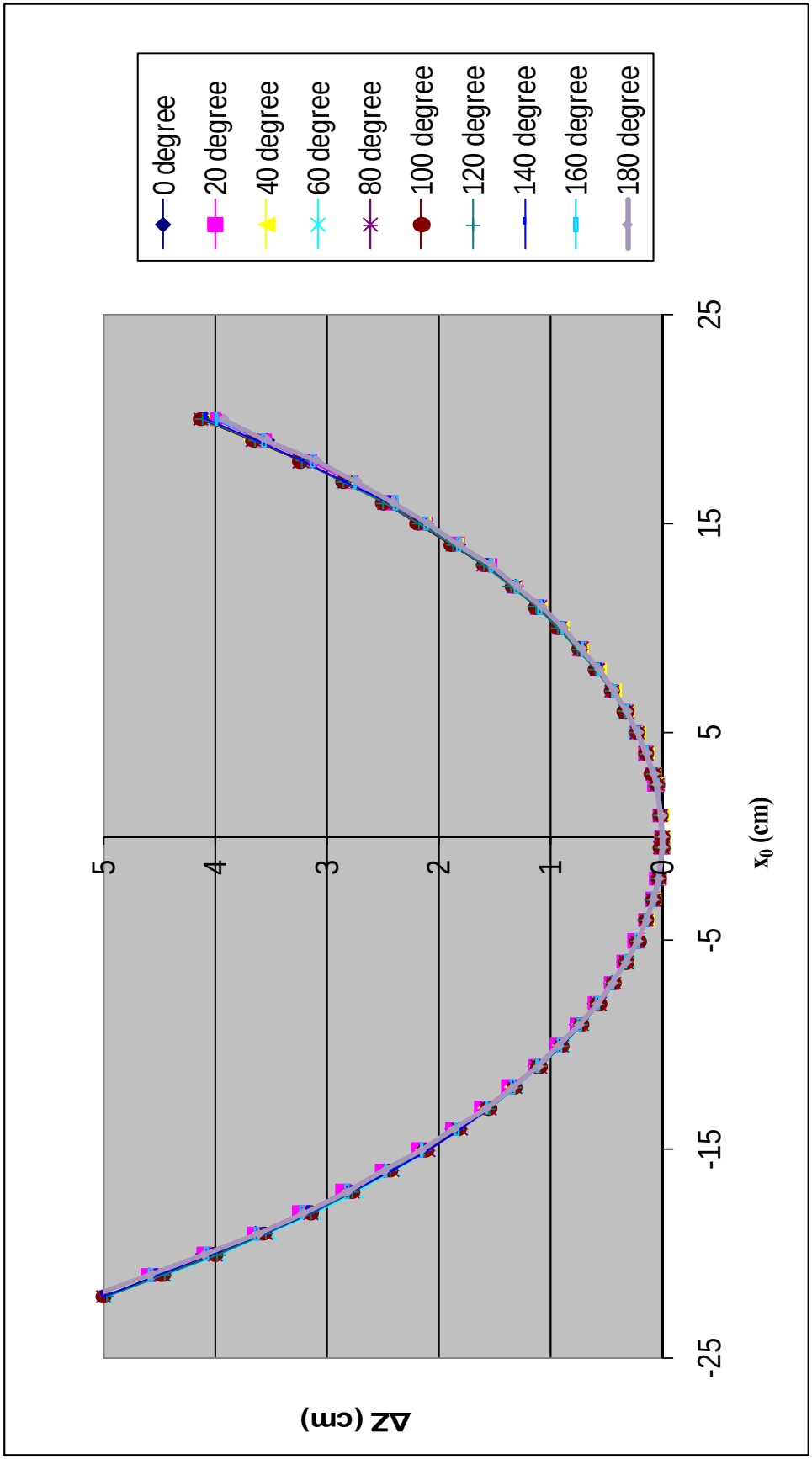

Figure 4.5 Optic #3 Surface Displacement.

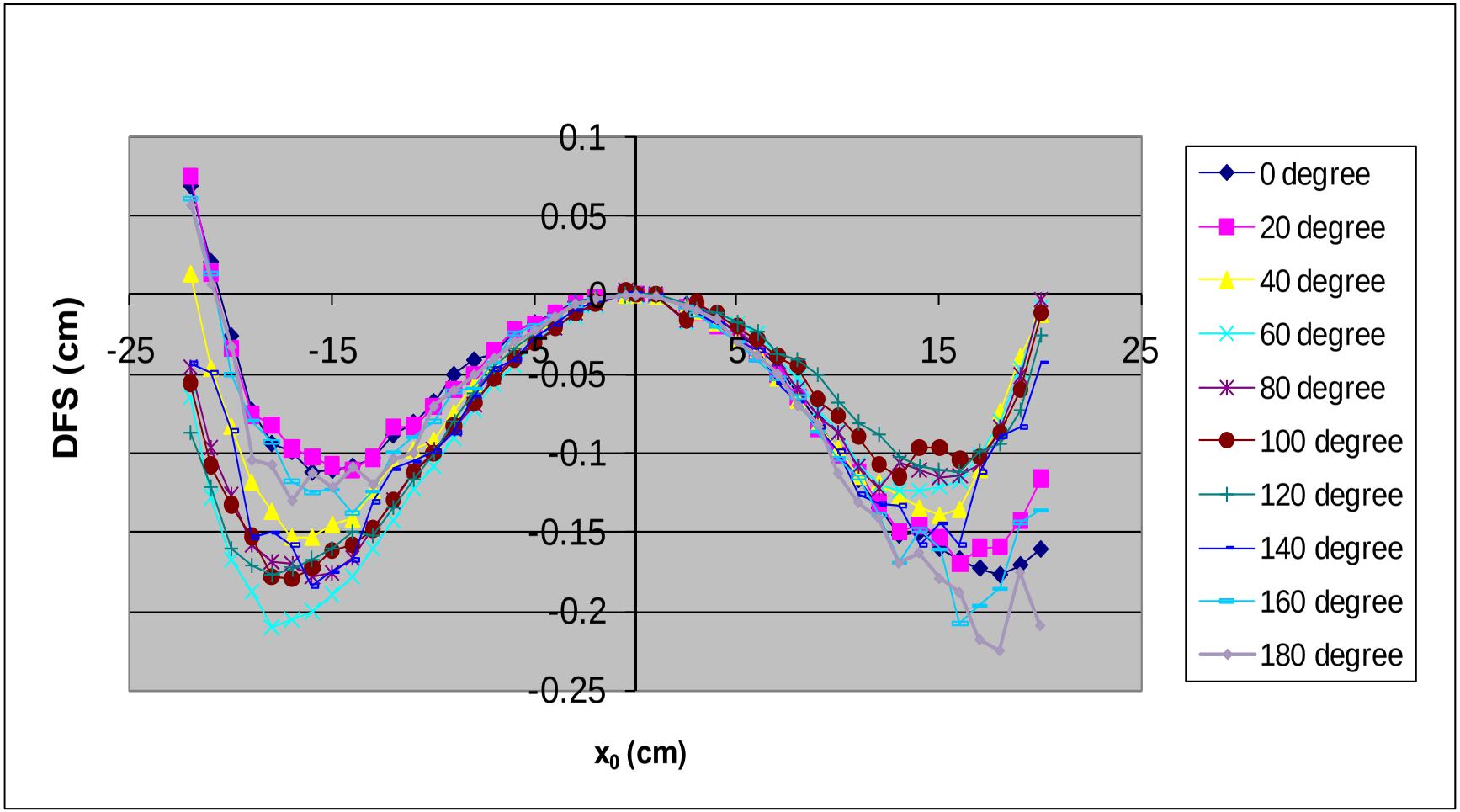

Figure 4.6 Optic #3 Departure From Sphere.

4.5 Optic #4 (1.0 m) Results

The data below represents one set of raw data obtained for optic #4, the 1.0 m diameter membrane. The raw data shows x_0 (scan location) and θ (reflected beam angle) values measured for each scan profile. The following pages will list the raw data and provide two plots of reduced data. Each row in the table represents the scan location and the columns represent the reflected beam location for various rotations of the tested optic. The two plots that follow the table illustrate the surface profile (ΔZ) and the departure from sphere (DFS) for optic #4. There is no irregular deviation in this data as seen with the first optic. The surface profile for all scans line up very well relative to each other. The DFS plot shows very little departure sphere for the majority of the aperture of the optic. The data becomes more erratic towards to the edge of the aperture yet the maximum departure from sphere is only 0.4 cm over a 68 cm aperture.

Table 4.4. Raw Data for Optic #4 (1.0 m) showing direct measurement of θ

x_0 (cm)	2θ (deg)								
	0°	20°	40°	60°	80°	100°	120°	140°	160°
-34	-36.1	-35.5	-35	-35	-35	-36	-36.5	-34.5	-36.3
-32	-34.5	-33.5	-33	-33	-33	-34	-34.5	-32.3	-34
-30	-32	-31	-31	-30.5	-30.5	-32	-32	-30.1	-32
-28	-30	-29.5	-29	-28.2	-28.5	-30	-29	-28	-30
-26	-27.5	-27	-26.5	-26.1	-26.5	-26.5	-27	-26	-28
-24	-25.6	-25	-24.5	-24.1	-24	-24.3	-25	-23.5	-25.7
-22	-23.2	-23	-22.5	-22	-22.1	-22.3	-22.5	-22	-23.9
-20	-21	-20.2	-20.5	-20	-20	-20	-20	-19.5	-21
-18	-19	-18.3	-18	-18	-18	-18	-18	-17.75	-18.3
-16	-16.5	-16.5	-16	-15.9	-16	-16	-16.5	-15.75	-16.3
-14	-14.2	-14.5	-14	-14	-13.5	-14	-14	-14	-14.3
-12	-13	-12	-12	-12.1	-12	-12	-12	-12	-13
-10	-10.5	-10	-10	-10	-9.5	-10	-10.1	-10	-10.1
-8	-8.2	-8	-8	-8	-8	-7.5	-8	-7.5	-8
-6	-7	-6	-6	-6	-6	-6	-6	-6	-6
-4	-4.4	-4	-4.5	-4	-4	-4	-5	-4	-5
-2	-2	-2.5	-2.5	-2	-2	-2	-2.5	-2.5	-2.3
0	0	0	0	0	0	0	0	0	0
2	1.9	1.8	2	1.5	1.9	1.7	1.5	2	2
4	3.9	3.9	3.5	3.9	3.9	3.6	3	3.9	3.5
6	6	6	6	5.9	5.9	5.7	5	6	6
8	7.9	7.9	8	7	7.5	7.7	7	7	7.7
10	9.9	10	10	9.9	9	9.8	9	9.5	9.7
12	11.9	11.9	11.75	11.5	11	11	10.5	11.5	11.7
14	13.9	14	14	13	13	13	12.5	13	13.3
16	16	16	16	15.9	15.5	14.7	14.8	15.5	15
18	18.1	18.5	18	17.8	17.5	17	17	17.5	18
20	20.5	21	20.5	20	20	19.8	18.8	20	20
22	23	23	23	22	22	22	21	22	22
24	25	25	25	24.2	24	24	23.5	24.5	24
26	27	27	27	26.5	26.5	26	26	27	26.3
28	29.5	29.5	29.5	29	28.5	28	28	29	28.5
30	32	32	32	31	31	30.5	30	31	30.3
32	34	33.9	34.5	33.5	33.5	33.7	32.5	33.5	33.7
34	36	36.5	37	36.5	36.5	35.9	35.5	36	36

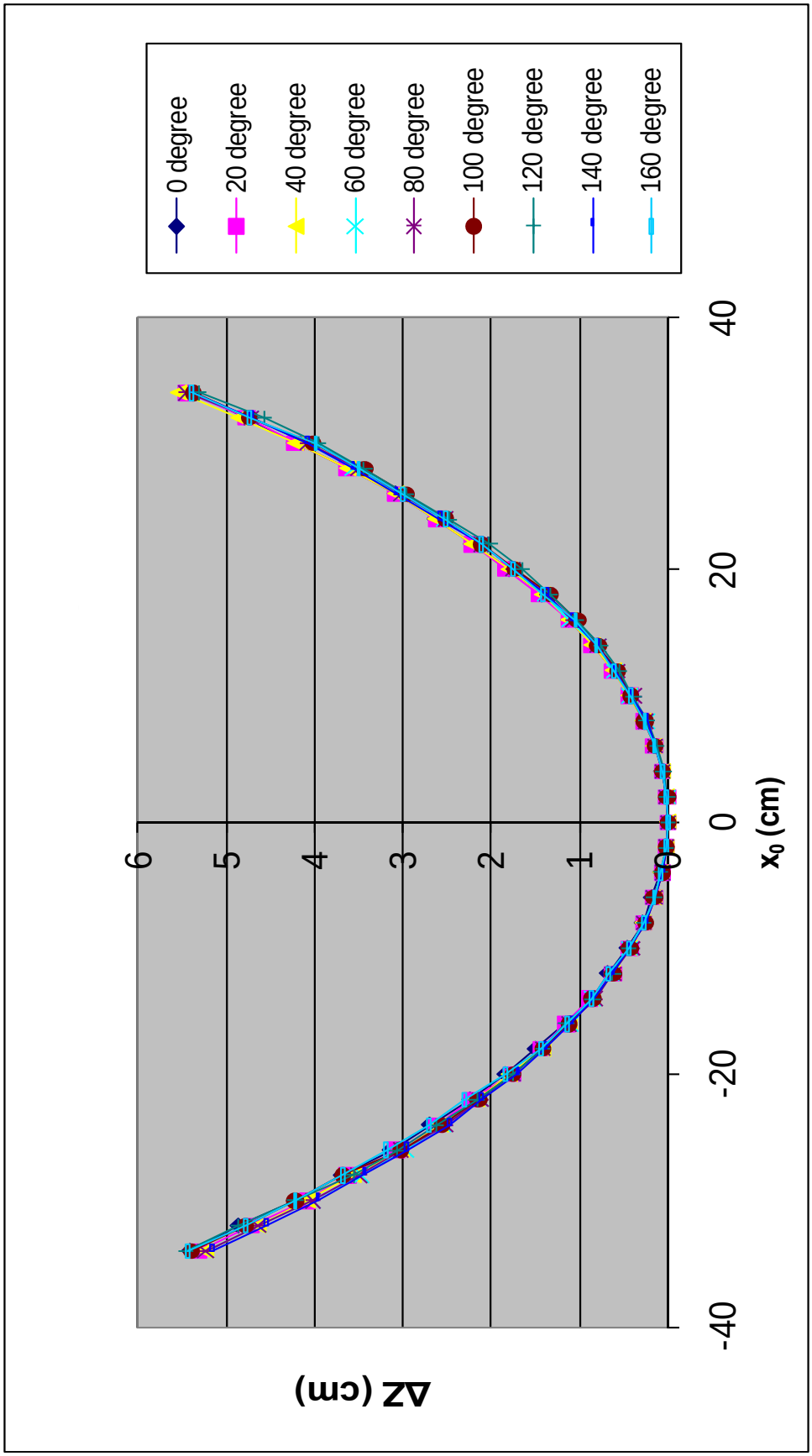

Figure 4.7 Surface Profile for Optic #4.

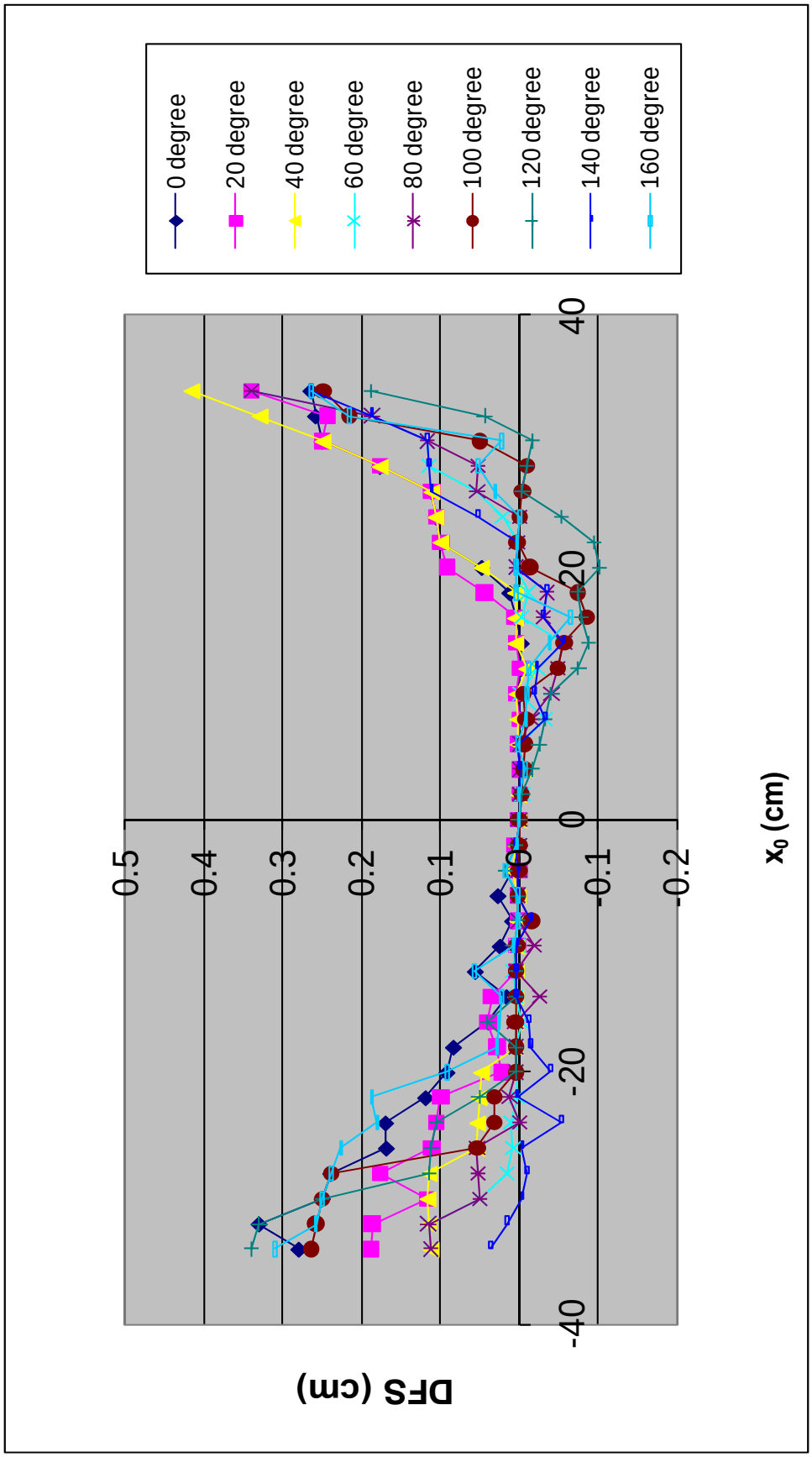

Figure 4.8 Departure From Sphere for Optic #4.

4.6 Measurement Method on Known Surface

How accurate is this method of measuring the surface of an optic? The validity of the measurement techniques presented needed to be tested. This was accomplished by scanning a 16 cm diameter rigid optic using the mirror method technique in this thesis and then comparing the results with the radius of curvature measured with a spherometer by an independent source. A spherometer is a contact measuring device used for determining the radius of curvature of a surface. The device consists of three balls oriented in circle that make contact with the surface under test and plunger, typically a micrometer, in the center of the circle. The balls define the measurement plane and the plunger measures the amount of sag from the measurement plane. Knowing the radius of the balls and the diameter of the circle, the radius of curvature can be calculated using the reading from the micrometer. The rigid optic was a solid glass optic in which the radius of curvature was unknown at the time of the measurements. This "control sphere" was measured by Dr. Joseph Geary and Mr. Ted Rogers of the Center for Applied Optics using a spherometer in the optical testing laboratory. The measurement of the curvature was made using two separate ring diameters, 3 cm and 9 cm. This allows measurement of the curvature at different parts of the lens to determine if the optic is spherical or aspherical. The average of the two measurements is 29.474 cm and the difference in the two measurements was 180 um, or approximately 0.06%. This small deviation in the two measurements shows that the surface can be treated as a sphere. Table 4.5 shows the calculated radius of curvature using the surface scan method for each scan location and the percent difference from the calculated radius from the spherometer.

Table 4.5 Comparison of surface scan to spherometer measurements for control sphere

X_0 (cm)	Surface Scan Radius of Curvature (cm)	% error
-8.8	29.98	1.71
-8.3	29.98	1.73
-7.8	30.06	1.98
-7.3	30.37	3.03
-6.8	30.56	3.70
-6.3	30.79	4.48
-5.8	30.88	4.78
-5.3	30.64	3.97
-4.8	30.33	2.91
-4.3	30.61	3.86
-3.8	30.66	4.02
-3.3	30.93	4.93
-2.8	30.72	4.22
-2.3	31.40	6.55
-1.8	31.90	8.22
-1.3	32.25	9.43
-0.8	35.95	21.98
-0.3	51.31	74.09
0	NAN	NAN
0.15	17.36	41.09
0.2	19.10	35.20
0.7	24.76	15.99
1.2	27.46	6.85
1.7	28.83	2.17
2.2	28.23	4.23
2.7	28.53	3.19
3.2	28.64	2.83
3.7	28.75	2.47
4.2	28.84	2.16
4.7	28.79	2.31
5.2	29.18	1.00
5.7	29.19	0.96
6.2	29.21	0.90
6.7	29.29	0.64
7.2	29.19	0.96
7.7	29.27	0.68
8.2	29.29	0.64
8.7	29.31	0.57
9.2	29.37	0.35

4.7 Comparison of Results

The average departure from sphere for each scan location and each optic were calculated and compared. The raw comparison and percentage of nominal radius is shown in Table 4.6 and Figure 4.9 illustrates the raw data comparison. The radius of curvature listed is that of the reference sphere. All measurements are in centimeters.

Table 4.6 Comparison of average DFS for each optic

Optic #1				Optic #2				Optic #3				Optic #4		
radius		56.167		radius		52.833		radius		50.518		radius		115.419
x0	DFS	% err		x0	DFS	% err		x0	DFS	% err		x0	DFS	% err
-22	0.496	0.88%												
-21	0.387	0.69%						-22	-0.002	0.00%				
-20	0.295	0.53%		-21	0.542	1.03%		-21	-0.050	0.10%				
-19	0.231	0.41%		-20	0.448	0.85%		-20	-0.090	0.18%				
-18	0.186	0.33%		-19	0.368	0.70%		-19	-0.127	0.25%				
-17	0.135	0.24%		-18	0.298	0.56%		-18	-0.140	0.28%				
-16	0.096	0.17%		-17	0.236	0.45%		-17	-0.148	0.29%		-34	0.194	0.17%
-15	0.058	0.10%		-16	0.191	0.36%		-16	-0.151	0.30%		-32	0.191	0.17%
-14	0.045	0.08%		-15	0.148	0.28%		-15	-0.147	0.29%		-30	0.147	0.13%
-13	0.032	0.06%		-14	0.114	0.22%		-14	-0.143	0.28%		-28	0.131	0.11%
-12	0.023	0.04%		-13	0.094	0.18%		-13	-0.131	0.26%		-26	0.086	0.07%
-11	0.016	0.03%		-12	0.066	0.12%		-12	-0.113	0.22%		-24	0.067	0.06%
-10	0.014	0.03%		-11	0.046	0.09%		-11	-0.102	0.20%		-22	0.061	0.05%
-9	0.008	0.01%		-10	0.031	0.06%		-10	-0.089	0.18%		-20	0.025	0.02%
-8	0.007	0.01%		-9	0.027	0.05%		-9	-0.073	0.15%		-18	0.016	0.01%
-7	0.002	0.00%		-8	0.016	0.03%		-8	-0.060	0.12%		-16	0.016	0.01%
-6	0.002	0.00%		-7	0.012	0.02%		-7	-0.045	0.09%		-14	0.007	0.01%
-5	0.001	0.00%		-6	0.008	0.02%		-6	-0.033	0.07%		-12	0.016	0.01%
-4	0.000	0.00%		-5	0.005	0.01%		-5	-0.025	0.05%		-10	0.004	0.00%
-3	0.000	0.00%		-4	0.003	0.01%		-4	-0.016	0.03%		-8	-0.001	0.00%
-2	0.000	0.00%		-3	0.003	0.01%		-3	-0.008	0.02%		-6	0.004	0.00%
-1.5	0.000	0.00%		-2	0.002	0.00%		-2	-0.004	0.01%		-4	0.006	0.01%
-0.5	0.000	0.00%		-1	0.000	0.00%		-0.5	0.000	0.00%		-2	0.002	0.00%
0	0.000	0.00%		0	0.000	0.00%		0	0.000	0.00%		0	0.000	0.00%
0.5	0.000	0.00%		1	0.000	0.00%		1	-0.001	0.00%		2	-0.002	0.00%
1	0.000	0.00%		2	0.003	0.01%		2.5	-0.010	0.02%		4	-0.005	0.00%
2	-0.001	0.00%		3	0.004	0.01%		3	-0.010	0.02%		6	-0.003	0.00%
3	-0.002	0.00%		4	0.005	0.01%		4	-0.016	0.03%		8	-0.015	0.01%
4	-0.001	0.00%		5	0.008	0.01%		5	-0.025	0.05%		10	-0.013	0.01%
5	-0.004	0.01%		6	0.010	0.02%		6	-0.033	0.07%		12	-0.027	0.02%
6	-0.004	0.01%		7	0.010	0.02%		7	-0.047	0.09%		14	-0.039	0.03%
7	-0.003	0.00%		8	0.016	0.03%		8	-0.060	0.12%		16	-0.031	0.03%
8	0.000	0.00%		9	0.013	0.02%		9	-0.077	0.15%		18	-0.018	0.02%
9	0.002	0.00%		10	0.019	0.04%		10	-0.093	0.18%		20	0.010	0.01%

Table 4.6 (continued)

x0	DFS	% err		x0	DFS	% err		x0	DFS	% err		x0	DFS	% err
10	0.006	0.01%		11	0.026	0.05%		11	-0.110	0.22%		22	0.024	0.02%
11	0.011	0.02%		12	0.042	0.08%		12	-0.124	0.24%		24	0.037	0.03%
12	0.020	0.04%		13	0.049	0.09%		13	-0.135	0.27%		26	0.063	0.05%
13	0.027	0.05%		14	0.083	0.16%		14	-0.134	0.27%		28	0.094	0.08%
14	0.042	0.08%		15	0.107	0.20%		15	-0.138	0.27%		30	0.128	0.11%
15	0.068	0.12%		16	0.145	0.27%		16	-0.148	0.29%		32	0.207	0.18%
16	0.067	0.12%		17	0.177	0.34%		17	-0.138	0.27%		34	0.296	0.26%
17	0.136	0.24%		18	0.216	0.41%		18	-0.126	0.25%				
18	0.199	0.35%		19	0.285	0.54%		19	-0.099	0.20%				
19	0.252	0.45%		20	0.348	0.66%		20	-0.073	0.14%				
20	0.332	0.59%		21	0.428	0.81%		21	-0.028	0.06%				
21	0.444	0.79%						22	0.035	0.07%				
22	0.538	0.96%												

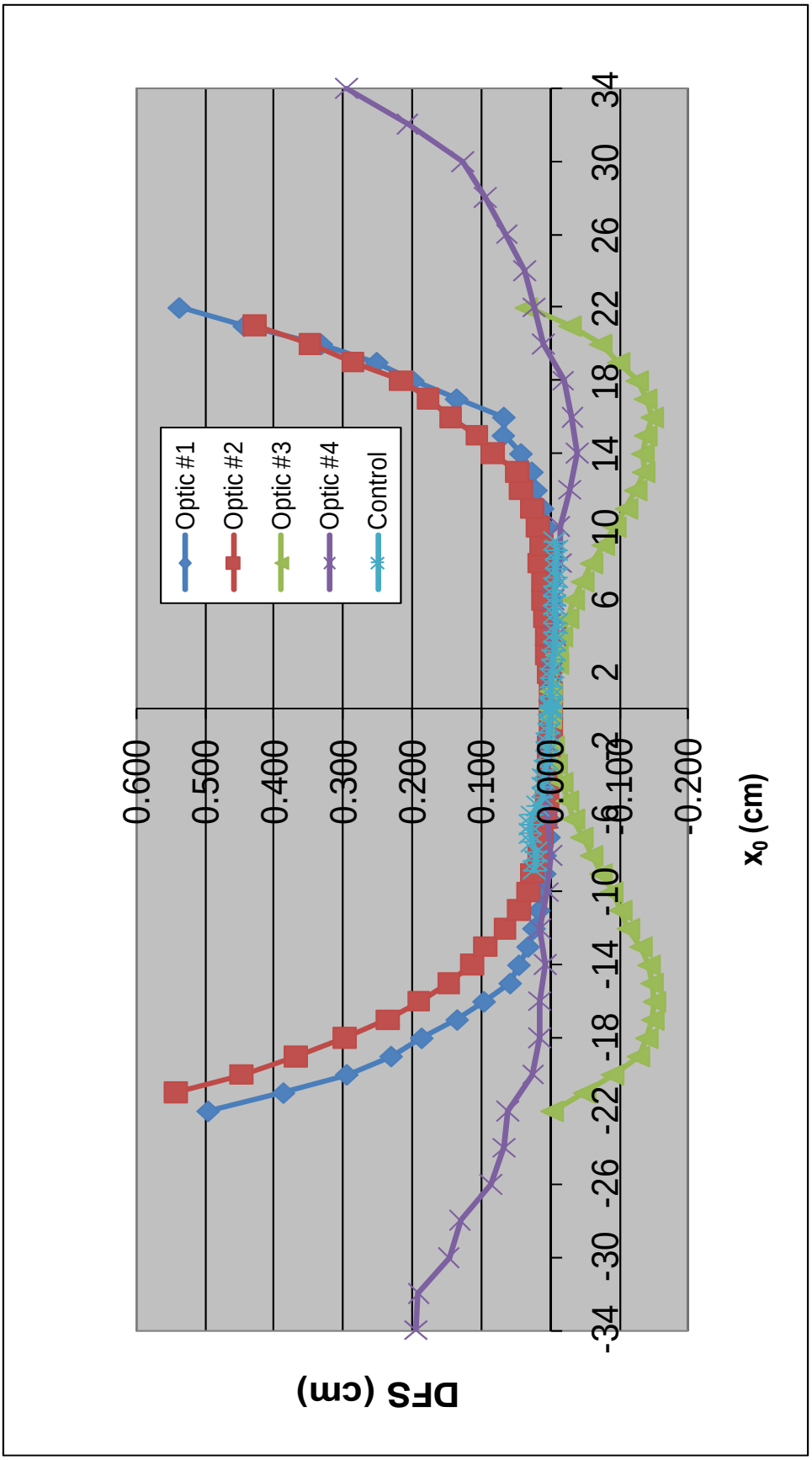

Figure 4.9 Average Departure from Sphere for all optics tested.

The departure from sphere profile for optics 1 and 2 is very similar, but the magnitude of the departure from sphere is high compared to the other optics. Optic 3 has a very interesting departure from sphere which is essentially zero at the edges and the center and optic 4 has the smallest departure from sphere compared to the other optics tested. The chart also shows the average DFS for the control sphere. Remember that the control surface is a rigid optic with a known curvature and as expected, the DFS is very small compared to the thin film optics. The real measure of the tested optics will be in performance, which will be analyzed in the next chapter. The next chapter will present the optical performance analysis, calculation of dominant aberrations based on analytical formulas presented earlier, and an error analysis indicating how measurement errors propagated through to the final surface figure result.

CHAPTER FIVE

ANALYTICS

5.1 Error Analysis

There is always uncertainty in the final result when measurements are made or calculations performed. These uncertainties arise from a variety of sources with some systematic and some being random.[i] A systematic error is a constant bias in the measurement due to a badly calibrated instrument or other equipment issues that the user is unaware of at the time of measurement. Often a systematic error can be removed from the final result since the bias is typically a fixed error. Random errors on the other hand stem from the precision of the actual measurement and can be from instrument resolution or an estimation made by the measurement taker or a combination of both. For instance, a rotary stage may have a measurement scale that allows reading to a tenth of a degree but the user can also estimate a value between the marks thus measuring a value to a greater precision than the scale. With every measurement there is uncertainty.

For the measurements presented, the main objective was to calculate ΔZ in order to create a surface map and calculate the departure from sphere. Examining equation (3.3), it is quite obvious that ΔZ is a function of two measurements, x_0 and θ. Every final result has an associated uncertainty because of the uncertainties in the measured quantities and calculated quantities. The absolute uncertainty in ΔZ, the

surface profile, is shown in equation (5.1), adapted from equation 3.6 in *Experimentation and Uncertainty Analysis for Engineers by* Coleman and Steele.[i]

$$\boldsymbol{U}_{\Delta Z}^{2} = \left(\frac{\partial \Delta Z}{\partial R}\right)^{2} * \boldsymbol{U}_{R}^{2} + \left(\frac{\partial \Delta Z}{\partial x_0}\right)^{2} * \boldsymbol{U}_{x_0}^{2} + \left(\frac{\partial \Delta Z}{\partial \theta}\right)^{2} * \boldsymbol{U}_{\theta}^{2}$$

$$\boldsymbol{U}_{\Delta Z}^{2} = (1)^{2} * \boldsymbol{U}_{R}^{2} + \left(\frac{1}{\tan\theta}\right)^{2} * \boldsymbol{U}_{x_0}^{2} + \left(\frac{x_0}{\sin^{2}\theta}\right)^{2} * \boldsymbol{U}_{\theta}^{2}\ , \qquad \textbf{(5.1)}$$

where the U terms are the uncertainties in the respective variables, and the other parameters have been previously defined and are either measurements or calculations. Examining this equation closely, the uncertainty in $\Delta Z, U_{\Delta z}$, for small angles, grows quite rapidly due to the $sin^4\theta$ term in the denominator. The ΔZ percent error is abnormally high for angles near normal incidence as seen in Table 5.1 below. The edges also have a higher than expected relative uncertainty but this can be reduced with finer resolution equipment.

Table 5.1 Relative Uncertainity in ΔZ (cm)

	0	**20**	**40**	**60**	**80**	**120**	**140**	**160**
-34	4.7E-01	3.8E-01	3.9E-01	3.9E-01	3.9E-01	3.7E-01	3.6E-01	4.0E-01
-32	4.9E-01	4.0E-01	4.1E-01	4.1E-01	4.1E-01	3.9E-01	3.8E-01	4.3E-01
-30	5.3E-01	4.4E-01	4.4E-01	4.5E-01	4.5E-01	4.2E-01	4.2E-01	4.6E-01
-28	5.7E-01	4.6E-01	4.7E-01	4.9E-01	4.8E-01	4.4E-01	4.7E-01	5.0E-01
-26	6.2E-01	5.0E-01	5.2E-01	5.3E-01	5.2E-01	5.2E-01	5.0E-01	5.4E-01
-24	6.7E-01	5.4E-01	5.6E-01	5.8E-01	5.8E-01	5.7E-01	5.4E-01	6.0E-01
-22	7.4E-01	5.9E-01	6.1E-01	6.3E-01	6.3E-01	6.2E-01	6.1E-01	6.3E-01
-20	8.3E-01	6.9E-01	6.7E-01	7.0E-01	7.0E-01	7.0E-01	7.0E-01	7.3E-01
-18	9.1E-01	7.6E-01	7.8E-01	7.8E-01	7.8E-01	7.8E-01	7.8E-01	8.0E-01
-16	1.1E+00	8.3E-01	8.8E-01	8.8E-01	8.8E-01	8.8E-01	8.3E-01	9.0E-01
-14	1.3E+00	9.4E-01	1.0E+00	1.0E+00	1.1E+00	1.0E+00	1.0E+00	1.0E+00
-12	1.3E+00	1.2E+00	1.2E+00	1.2E+00	1.2E+00	1.2E+00	1.2E+00	1.2E+00
-10	1.7E+00	1.4E+00	1.4E+00	1.4E+00	1.5E+00	1.4E+00	1.4E+00	1.4E+00
-8	2.2E+00	1.8E+00	1.8E+00	1.8E+00	1.8E+00	2.0E+00	1.8E+00	2.0E+00
-6	2.3E+00	2.5E+00	2.8E+00	2.8E+00	2.8E+00	2.8E+00	2.8E+00	2.8E+00
-4	3.8E+00	6.3E+00	6.5E+00	6.0E+00	8.1E+00	8.1E+00	5.3E+00	4.8E+00
-2	9.1E+00	7.5E+01	3.5E+01	5.4E+01	1.2E+02	1.2E+02	7.5E+01	3.5E+01
0	ILL CONDITIONED							
2	9.9E+00	1.7E+02	1.7E+02	2.1E+02	3.8E+02	2.0E+02	3.8E+02	3.4E+02
4	4.7E+00	9.2E+00	1.1E+01	1.3E+01	9.2E+00	1.1E+01	2.0E+01	2.3E+01
6	3.0E+00	2.8E+00	2.8E+00	2.8E+00	2.9E+00	3.1E+00	4.1E+00	3.7E+00
8	2.3E+00	1.9E+00	1.8E+00	2.3E+00	2.1E+00	2.0E+00	2.3E+00	2.4E+00
10	1.8E+00	1.4E+00	1.4E+00	1.4E+00	1.7E+00	1.5E+00	1.7E+00	1.6E+00
12	1.5E+00	1.2E+00	1.2E+00	1.3E+00	1.4E+00	1.4E+00	1.5E+00	1.3E+00
14	1.3E+00	1.0E+00	1.0E+00	1.1E+00	1.1E+00	1.1E+00	1.2E+00	1.1E+00
16	1.1E+00	8.8E-01	8.8E-01	8.8E-01	9.2E-01	1.0E+00	1.0E+00	9.2E-01
18	9.9E-01	7.4E-01	7.8E-01	7.9E-01	8.1E-01	8.6E-01	8.6E-01	8.1E-01
20	8.6E-01	6.4E-01	6.7E-01	7.0E-01	7.0E-01	7.1E-01	7.8E-01	7.0E-01
22	7.6E-01	5.9E-01	5.9E-01	6.3E-01	6.3E-01	6.3E-01	6.9E-01	6.3E-01
24	7.0E-01	5.4E-01	5.4E-01	5.7E-01	5.8E-01	5.8E-01	6.0E-01	5.6E-01
26	6.5E-01	5.0E-01	5.0E-01	5.2E-01	5.2E-01	5.4E-01	5.4E-01	5.0E-01
28	5.8E-01	4.6E-01	4.6E-01	4.7E-01	4.8E-01	5.0E-01	5.0E-01	4.7E-01
30	5.3E-01	4.2E-01	4.2E-01	4.4E-01	4.4E-01	4.5E-01	4.6E-01	4.4E-01
32	5.0E-01	3.9E-01	3.8E-01	4.0E-01	4.0E-01	4.0E-01	4.2E-01	4.0E-01
34	4.7E-01	3.6E-01	3.5E-01	3.6E-01	3.6E-01	3.7E-01	3.8E-01	3.7E-01

By a similar expression, the uncertainty in the radius of curvature can be determined as well, and as in the expression for ΔZ, the uncertainty grows rapidly for small angles of incidence. The uncertainty is high near the center of the mirror, or small angles of incidence, because in measuring small angular changes at very small absolute angular values, the measured value of the angle is a very large percentage of the absolute value.

5.2 Analytic Aberration Calculation

The wavefront shape has been determined for the optics tested; next the primary Seidel aberrations need to be calculated for comparison to the computer optical analysis performed in the next section. The following calculations are for the Seidel aberrations only, and for comparison, the Zernike standard coefficients for each optic are included in Appendix A. As stated in Chapter 2, the expression for the Seidel aberrations is

$$\mathbf{W} = \sum_{\mathbf{ijk}} \mathbf{W_{ijk}} * \overline{\mathbf{H^1}} * \boldsymbol{\rho}^{\mathbf{j}} * \mathbf{cos}^{\mathbf{k}} \boldsymbol{\varphi}. \tag{5.2}$$

However for a sun tracking system, the object is nearly stationary on-axis, so $\overline{H}$ in the above equation will be zero for the field dependent aberration contributions such as coma and astigmatism. The primary aberration for examination is then spherical aberration which as stated previously is

$$\Delta \mathbf{W} = \mathbf{W_{040}} * \boldsymbol{\rho}^{\mathbf{4}}, \tag{5.3}$$

and is only dependent on the radial position within the pupil. Even though previous discussions indicated that solar collectors need to be parabolic in shape for smaller focus spots, the optics tested as part of this investigation were designed to be spherical. There

will be some inherent spherical aberration present from an ideal spherical surface. A spherical reference surface was created for each optic based on the average radius of curvature. The individual departures from spherical were measured from each optic's spherical reference surface. The analytic analysis will examine the spherical aberration present in the optics and all calculations will be made at the extrema of the pupil. The following equation as presented by Mouroulis and Macdonald in *Geometrical Optics and Optical Design* will be used to determine the amount of spherical aberration:

$$\mathbf{S_I = -2 * n * c^3 * h^4 = 8 * W_{040}}. \quad \textbf{(5.4)}$$

In the above equation, S_I is the Seidel aberration sum, n is the index of refraction, c is the curvature of the surface, and h is the pupil position in units of length. For a mirror in air, this reduces to

$$\mathbf{W_{040} = \frac{h^4}{4 * R^3}}. \quad \textbf{(5.5)}$$

For ideal spheres, this equation was used to determine the amount of spherical aberration present because the surface is spherical. Using the 1 m optic as an example, $h = 34\ cm$ and $R = 115\ cm$, so $W_{040} = 0.2\ cm$ of spherical aberration, or ~4000 waves for $\lambda = 0.55\ \mu m$. For each rotation of the optic, a radius of curvature was calculated for the point at the edge of the pupil. By inserting these radii and averaging, the W_{040} of the tested 1 m optic is 0.24 cm, or ~4400 waves for λ=0.55 μm. The above statement about coma and astigmatism not being present is not entirely correct since the aperture of the mirror is acting as the stop and the angle to the edge of the sun is ~0.25 deg. From

Mouroulis and Macdonald in *Geometrical Optics and Optical Design*, the Seidel sum for coma is

$$\mathbf{S_{II} = -2 * \bar{u}^2 * c * h^2 = 2 * W_{131}}, \quad \textbf{(5.6)}$$

where $\bar{u}$ is the maximum field angle and the other variables are already defined. The result is that W_{131} is approximately 4.3 μm, or 7.8 waves for λ=0.55 μm. This is a small contribution to the overall aberration and it can be shown that the astigmatism contribution is on the same order. There are methods for minimizing coma and astigmatism by shifting the location of the stop. This includes placing the stop at the center of curvature of the mirror which is known to eliminate coma and astimatigism. [ii] The contributions from coma and astigmatism are small; therefore, using the aperture of the mirror as the stop is perfectly acceptable.

The primary performance metric will not be the amount of aberration but rather collection efficiency. The collection efficiency is defined as the collection diameter divided by the focused spot diameter where the greater the number, the greater the collection efficiency. The spot diameter is affected by the amount of aberration, but the individual contributions are of no consequence. For each optic tested, collection efficiencies were calculated for an ideal sphere and measured sphere. The spot diameters were taken from ZEMAX at a plane that contains the minimum blur circle for each case, reference and deformed. The ideal sphere is an ideal spherical surface of the appropriate diameter and radius for that particular optic and the measured case is the measured surface profile. All the spot diameters listed are RMS spot diameters.

Table 5.2 Collection efficiency for each optic

Optic #	Aperture (cm)	Spot Dia (mm)		Efficiency	
		Reference	Deformed	Reference	Deformed
1	44	12.726	74.23	34.57	5.93
2	44	12.952	50.119	33.97	8.78
3	44	12.992	56.99	33.87	7.72
4	68	11.042	182.5	61.58	3.73

Solar collection systems aim to maximize the collection efficiency of the system, but the required collection efficiency of a solar collection system is completely dependent on the application and the absorber device. The efficiencies for the deformed optics are low compared to the reference efficiencies, but based on the system, the values may be sufficient to gather the appropriate amount of solar energy.

5.3 Computer Analysis of Aberration

The primary analysis tool will be the optical design and analysis software ZEMAX, which will be utilized to examine the effects of the shape deformations on the surface of the optics. All of the analysis will compare the deformed surface to a reference sphere with an average radius. The deformed surface data must be converted to the right format for ZEMAX in order to perform the wavefront analysis. The measured data is gathered at a radius and at an angle, polar data. A MATLAB routine was developed to convert the polar data points into Cartesian coordinates. The collected data

was in polar format and in converting to Cartesian, the spacing of the points becomes irregular so using the function *gridfit.m* from MATLAB central, the irregular Cartesian grid was interpolated to a regular grid with a finer spacing using a bilinear interpolation between the points. The ZEMAX surface type Grid Sag is used for importing the surface into ZEMAX, where the data format is a regular grid of x and y data points with z points for every point in the grid. The ZEMAX analysis includes a surface with an average radius of curvature with two separate text files to load. The first text file includes zero deformation for use as a reference and the second file includes all the surface deformations that were measured. The figures on the following pages illustrate the ray layouts for the reference and deformed cases for each optic. The deformed surface substantially changes the intersections of the ray bundle and the resultant focus spot. The ray layouts show the location of the image plane which is at the location of minimum blur for each optic and each case, reference and deformed. The spot diagrams are also created at this plane for both the reference and deformed spheres. Additional analysis images are included in Appendix B. These additional figures include a wavefront map and ray fan plot for the optics tested. The wavefront maps and ray fan plots are sampled at the paraxial image plane for both the reference and deformed sphere as determined by the reference sphere.

5.3.1 Optic #1 Optical Analysis Images

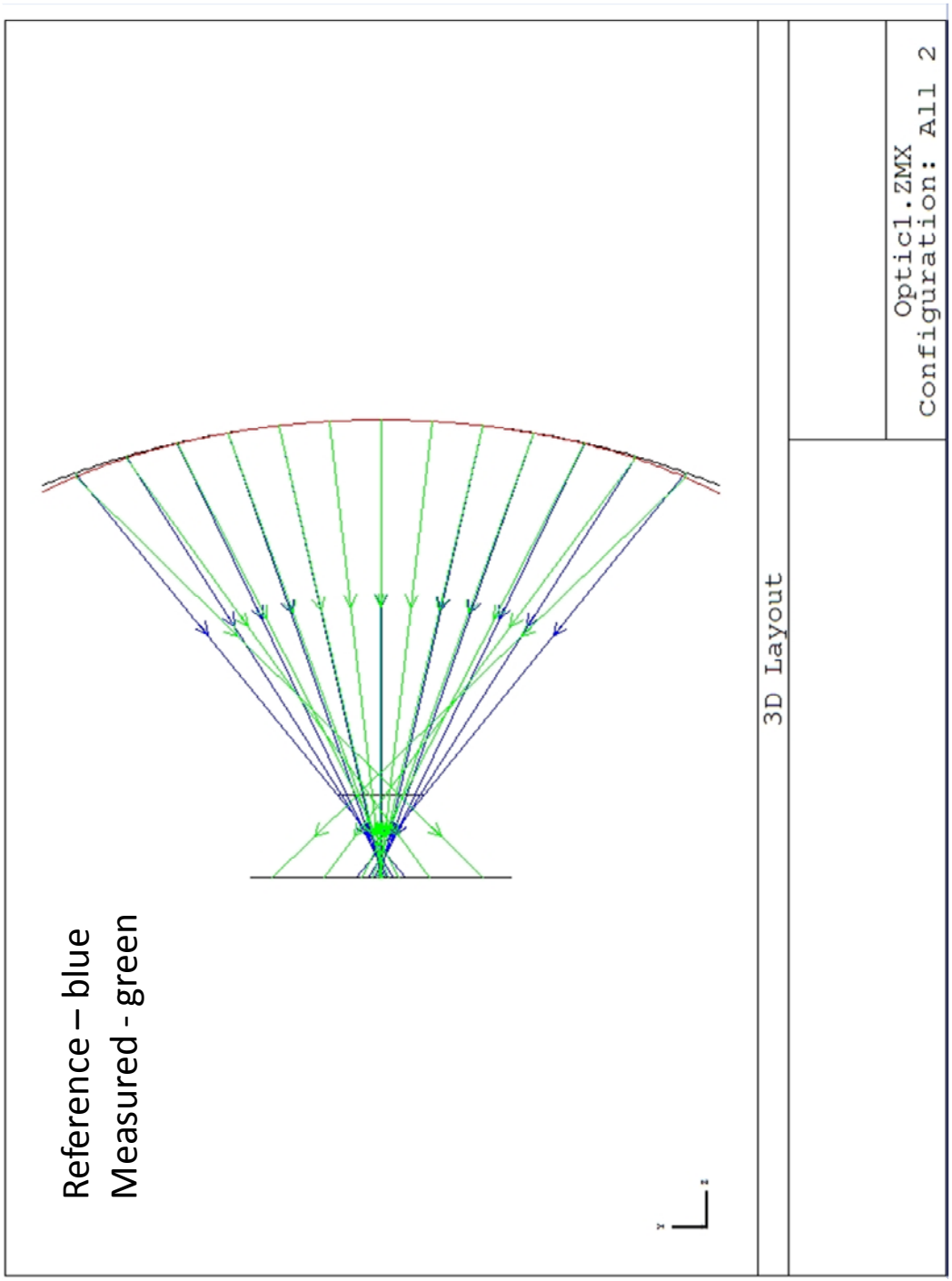

Figure 5.1 Optic #1 Ray Layouts.

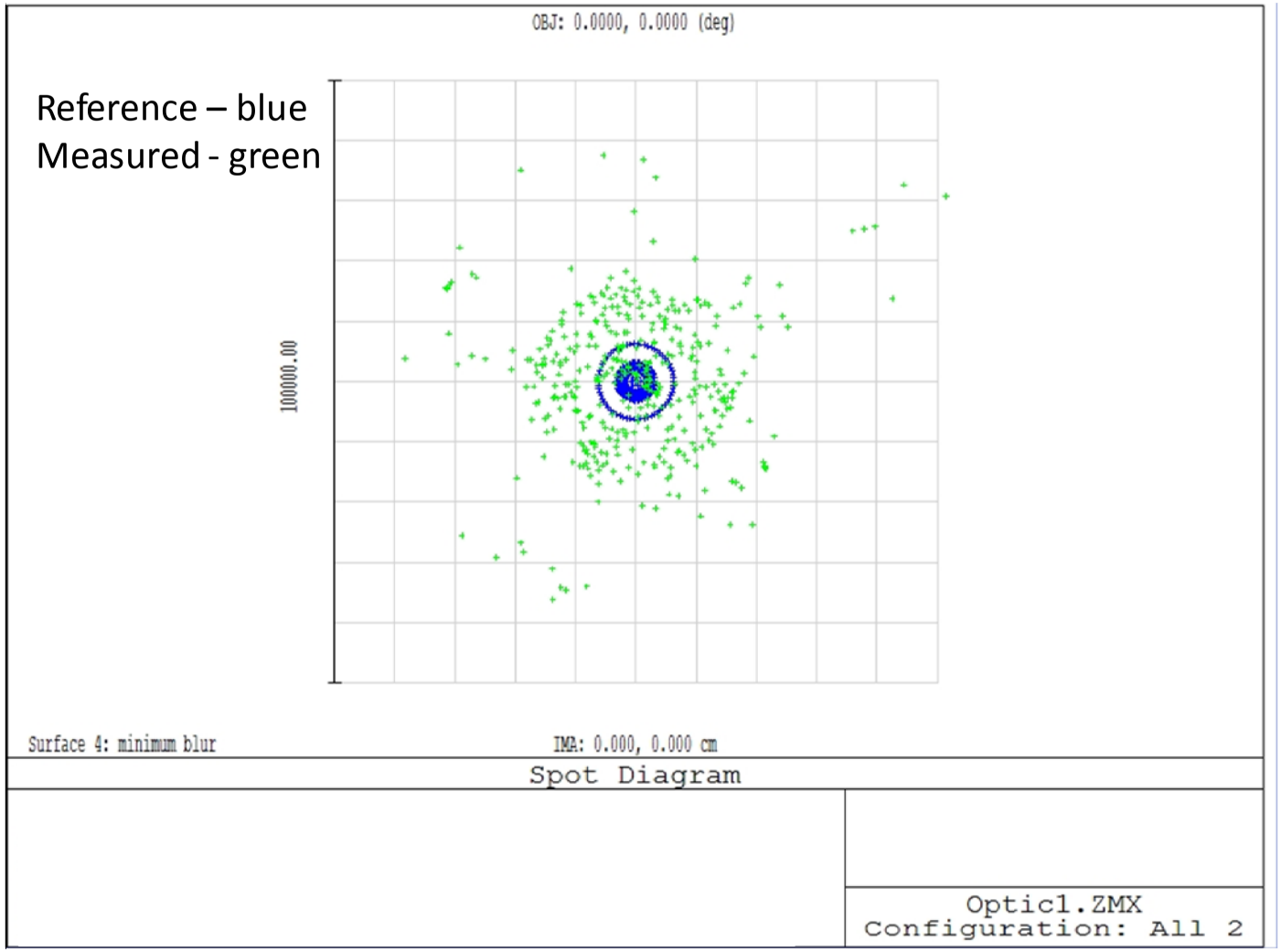

Figure 5.2 Optic #1 Spot Diagrams.

5.3.2 Optic#2 Optical Analysis Images

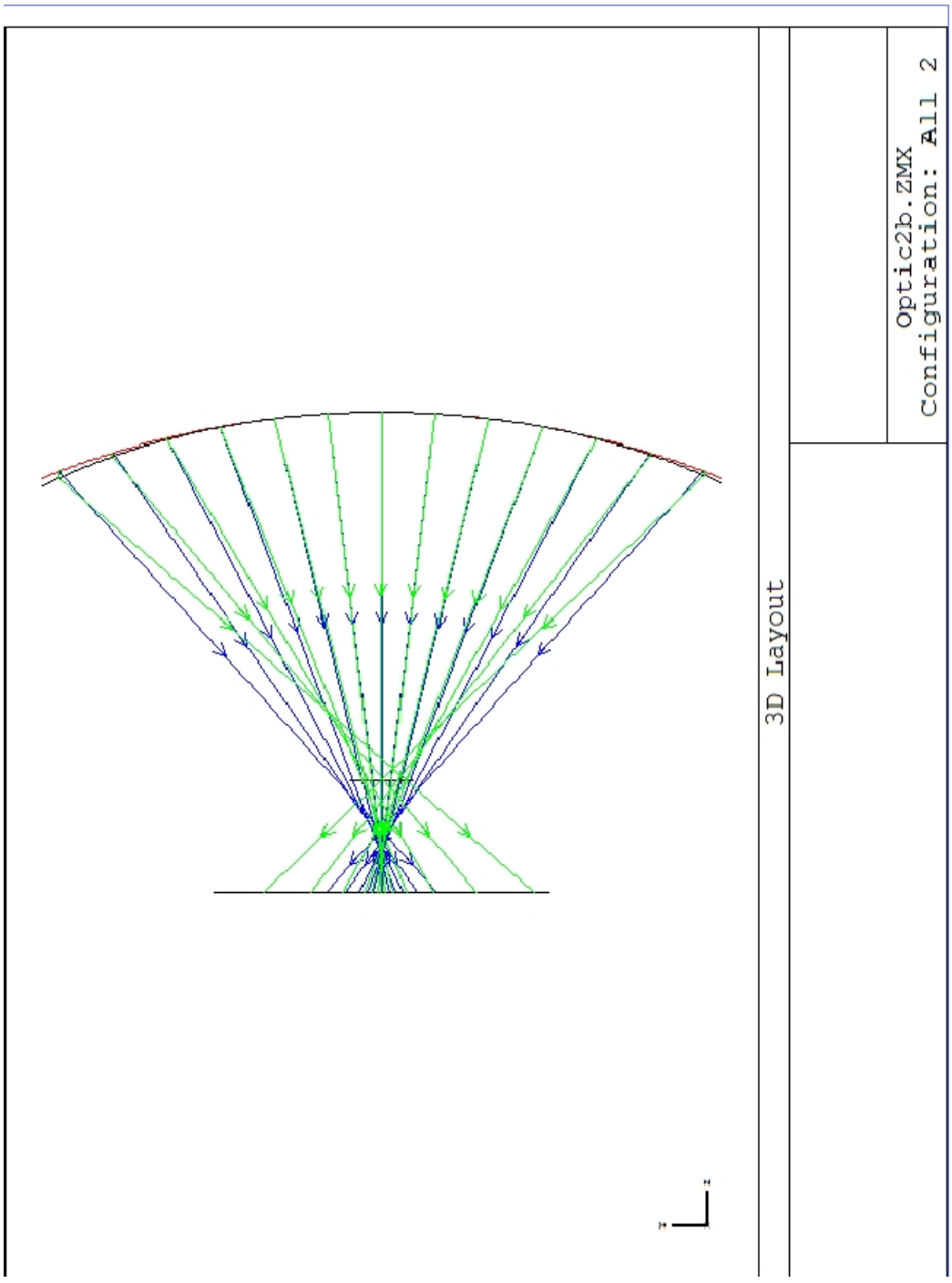

Figure 5.3 Optic #2 Ray Layouts.

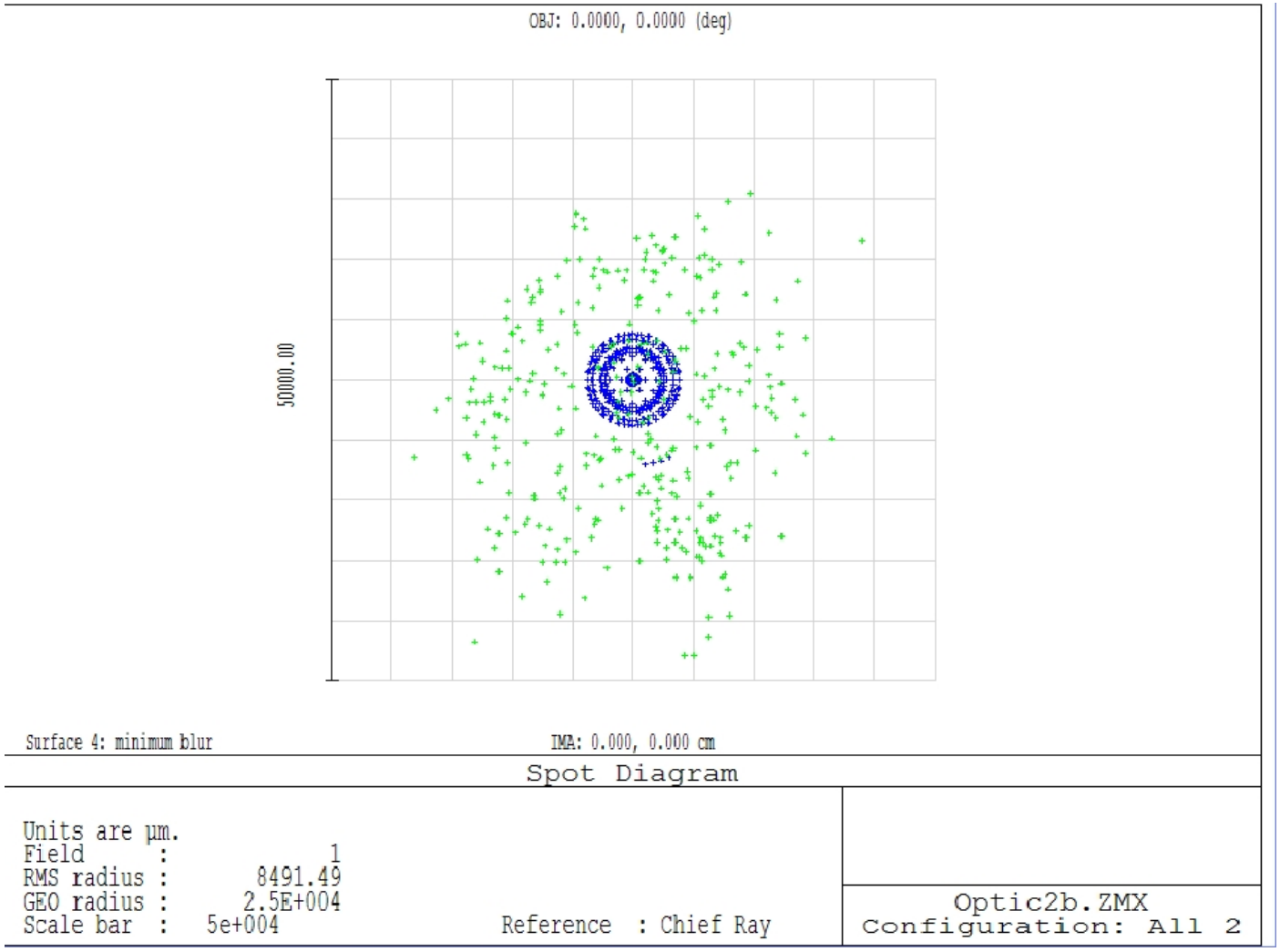

Figure 5.4 Optic #2 Spot Diagrams.

5.3.3 Optic #3 Optical Analysis Images

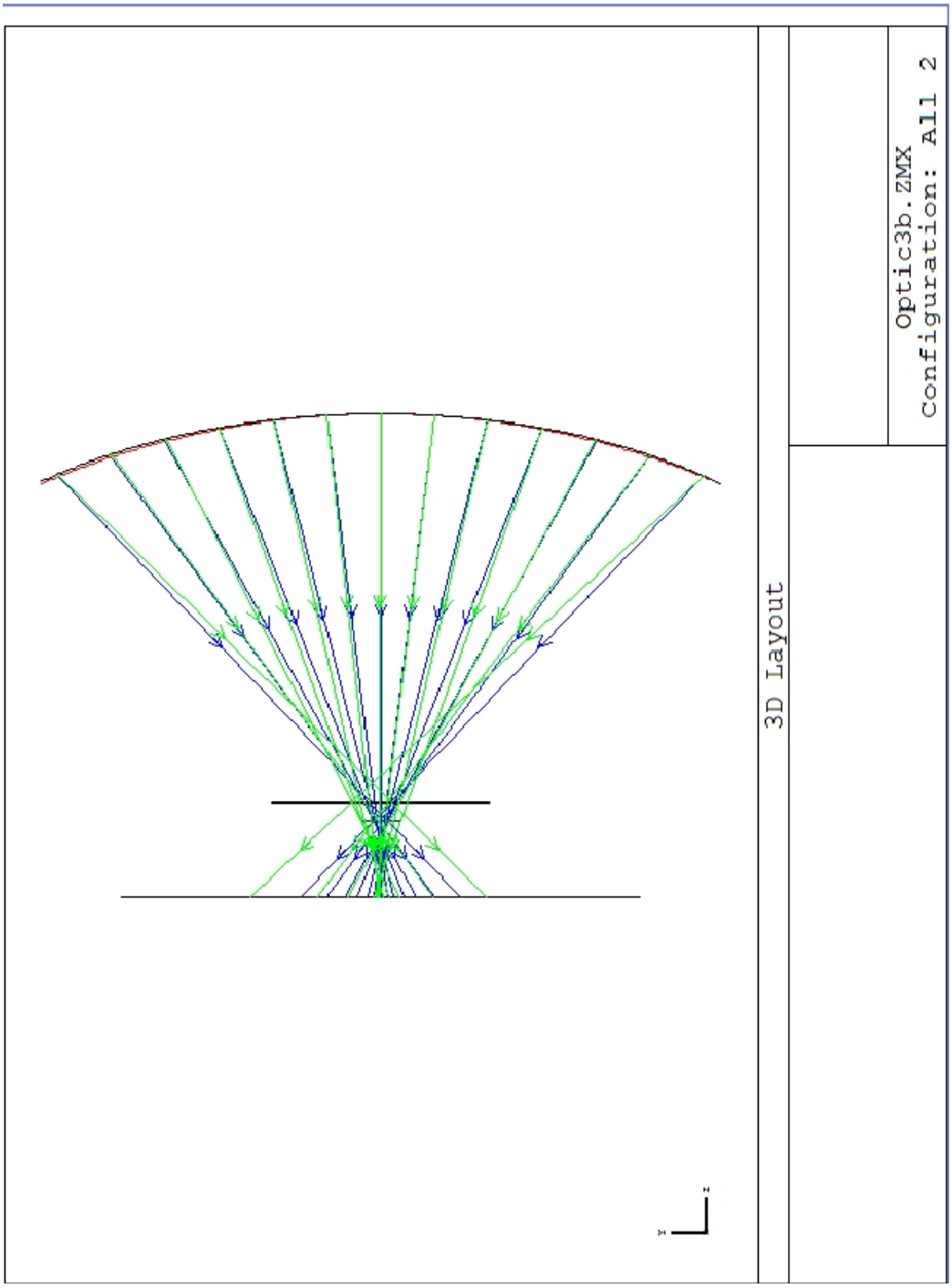

Figure 5.5 Optic #3 Ray Layouts .

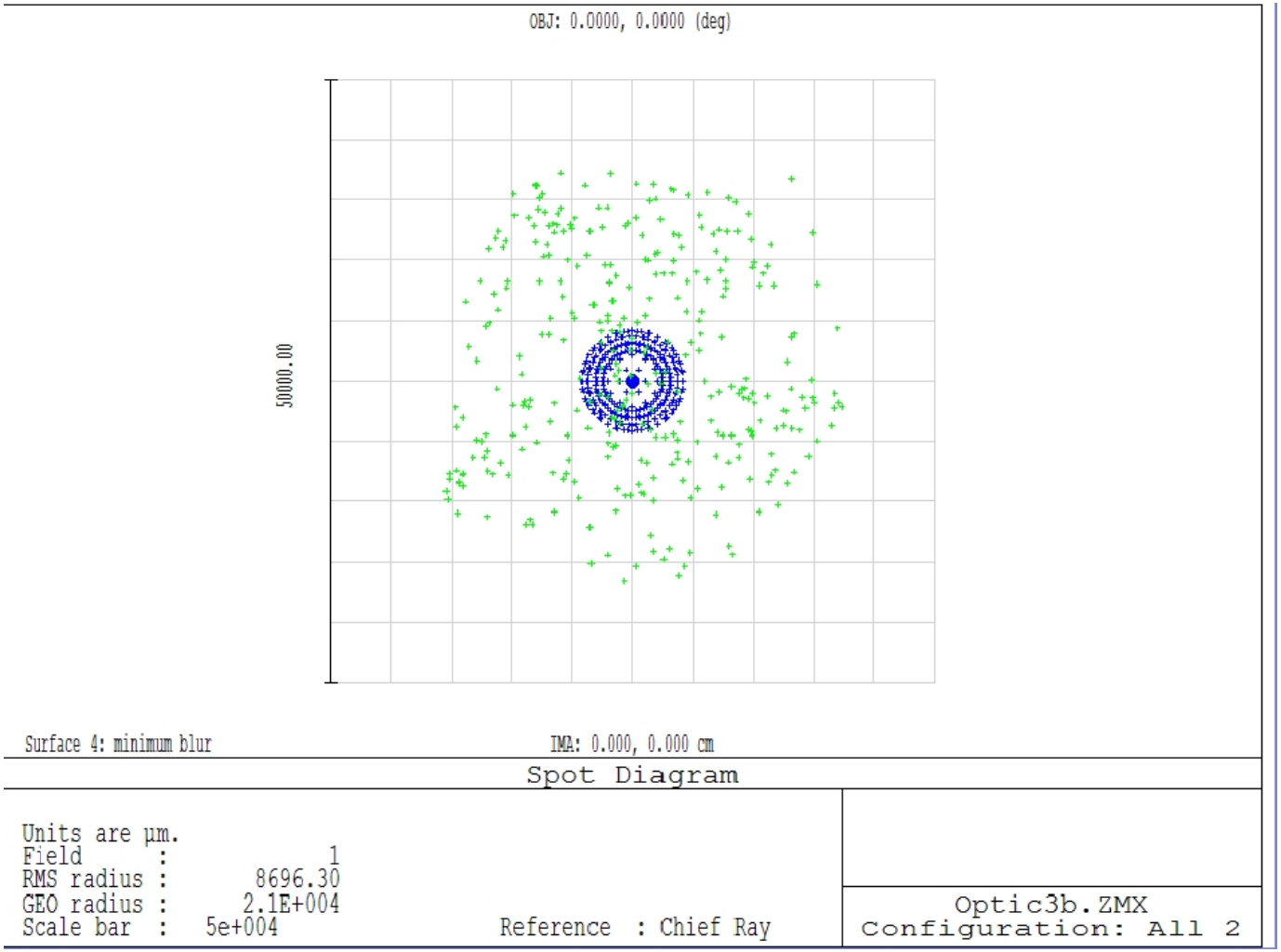

Figure 5.6 Optic #3 Spot Diagrams.

5.3.4 Optic #4 Optical Analysis Images

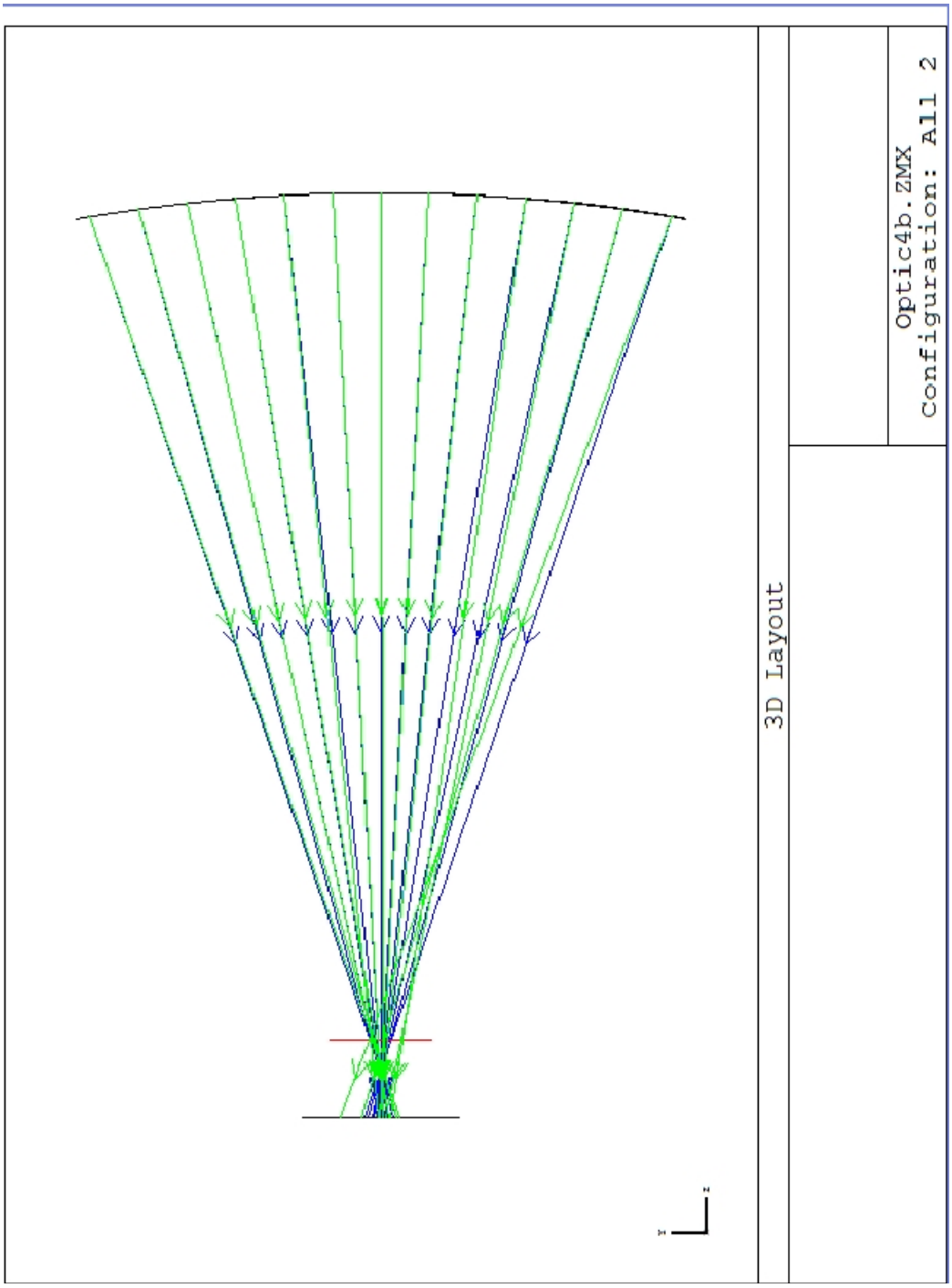

Figure 5.7. Optic #4 Ray Layouts.

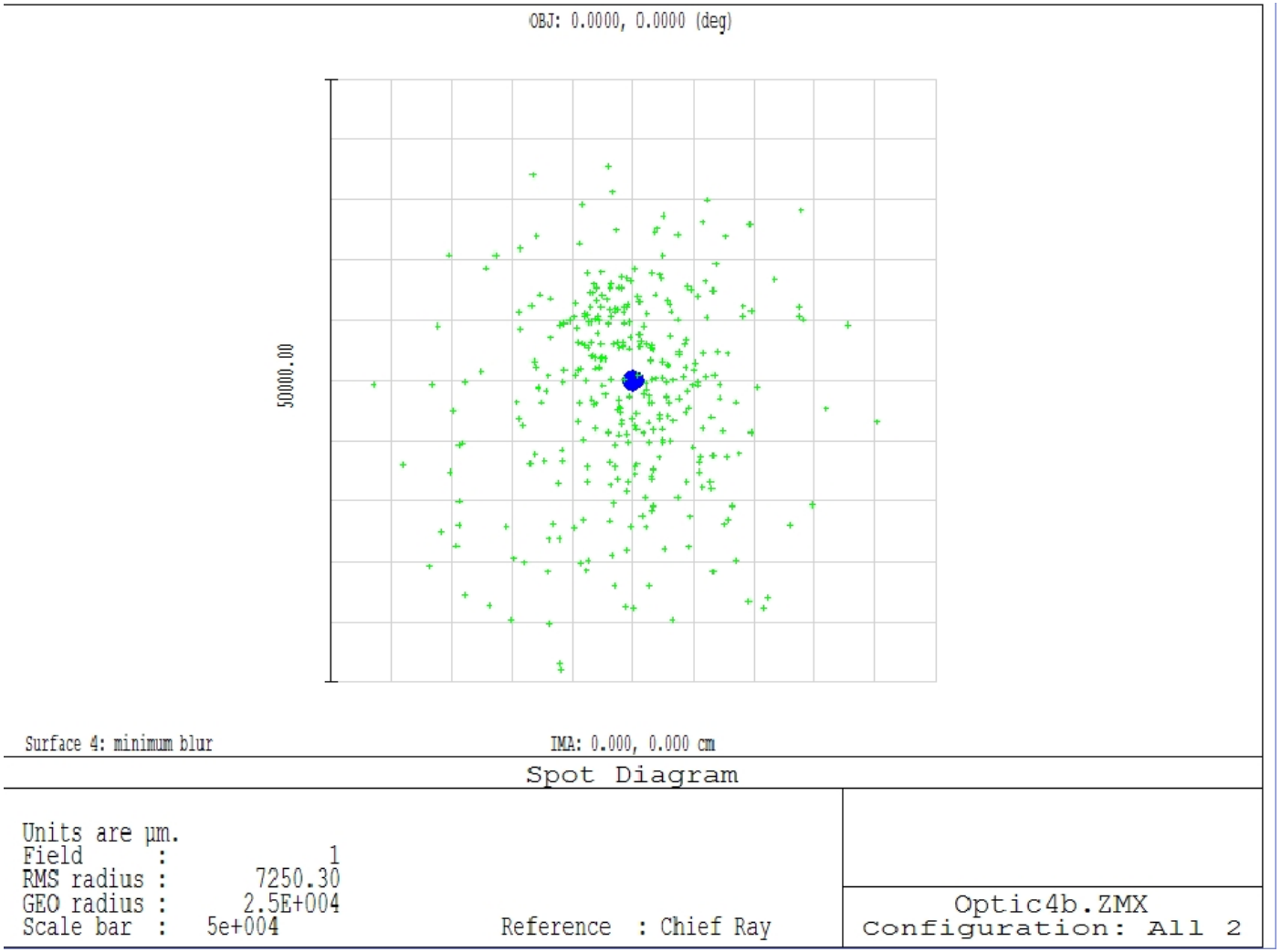

Figure 5.8. Optic #4 Spot Diagrams.

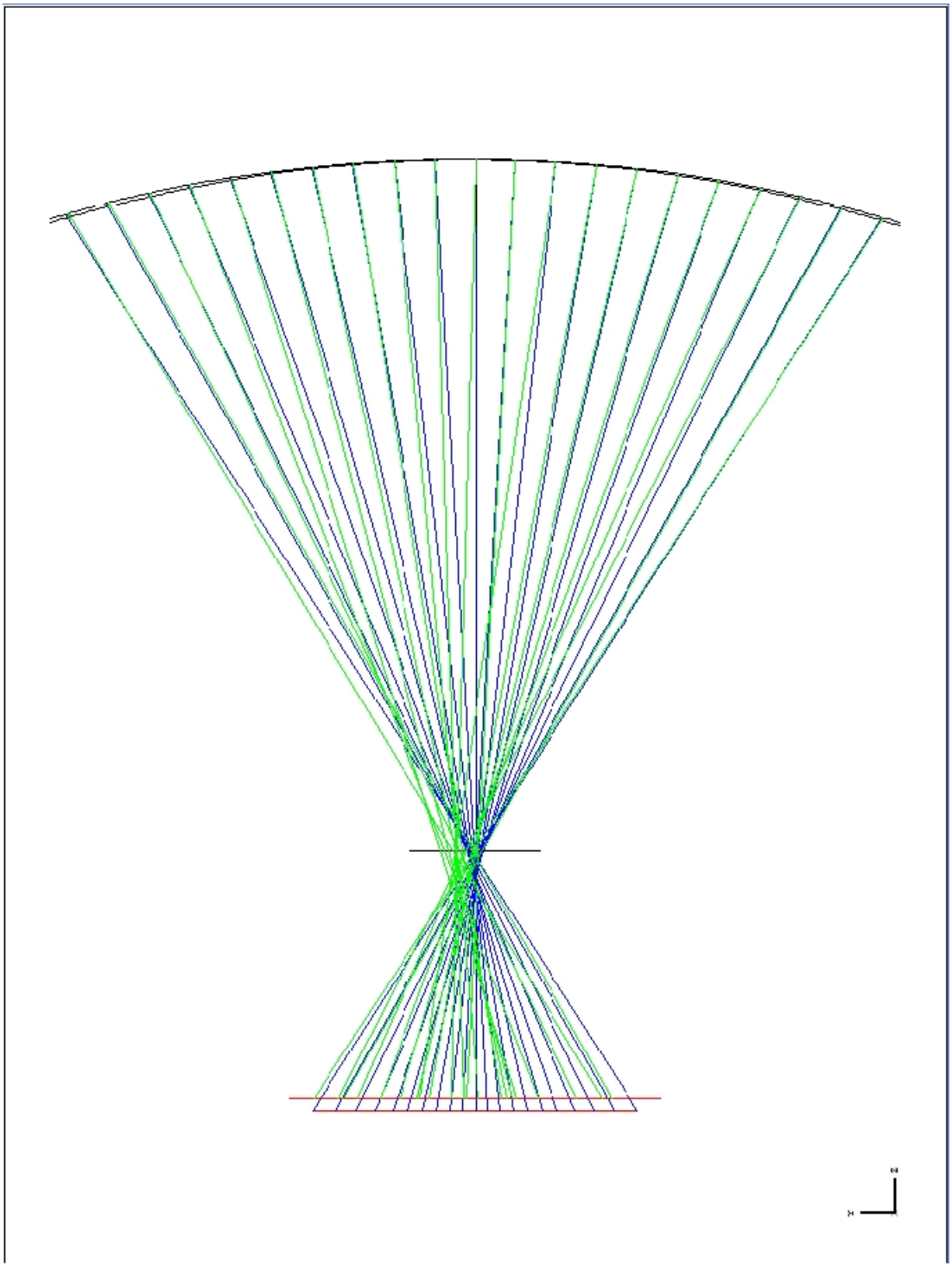

Figure 5.9. Control Surface Layout.

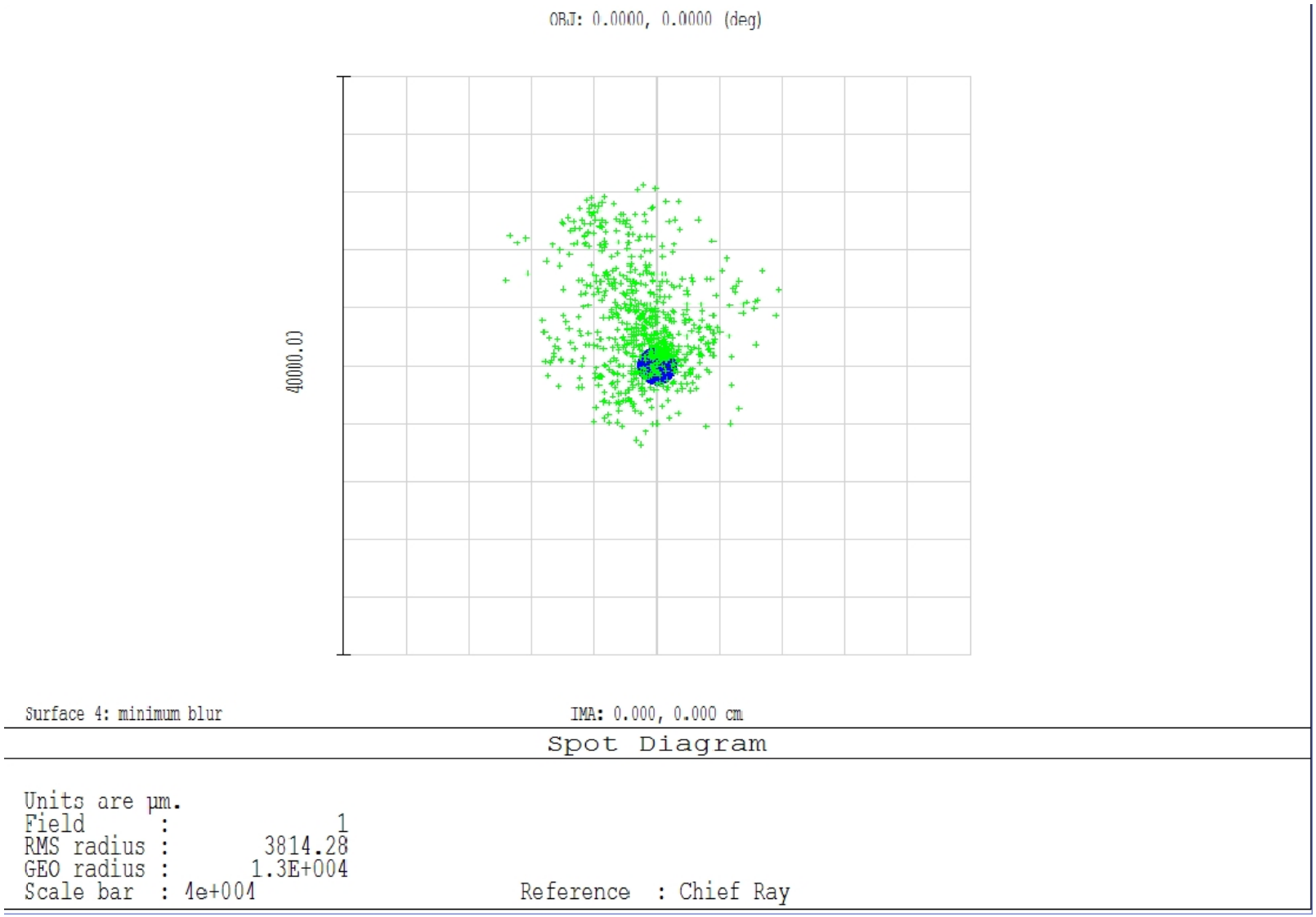

Figure 5.10. Control Surface Spot Diagram.

5.3.5 Discussion

The ray layout plots provide an excellent example of spherical aberration added to the wavefront due to the spherical nature of the surface. Examining the profile of the spot for the reference sphere also points to classic spherical aberration. The three 0.5 m optics tested have surface figures that are fairly uniform across the aperture. The spot diagrams for the deformed case of these optics are nearly circular with just a few outliers, primarily in optic #1. The deformed spot diagram for optic #4 is more erratic even though the overall magnitude of the average departure from sphere was less than the other optics. Just using the spots diagrams and ray layouts, a coarse conclusion can be determined for each optic to its respective performance. A more detailed analysis will include ray fan plots and wavefront maps in order to more closely examine the surface graphically. As mentioned earlier, more images are provided in Appendix A so the reader can examine the ray fans and the wavefronts which are a direct mapping of the surface profile.

---

[i] Coleman, Hugh W., and W. Glenn Steele. *Experimentation and Uncertainty Analysis for Engineers*. Second ed. New York: Wiley, 1999.

[ii] Mouroulis, Pantazis, and John Macdonald. *Geometrical Optics and Optical Design*. New York: Oxford University Press, 1997.

CHAPTER SIX

LA FIN

6.1 Summary and Conclusion

The measurement method presented in the preceding pages is a valid technique for determining the surface figure and resulting performance for large aperture optics that are difficult to measure using traditional interferometry techniques. It was shown that simple geometric relationships can used to quantify the shape of the mirror to ultimately determine the optical quality. The techniques presented in this thesis for measuring the shape profile provided a coarse resolution (1 cm) measurement which can be increased using more sophisticated measurement equipment such as motorized stages and a position sensitive detector or camera to detect spot movement. This and other equipment can also be used to automate the system which will result in finer resolution scans, lower uncertainties, and reduced capture time for a full surface scan. The basic methods presented identified several sources of error which helped to evolve the technique to minimize these errors and can be used in future refinement of the experimental setup.

The sources of error were identified for each method and minimized as the research evolved. The main sources of error in the measurements of the first optic were the lack of an absolute zero reference and the measurement of the spot location of the wall. The lack of the zero reference on the measurement wall could have introduced a bias into the overall shape measurement. The measurement of the spot location was difficult due to the large asymmetric spot size and in some cases, the spot had moved off

the centerline indicating a local tilt in two directions. The measurement technique for the second optic introduced an absolute zero reference which produced a spot on the measurement wall that was co-linear with the vertex of the mirror. However, the measurement of the spot location was still an arduous task. Measurement of the third optic included both measurement methods: the reflected spot location method and mirror method. The data presented in this thesis for the third optic was for the reflected spot method only, so the measurement error in the spot location was still present. Another potential error source was the angle of the wall to the optic axis which, if not perpendicular, would cause the spot location measurement to be incorrect. These sources of error were major factors in developing the third measurement setup using the mirror which allowed for a direct measurement of reflected beam angle instead of spot location. A key parameter in all the methods explored is the nominal radius of curvature which is found by averaging the all the radii calculated. An error in this would cause the departure from sphere calculations to be incorrect, so a better method of determining the nominal radius of curvature needs to be implemented in future measurements. One particular method is moving a light source along an optical rail until a crisp image of the source appears at the back at the source. This indicates the source is located at the center of curvature of the mirror which creates an optical setup with unit magnification.

The measurement method using the mirror to determine the angle of the reflected beam eliminated some major sources of error present in the other methods but also introduced others. The major source of error then was the measurement of the reflected beam angle at near normal angles of incidence. This error is due to the laser beam incidence angle being nearly collinear with the normal of the local tilt surface, which

results in a small reflected beam angle. The uncertainty in the calculations rose rapidly at points near the vertex. An error in the measurement of the reflected beam is a large percentage of the overall angle measured because of the small angular deflection. This error can be reduced by tilting the measurement system which would increase the laser beam incidence angle with respect to the surface normal thereby increasing the reflecting angle. Any error in the measurement of the reflected angle would then be a small percentage of the overall measurement. The same angular relationships presented earlier hold true because the normal to the local tilt plane will still bisect the angle created by the incident beam and the reflected beam so the data reduction is not drastically changed.

The overall departure from sphere was lower for the fourth optic which was scanned using the mirror method for determining the reflected beam angle. There are two possible reasons for this improvement; the optic is actually closer to a spherical shape than the previous optics or the measurement errors have been reduced enough to illustrate a more accurate profile of the optic. The ultimate metric for the optics is not the shape profile but the collection efficiency of the optic. Table 5.2 lists the collection efficiencies for the four optics tested and the larger optic, number 4, has the lowest highest collection efficiency, however, the tested aperture of the optic is a smaller percentage of the overall optic diameter compared to the first 3 optics. As the tested aperture is increased, the spot size will increase therefore decreasing the efficiency. The spot size increased drastically from the ideal sphere case when the actual surface profile was included. The measured profiles of the optics appeared to have an aspherical profile helping to reduce the effect of spherical aberration on the spot size. Departure from parabola was calculated for all of the optics and the deviations were greater than the DFS

- as expected, since the optics were nominally designed to be spherical. In the majority of applications, the preferred profile is parabolic for the elimination of spherical aberration thus creating a smaller spot and higher collection efficiencies.

The minimum efficiency required is dependent on the specific application of the thin film membrane, so for some applications, a spherical profile is sufficient. For instance, solar pumped lasers typically require greater collection efficiencies than solar sails and solar collectors for energy production. These greater collection efficiencies are achieved with smaller spot sizes or by increasing the diameter of the optic to increase the overall power of the focused spot even though the spot diameter may increase as well. In other applications such as solar thermal propulsion or solar heating, the main goal is to collect large amounts of energy in a volume, therefore focus volume is a key metric instead of pure spot diameter.

Computer aided analysis can be very beneficial to the design of solar collection systems. The optic can be measured and then the data input into the overall optical system to analyze the effect of non-ideal shapes. This is less expensive than building the full system to test and then realizing some factor in the manufacturing process has caused the thin-film membrane to have an incorrect shape. Also, the computer aided analysis can assist in designing corrective optics for a system in which the thin-film membrane has substantial shape errors but would be too costly to re-manufacture. The techniques presented in this paper provide a method for characterizing the shape so that an accurate model can be input into such a computer aided analysis. These techniques were verified by independent spherometer measurements on a rigid optic illustrating that these simple geometric methods can be used to provide accurate data for the optical design software.

The simple geometric relationships and measurement methods presented here are an excellent low cost method of extracting the relevant shape information from thin film membranes. The uncertainties are high for some of the measurements but the application of the optic determines the significance of the error and if needed, mitigation procedures can be used to decrease the error. These mitigation procedures include modifying the setup and adding computer control of the translation and rotation stages. This will reduce the uncertainty near the vertex and increase the resolution of the measurement system. The technique was compared with a commonly accepted surface measuring instrument and proved to be valid method for determining the shape profile of the optic. The use of computer design software was illustrated with the measured surfaces and a brief analysis was demonstrated using this software. The majority of these optics are used in non-imaging applications, therefore, the overall aberration is allowed to be higher as long as the requisite amount of energy is collected into the specific focus volume or focus spot as defined by the application.

APPENDICES

APPENDIX A

Zernike Coefficients of Tested Optics

The main two methods of classifying aberrations of an optical system consist of Seidel coefficients and Zernike coefficients. The Seidel coefficients were described and calculated for the optics tested as part of this thesis. The mathematical construct and definitions of the Zernike coefficients will not be discussed here. However, the first 37 Zernike coefficients for each optic are listed below for comparison.

Table A.1 Zernike Standard Coefficients

Coefficient	Optic 1 Value	Optic 2 Value	Optic 3 Value	Optic 4 Value
1	6369.49	8227.18	7232.35	1717.90
2	115.52	141.94	-259.93	571.80
3	-30.44	1821.81	-364.06	28.56
4	5828.28	6689.48	6356.15	1395.50
5	237.27	-33.80	-105.11	-399.92
6	-65.70	496.77	20.42	759.57
7	-146.46	562.60	-232.34	-253.21
8	107.30	83.31	-26.60	99.51
9	-188.48	-382.33	427.84	-27.06
10	116.83	258.71	-258.18	-131.82
11	1761.87	1448.75	1645.38	403.50
12	55.94	-68.75	-9.14	19.86
13	24.51	3.09	-41.53	12.46
14	106.64	52.01	-171.63	279.06
15	-295.52	67.69	32.12	61.86
16	76.32	-12.68	-48.94	47.13
17	-113.13	-11.05	54.23	-141.20
18	-70.88	-1.06	-0.26	213.05
19	-134.76	23.34	-89.91	-8.94
20	162.68	-17.03	-97.51	90.43
21	-358.39	-410.67	381.47	-87.98
22	-7.67	-132.06	-118.37	35.85
23	-90.65	-37.04	9.61	22.02
24	-27.12	84.90	31.77	82.24
25	41.75	-13.75	208.36	55.62
26	-21.52	-143.07	-163.69	8.13
27	32.64	74.29	1.03	37.97
28	-397.97	-417.04	-144.33	-4.84
29	-54.68	50.60	52.88	74.75
30	14.51	7.60	-43.35	58.94
31	23.55	34.85	77.41	56.18
32	-76.84	0.31	4.29	26.60
33	71.80	49.78	-213.26	-106.78
34	73.61	-0.96	75.20	76.89
35	257.83	398.36	245.17	308.44
36	-53.09	560.07	-190.45	-305.86
37	-138.80	-13.89	-66.35	-34.11

APPENDIX B

Optical Analysis Plots

The following plots show the wavefront diagram and ray fan plot for each of the measured optics. The wavefront visibly describes the surface of the mirror and the ray fan plots provide an indicator of the performance of the optics by depicting the aberrations present at the image plane. All the plots were generated as part of the analysis in ZEMAX. As expected the dominant aberration is spherical aberration which can clearly be seen from the ray plots by the cubic nature of the ray intercepts. It is a little more difficult to determine spherical aberration from the wavefront maps but these particular optics are dominated by spherical aberration and the maps clearly indicate the quortic nature.

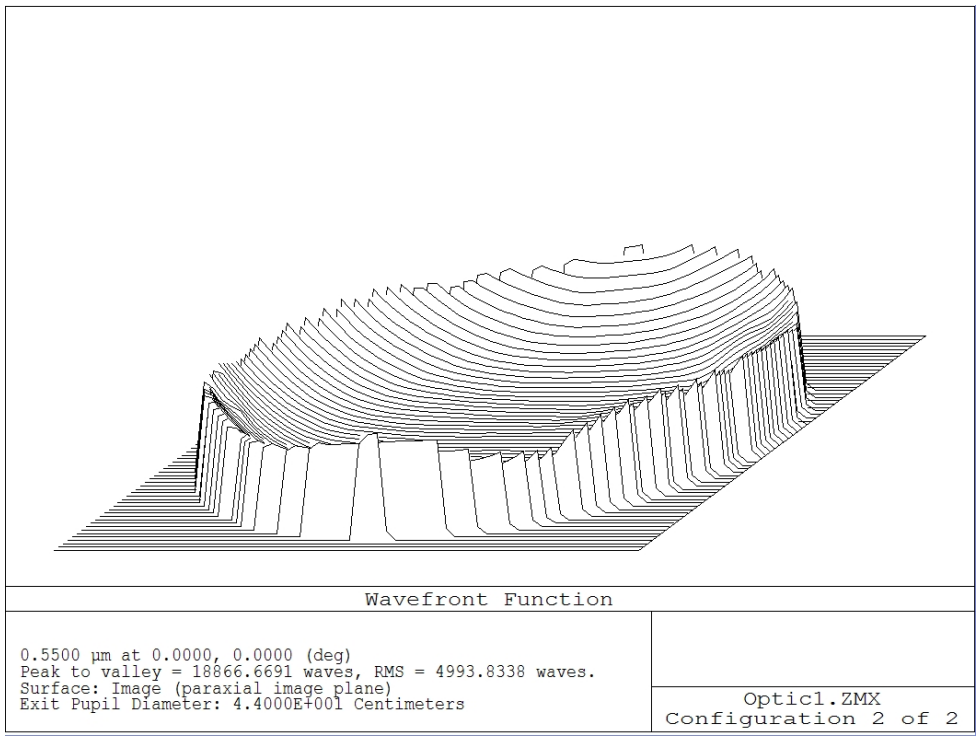

Figure B.1 Optic 1 Wavefront Map.

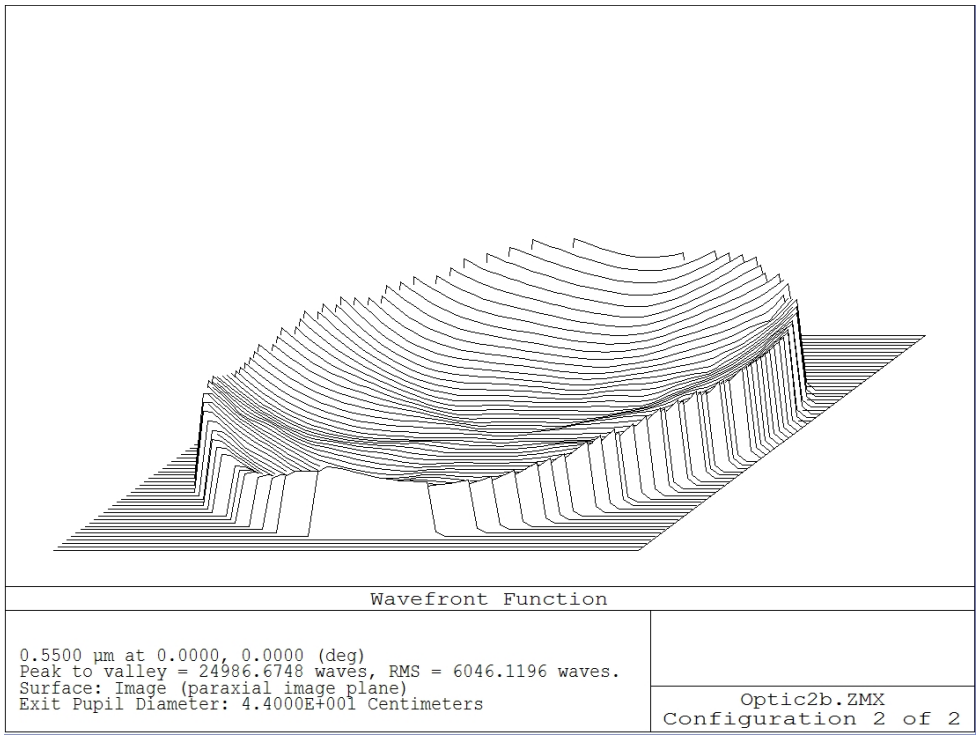

Figure B.2 Optic 2 Wavefront Map.

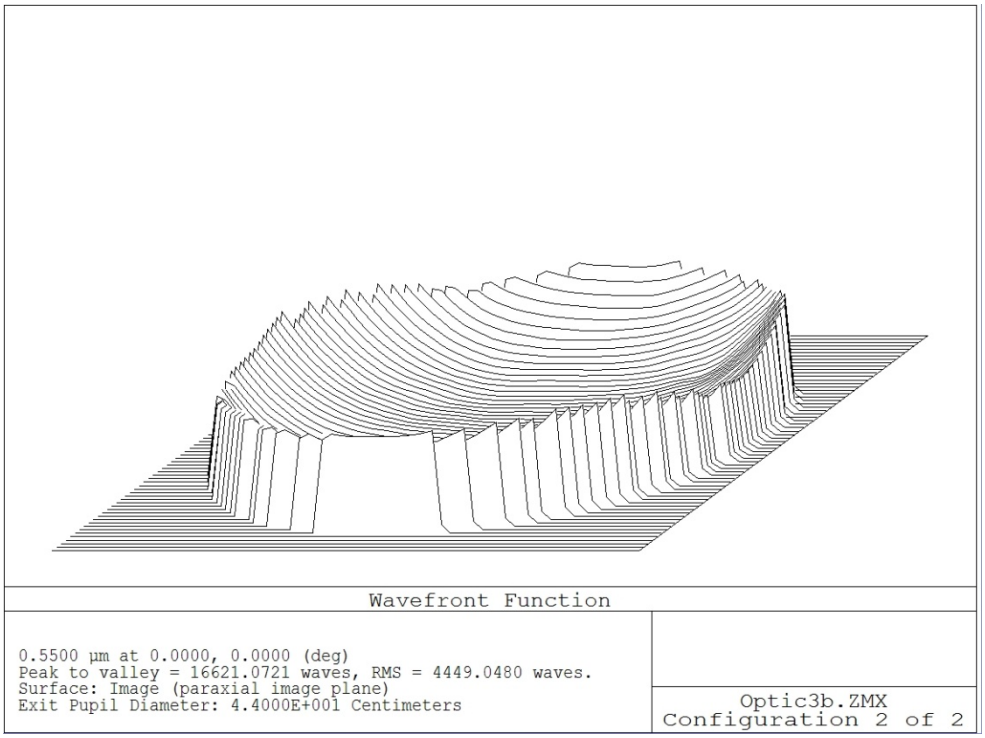

Figure B.3 Optic 3 Wavefront Map.

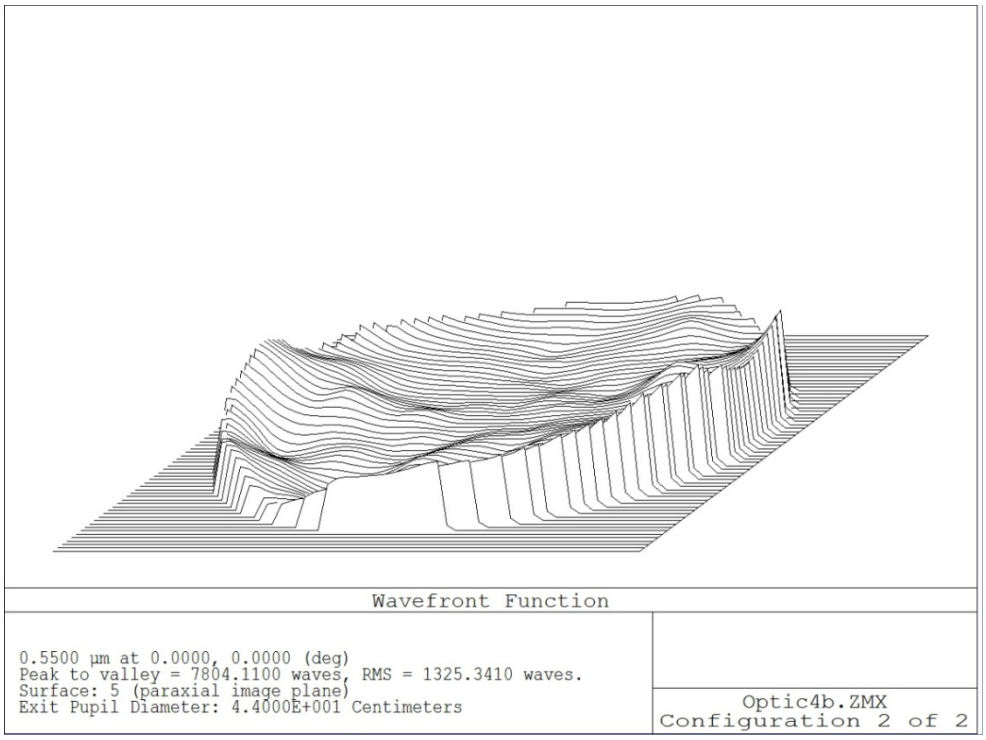

Figure B.4 Optic 4 Wavefront Map.

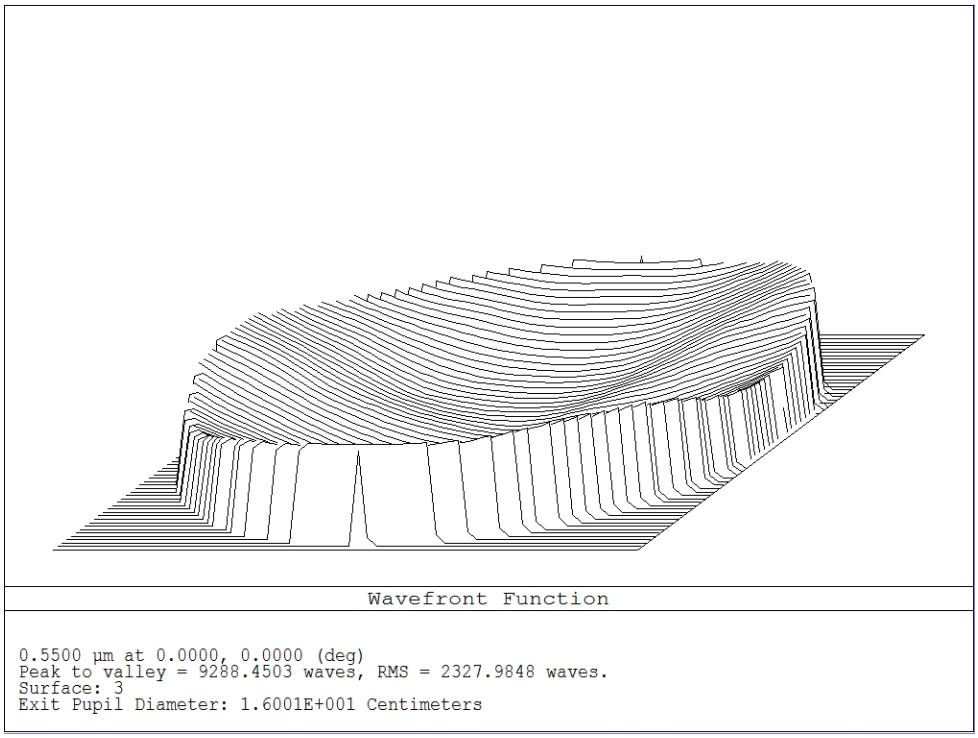

Figure B.5 Control Surface Wavefront Map.

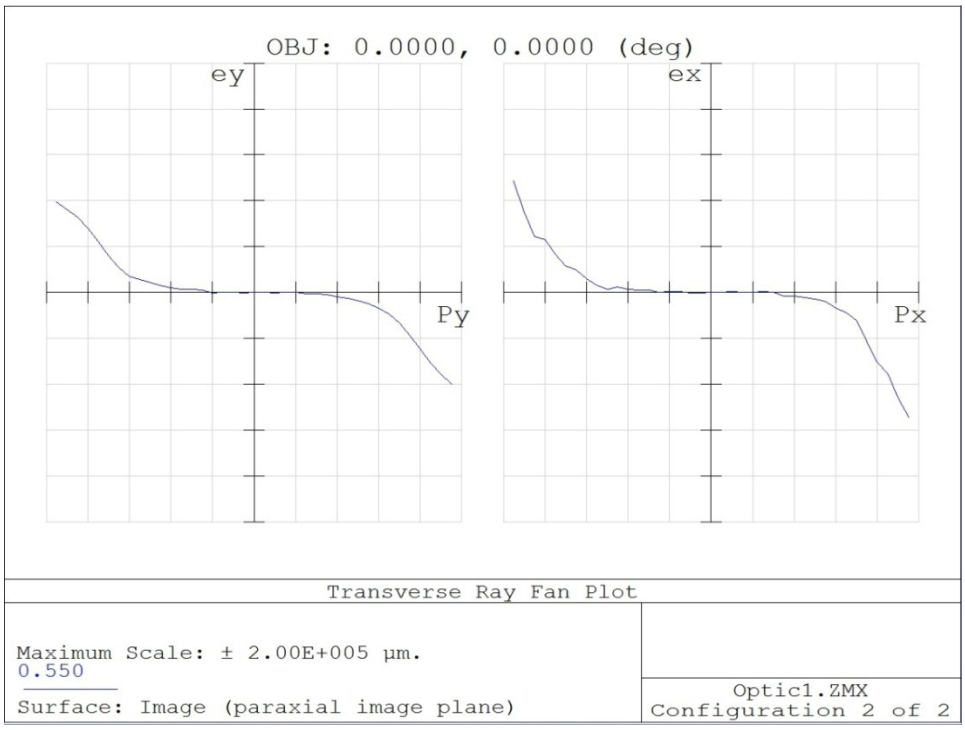

Figure B.6 Optic 1 Ray Fan.

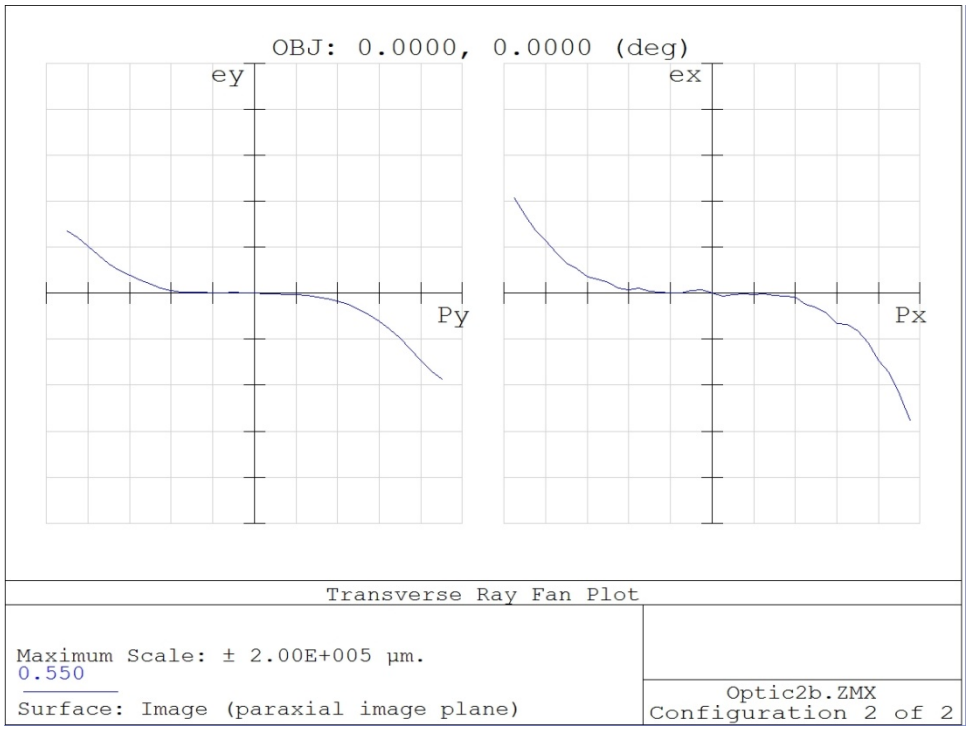

Figure B.7 Optic 2 Ray Fan.

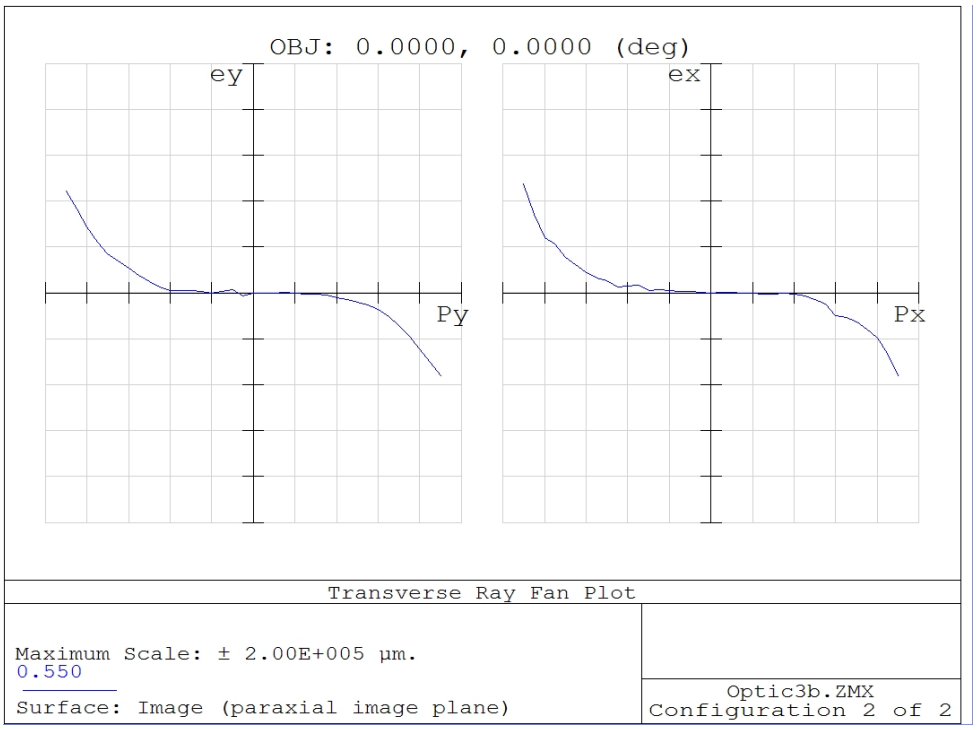

Figure B.8 Optic 3 Ray Fan.

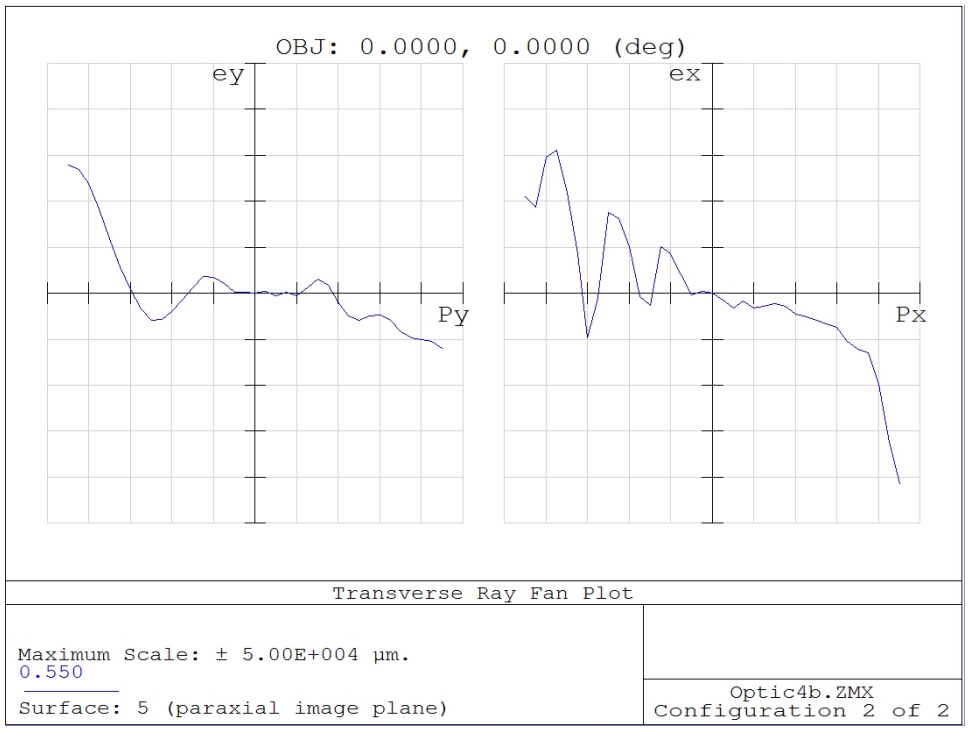

Figure B.9 Optic 4 Ray Fan.

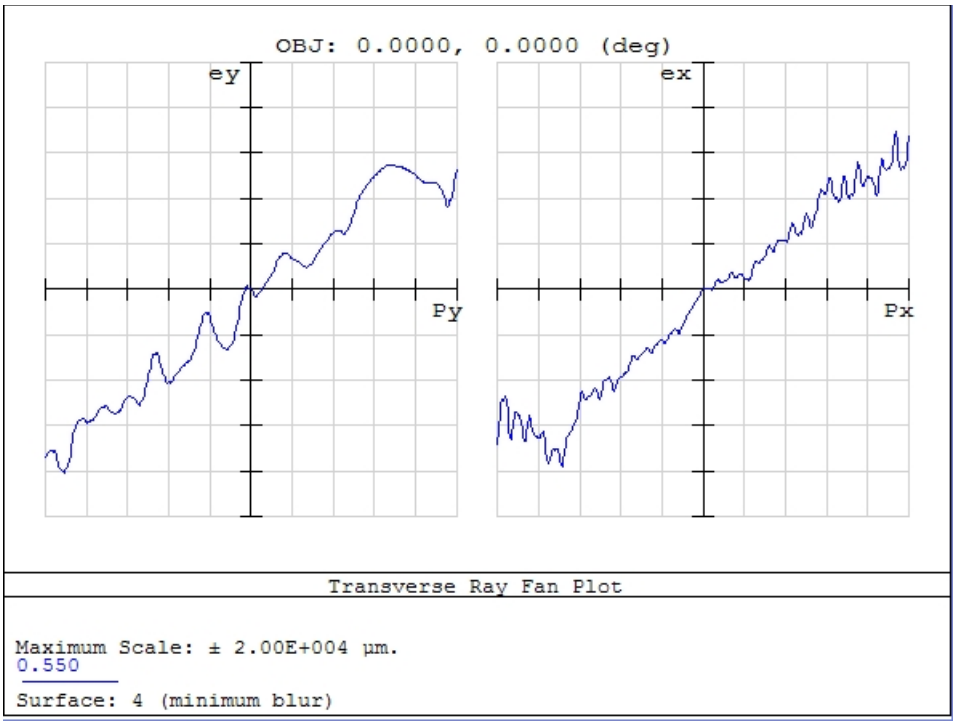

Figure B.10 Control Surface Ray Fan.

REFERENCES

"Burning Mirrors." www.cs.drexel.edu. http://www.cs.drexel.edu/~crorres/Archimedes/Mirrors/Tzetzes.html (accessed September 1, 2010).

Coleman, Hugh W., and W. Glenn Steele. *Experimentation and Uncertainty Analysis for Engineers*. Second ed. New York: Wiley, 1999.

"Concentrated Solar Power."*Solar Thermal Magazine*, October 2004. http://www.solarthermalmagazine.com/learn-more/concentrated-solar-power-csp/ (accessed September 2, 2010).

"Current Projects." Current Projects. http://www.acrim.com/ (accessed March 3, 2011).

"DuPont™ Kapton®: Uses & Applications: Aerospace." DuPont. The miracles of science. http://www2.dupont.com/Kapton/en_US/uses_apps/aero/index.html (accessed August 20, 2010).

Elert, Glenn, and Mathew Tsang. "Power of the Sun." hypertextbook.com. http://hypertextbook.com/facts/1999/MatthewTsang.shtml (accessed October 1, 2010).

Geary, Joseph M. *Introduction to Optical Testing*. Bellingham, Wash., USA: SPIE Optical Engineering Press, 1993.

Hecht, Eugene, and Alfred Zajac. *Optics / Eugene Hecht ; With Contributions by Alfred Zajac*. 2nd ed. Reading, MA: Addision-Wesley, 1987.

Hitz, Breck. "Can Lasers Help Decrease Our Dependence on Fossil Fuels? (Photonics Spectra | Sep 2007 | Tech News)." Photonics.com: Optics, Lasers, Imaging & Fiber Information Resource. http://www.photonics.com/Article.aspx?AID=30649 (accessed September 14, 2010).

Johnston, John. "Analysis and Test Technology For Thin-Film Membrane Structures." Analysis and Test Technology for Thin-Film Membrane Structures. http://femci.gsfc.nasa.gov/workshop/2001/posters/johnston/Johnston_Membrane.pdf (accessed September 15, 2010).

Liverpool John Moores University. "Astrophysics Research Institute." Astrophysics Research Institute. www.astro.ljmu.ac.uk/courses/phys134/pic/scope/airydisk.jpg (accessed April 15, 2011).

Mouroulis, Pantazis, and John Macdonald. *Geometrical Optics and Optical Design*. New York: Oxford University Press, 1997.

Nakamura, Takashi, Robert Krech, James McClanahan, James Shoji, Russell Partch, and Skylar Quinn. "Solar Thermal Propulsion for Small Spacecraft - Engineering System Development and Evaluation." sr-1228.pdf. www.psicorp.com/pdf/library/sr-1228.pdf (accessed October 2, 2010).

O'Shea, Donald C. *Elements of Modern Optical Design*. New York: Wiley, 1985.

Ombello, Carlo. "The world's first molten salt concentrating solar power plant | Environment | guardian.co.uk ." Latest news, comment and reviews from the Guardian | guardian.co.uk . http://www.guardian.co.uk/environment/2010/jul/22/first-molten-salt-solar-power (accessed February 14, 2011).

Pedrotti, Frank L., and Leno S. Pedrotti. *Introduction to Optics*. Englewood Cliffs, NJ: Prentice-Hall, 1987.

"Physics-sun Solar Laser Oozes Millions of Watts." Solar Feeds News Network. http://solarfeeds.com/index.php?option=com_content&view=article&id=2820:physics-sun-solar-laser-oozes-millions-of-watts&catid=76:ecofriend&Itemid=112 (accessed September 13, 2010).

"Press Releases - Enel.com." Home - Enel.com. http://www.enel.com/en-GB/media/press_releases/release.aspx?iddoc=1634858 (accessed September 2, 2010).

"SART-Systemanalyse Raumtransport - Solar Thermal Propulsion." DLR Portal - Lampoldshausen. http://www.la.dlr.de/ra/sart/projects/sto/sto.php.en (accessed October 3, 2010).

Sahara, Hironori, Morio Shimizu, Keitaro Osi, Kai Watanabe, and Yoshihiro Nakamura. "Solar Thermal Propulsion for Microsatellites End-of-life De-orbiting." 0085-0303iepc-full.pdf. sgc.engin.umich.edu/erps/IEPC_2003/proceedings/0085-0303iepc-full.pdf (accessed September 20, 2010).

"Science: Archimedes' Weapon." *Time*, November 26, 1973. http://www.time.com/time/magazine/article/0,9171,908175,00.html (accessed August 20, 2010).

Smith, Brett. "NASA Marshall Space Flight Center - Huntsville, AL: Solar Thermal Propulsion." Best Manufacturing Practices: Your Source for Best Practices and Innovative Technologies. http://www.bmpcoe.org/bestpractices/internal/nasam/nasam_32.html (accessed February 14, 2011).

“Solar Insolation." Solar Water Heater, Solar Hot Water, Solar Hot Water Heater, Solar Heating, Solar Collector by Apricus. http://www.apricus.com/html/solar_collector_insolation.htm (accessed February 15, 2011).

"SolarPACES Home Page." SolarPACES. http://www.solarpaces.org/Tasks/Task1/ps10.htm (accessed September 2, 2010).

"Solar Spectral Irradiance: ASTM G-173." Renewable Resource Data Center (RReDC) Home Page. http://rredc.nrel.gov/solar/spectra/am1.5/ASTMG173/ASTMG173.html (accessed March 3, 2011).

"Types of Solar Collectors, Solar Basics." Solar Water Heater, Solar Hot Water, Solar Hot Water Heater, Solar Heating, Solar Collector by Apricus. http://www.apricus.com/html/solar_typesofsolar.htm (accessed August 20, 2010).

Wyant, James, and Katherine Kreath. "Aberrations and Optical Testing." www.optics.arizona.edu. www.optics.arizona.edu/jcwyant/optics513/ChapterNotes/Chapter03/BasicAberrationsandOpticalTesting.pdf (accessed September 2, 2010).

Yakhyaev, Anvar. "Uzbek Scientists Created a Powerful Solar Laser." *Uzbekistan Today* (Tashkent), November 16, 2007. http://www.ut.uz/eng/today/uzbek_scientists_created_a_powerful_solar_laser.mgr (accessed September 13, 2010).